

INFORMATION TO USERS

This manuscript has been reproduced from the microfilm master. UMI films the text directly from the original or copy submitted. Thus, some thesis and dissertation copies are in typewriter face, while others may be from any type of computer printer.

The quality of this reproduction is dependent upon the quality of the copy submitted. Broken or indistinct print, colored or poor quality illustrations and photographs, print bleedthrough, substandard margins, and improper alignment can adversely affect reproduction.

In the unlikely event that the author did not send UMI a complete manuscript and there are missing pages, these will be noted. Also, if unauthorized copyright material had to be removed, a note will indicate the deletion.

Oversize materials (e.g., maps, drawings, charts) are reproduced by sectioning the original, beginning at the upper left-hand corner and continuing from left to right in equal sections with small overlaps. Each original is also photographed in one exposure and is included in reduced form at the back of the book.

Photographs included in the original manuscript have been reproduced xerographically in this copy. Higher quality 6" x 9" black and white photographic prints are available for any photographs or illustrations appearing in this copy for an additional charge. Contact UMI directly to order.

UMI

**A Bell & Howell Information Company
300 North Zeeb Road, Ann Arbor MI 48106-1346 USA
313/761-4700 800/521-0600**

University of Alberta

**Deposition of Medical Aerosols in the Human Respiratory Tract: Predicting Dosages
from Nebulizers, and Deposition in the Mouth-throat using Computational Fluid
Dynamics**

by

Kevin Walter Stapleton



**A thesis submitted to the Faculty of Graduate Studies and Research in partial fulfillment
of the requirements for the degree of Doctor of Philosophy**

Department of Mechanical Engineering

**Edmonton, Alberta
Spring, 1997**



**National Library
of Canada**

**Acquisitions and
Bibliographic Services**

**395 Wellington Street
Ottawa ON K1A 0N4
Canada**

**Bibliothèque nationale
du Canada**

**Acquisitions et
services bibliographiques**

**395, rue Wellington
Ottawa ON K1A 0N4
Canada**

Your file Votre référence

Our file Notre référence

The author has granted a non-exclusive licence allowing the National Library of Canada to reproduce, loan, distribute or sell copies of his/her thesis by any means and in any form or format, making this thesis available to interested persons.

The author retains ownership of the copyright in his/her thesis. Neither the thesis nor substantial extracts from it may be printed or otherwise reproduced with the author's permission.

L'auteur a accordé une licence non exclusive permettant à la Bibliothèque nationale du Canada de reproduire, prêter, distribuer ou vendre des copies de sa thèse de quelque manière et sous quelque forme que ce soit pour mettre des exemplaires de cette thèse à la disposition des personnes intéressées.

L'auteur conserve la propriété du droit d'auteur qui protège sa thèse. Ni la thèse ni des extraits substantiels de celle-ci ne doivent être imprimés ou autrement reproduits sans son autorisation.

0-612-21642-X

University of Alberta

Library Release Form

Name of Author: Kevin Walter Stapleton

Title of Thesis: Deposition of Medical Aerosols in the Human Respiratory Tract:
Predicting Dosages from Nebulizers, and Deposition in the Mouth-throat using
Computational Fluid Dynamics

Degree: Doctor of Philosophy

Year this Degree Granted: 1997

Permission is hereby granted to the University of Alberta Library to reproduce single copies of this thesis and to lend or sell such copies for private, scholarly, or scientific research purposes only.

The author reserves all other publication and other rights in association with the copyright in the thesis, and except as hereinbefore provided, neither the thesis nor any substantial portion thereof may be printed or otherwise reproduced in any material form whatever without the author's prior written permission.

A handwritten signature in black ink, appearing to read 'K. Stapleton', is written over a horizontal line.

Kevin Stapleton
Zur Bergwiese 5
82152, Planegg
Germany

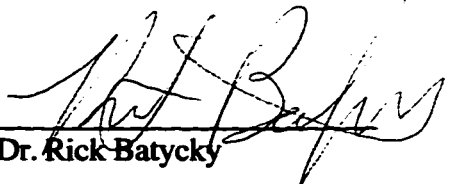
March 10, 1997

University of Alberta

Faculty of Graduate Studies and Research

The undersigned certify that they have read, and recommend to the Faculty of Graduate Studies and Research for acceptance, a thesis entitled "Deposition of Medical Aerosols in the Human Respiratory Tract: Predicting Dosages from Nebulizers, and Deposition in the Mouth-throat using Computational Fluid Dynamics" submitted by Kevin Walter Stapleton in partial fulfillment of the requirements for the degree of Doctor of Philosophy


Dr. Warren H. Finlay


Dr. Rick Batycky


Dr. C. Capjack


Dr. David A. Edwards


Dr. D. J. Wilson

March 10, 1997
Date

Dedication

This thesis is dedicated to the memory of

Ms. Barbara Anne Holmes

May 21, 1956 - Jan 5, 1992

Abstract

A Lagrangian dynamical model for calculating the regional deposition of hygroscopic aerosols in the respiratory tract is presented. The model tracks a bolus of aerosol as it travels through the respiratory tract and calculates the growth of the particles using a full two-way coupled hygroscopic growth model in which the change in aerosol droplet size affects the humidity and temperature of the air in the respiratory tract. The deposition probabilities for a particle in a specific generation are calculated from theoretical and empirical expressions. A method to estimate the intersubject variability is also presented. The deposition probabilities calculated by the model agree well with available experimental data.

A methodology is presented in which experimental methods that characterize the aerosol emitted by jet nebulizers are combined with the deposition model to predict the dosage of medication delivered to the different regions of the respiratory tract. The methodology is applied to the Hudson T-Updraft II nebulizer, and the Pari LC+ nebulizer. The dosage delivered to the lungs by the Hudson is estimated as $16.1 \pm 0.5\%$ (intersubject variability 68% confidence interval: 11.8% - 20.4%) of the nominal dose put in the nebulizer, while the Pari is estimated to deliver $13.0 \pm 0.3\%$ (intersubject variability 68% confidence interval: 9.3% - 16.8%) of the nominal dose to the lung.

Computational fluid dynamics (CFD) is investigated as a tool to predict the deposition of aerosol particles in the mouth and throat by testing a commercially available CFD package (TASCflow3D, ASC, Waterloo, ON) on a number of geometries. For laminar

flow in tubes with simple 90-degree bends, CFD provided accurate predictions of the particle deposition. In the USP model throat, the overall filtering efficiency of the model and the deposition pattern predicted by the CFD agreed poorly with the filtering efficiency and deposition patterns determined experimentally. Finally, the code was tested in a novel geometry that approximates the extrathoracic region of the respiratory tract. Here, the deposition patterns agreed reasonably well with experimentally determined patterns, but the CFD greatly overestimated the deposition compared with experimentally determined values and the values from an empirical equation for the deposition of droplets in the extrathoracic region of the respiratory tract. The poor performance of CFD in the USP model throat and the physiologically realistic throat geometry may be due to the inadequacy of current models of turbulence and turbulent dispersion.

Acknowledgements

An accomplishment such as a PhD thesis cannot be achieved without the support of a great many people. In particular I would like to thank Dr. Warren Finlay for all his advice, support, and guidance over the years. It is difficult for me to imagine accomplishing this with anyone else. I would also like to thank my family, who may be spread all over Canada, but are always close in my heart.

Most importantly, I would like to thank all the people who have been apart of my life over the past 5+ years. You are far too many to mention, but your names, phone numbers, addresses, and notes are written in my daytimer, on my calendars, in my workbooks, and on cards, letters, and oh-so-many e-mail messages. Each and every one of you have added to my life, and in your own way, you have contributed to this work. Thank you.

Kevin Stapleton
Planegg, Germany
March 4, 1997

Table of Contents

1. Introduction	1
2. Deposition Modeling.....	8
2.1 Overview	8
2.2 Morphology and models of the human respiratory tract.....	13
2.2.1 Respiratory tract morphology	13
2.2.2 Heat and vapour transport models	20
2.3 Respiratory tract fluid dynamics.....	22
2.4 Particle deposition mechanisms.....	27
2.4.1 Particle deposition in bifurcating systems of cylindrical tubes.....	27
2.4.1.1 Inertial Impaction.....	27
2.4.1.2 Sedimentation	33
2.4.1.3 Diffusion	35
2.4.2 Extrathoracic deposition	36
2.5 Respiratory tract deposition models.....	37
2.5.1 Calculation of deposition probabilities	37
2.5.1.1 Deposition during inhalation.....	38
2.5.1.2 Deposition during the inspiratory pause	39
2.5.1.3 Deposition during exhalation.....	40
2.5.1.4 Total and Regional deposition.....	40
2.5.1.5 Polydisperse aerosols	41
2.5.2 Hygroscopic effects	41
2.5.2.1 Governing Equations.....	42

2.5.2.2 Solution methodology	48
2.5.2.3 One-way Coupling	48
2.5.2.4 Hygroscopic vs. Nonhygroscopic calculations	50
2.5.3 Intersubject variability	51
2.5.3.1 Calculation of intersubject variability	53
2.6 Comparison with experimental data	58
2.6.1 Regional Deposition of Stable Aerosols	59
2.6.2 Total and Regional Deposition of Hygroscopic Aerosols	63
3. Regional Dosage Predictions from Medical Nebulizers	66
3.1 Introduction	66
3.2 Nebulizer Types	68
3.3 Determining solution concentration within aerosol droplets output by nebulizers	72
3.3.1 Theory	73
3.3.2 Experimental Validation	77
3.3.2.1 Droplet Equilibrium	77
3.3.2.2 Droplet Solution	82
3.3.3 Application to Vented Jet and Ultrasonic Nebulizers	90
3.3.4 Calculation of Reservoir Solution Concentration for Unvented Jet Nebulizers ..	92
3.3.5 Miscellaneous issues	94
3.4 Calculation of Regional Dosage	96
3.4.1.1 Unvented Jet Nebulizers	98
3.4.1.2 Computer Calculations of Regional Dosage	100
3.4.1.3 Results	104
3.4.2 Vented Jet Nebulizers	105

3.4.2.1 Bench Measurements	107
3.4.2.2 Calculation of Regional Dosages.....	108
3.4.2.3 Results.....	109
3.4.3 The Effect of Tapping.....	110
3.4.4 Effect of different treatments of hygroscopic growth	111
3.5 Comparison with other methodologies.....	113
4. CFD studies of particle deposition in the extrathoracic region of the respiratory tract ..	120
4.1 Introduction	120
4.2 Calculation of particle trajectories	125
4.3 Turbulence models and boundary conditions for turbulent flows.....	129
4.4 Physiologically realistic throat model	131
4.5 Particle Deposition in Bent Tubes.....	137
4.5.1 Geometry.....	137
4.5.2 Grid	138
4.5.3 Convergence	141
4.5.4 Results	143
4.6 Deposition in the USP model throat.....	144
4.6.1 Geometry and Grid.....	145
4.6.2 Boundary conditions.....	148
4.6.3 Convergence	148
4.6.4 Experimental studies of aerosol deposition in the USP model throat.....	149
4.6.5 Results	153
4.7 Aerosol deposition in the physiologically realistic throat model	156
4.7.1 Geometry and grid.....	156

4.7.2 Boundary conditions.....	158
4.7.3 Convergence.....	158
4.7.4 Experimental studies of aerosol deposition in the physiologically realistic throat model.....	160
4.7.5 Results.....	161
5. Conclusions.....	120
6. References	169
7. Appendix A.....	183
8. Appendix B	189

List of Figures

Figure 2.1: Classifications of deposition models.....	9
Figure 2.2. The mean end of inhalation temperature of the respiratory tract for inhalation flow rates representative of tidal breathing ($300 \text{ cm}^3/\text{s}$) through single breath inhalation maneuvers ($1500 \text{ cm}^3/\text{s}$) for a Weibel 'A' lung scaled to 3000 cm^3 . Data from Daviskas <i>et al.</i> (1990).....	21
Figure 2.3. The mean end of inhalation relative humidity of the respiratory tract for inhalation flow rates representative of tidal breathing ($300 \text{ cm}^3/\text{s}$) through single breath inhalation maneuvers ($1500 \text{ cm}^3/\text{s}$) for a Weibel 'A' lung scaled to 3000 cm^3 . Data from Daviskas <i>et al.</i> (1990).	21
Figure 2.4. Plot of Stokes number (Equation 2.10) vs. lung generation for the Weibel 'A' model lung for three particle sizes and two flow rates.	29
Figure 2.5. Common equations used to predict deposition due to impaction in deposition models.	32
Figure 2.6. Normalized standard deviation vs. particle size for the extrathoracic region showing the 3rd order polynomial fit used in the model. Data from Lippmann & Albert (1969), and Foord <i>et al.</i> (1978).	55
Figure 2.7. Normalized standard deviation vs. particle size for the tracheo-bronchial region showing the 3rd order polynomial fit used in the model. Data from Lippmann & Albert (1969), Chan & Lippmann (1980), Foord <i>et al.</i> (1978), Emmett <i>et al.</i> (1982), and Lourenço <i>et al.</i> (1971).	55
Figure 2.8. Normalized standard deviation vs. particle size for the alveolar region showing the 3rd order polynomial fit used in the model. Data from Lippmann & Albert (1969), Chan & Lippmann (1980), Foord <i>et al.</i> (1978), Emmett <i>et al.</i> (1982), and Lourenço <i>et al.</i> (1971).	56

Figure 2.9. Normalized standard deviation vs. particle size for total deposition in the respiratory tract showing the 3rd order polynomial fit used in the model. Data from Lippmann & Albert (1969), Chan & Lippmann (1980), and Foord <i>et al.</i> (1978).....	56
Figure 2.10: Experimental data on the deposition of stable particles in the extrathoracic region of the respiratory tract and the mean deposition and 68% confidence interval predicted by the model for a flow rate of 400 cm ³ /s and a tidal volume of 0.7 litres. .	60
Figure 2.11. Experimental data on the deposition of stable particles in the tracheo-bronchial region of the respiratory tract and the mean deposition and 68% confidence interval predicted by the model for a flow rate of 400 cm ³ /s and a tidal volume of 0.7 litres.....	60
Figure 2.12. Experimental data on the deposition of stable particles in the alveolar region of the respiratory tract and the mean deposition and 68% confidence interval predicted by the model for a flow rate of 400 cm ³ /s and a tidal volume of 0.7 litres.....	61
Figure 2.13. Experimental data on the deposition of stable particles in the tracheo-bronchial region of the respiratory tract and the mean deposition and 68% confidence interval predicted by the model for a flow rate of 400 cm ³ /s and a tidal volume of 0.7 litres. Iron oxide particles are corrected for hygroscopic growth.	61
Figure 2.14: Experimental data on the total deposition if initially solid hygroscopic NaCl particles and the mean deposition and 68% confidence interval predicted by the model for a flow rate of 500 cm ³ /s and a tidal volume of 1.0 litres.	63
Figure 3.1. A schematic of an unvented jet nebulizer (2) with attached T-mouthpiece (1). The nebulizer has a reservoir (3), a venturi (4), and baffles (5). The aerosol produced by the nebulizer is mixed with ambient air at (6), which is also the point that the droplet size distribution is measured by the PDA system.	69

Figure 3.2. A schematic of a vented jet nebulizer (2) and attached mouthpiece (1) shown during inhalation. The nebulizer includes the reservoir (3), venturi (4) and baffles (5). Here, when the patient inhales, air is drawn through the open inlet valve (6). During exhalation, the inlet valve (6) closes, and air is expelled through the exhalation valve (7).....	70
Figure 3.3. A schematic of an ultrasonic nebulizer (2) and attached mouthpiece (1) shown during inhalation. The nebulizer includes the reservoir (3), pizo-electric crystal (4) and baffles (5). Here, when the patient inhales, air is drawn through the inlet valve (6). During exhalation, the inlet valve (6) closes, and air is expelled through the exhalation valve (7). The electronics for the piezo-electric crystal are not shown.	71
Figure 3.4. A schematic of the control volume around a jet nebulizer.....	74
Figure 3.5: A schematic of a vented jet nebulizer with a length of tube attached vertically for measuring the equilibrium condition of the aerosol leaving the nebulizer. The asterisk marks the approximate measuring point.....	77
Figure 3.6. The change in average diameter of droplets with time after leaving the nebulizer, and before interacting with the ambient air. The dotted lines indicate the measurement error of the phase Doppler anemometer (4%).....	79
Figure 3.7. The change in average GSD of the droplet distribution with time after leaving the nebulizer, and before interacting with the ambient air. The dotted lines indicate the measurement error of the phase Doppler anemometer (4%).....	79
Figure 3.8. A schematic of the experimental setup to collect the solids output by a nebulizer. The nebulizer (1) is attached to the filter (3) via a short section of tube (2) with holes to allow ambient air to be entrained to match the flow rate of the vacuum pump. The nebulizer and vacuum pump are attached to the test aparatus via hosing (5) and (6) respectively	83

Figure 3.9. Plot of the temperature of the air exiting the nebulizer as a function of time (points with error bars) and Equation 3.8).....	84
Figure 3.10. Measured concentration of the reservoirs solution for 8 PulmoNeb disposable nebulizers given in Table 3.1 and the values predicted by Equation (3.11). Error bars indicate standard error of the measurements.	94
Figure 3.11. A flowchart for the program to calculate the dosage delivered to different regions of the respiratory tract.	97
Figure 3.12. A schematic of the experimental setup for a vented jet nebulizer. The nebulizer and mouthpiece (1) and compressor are placed in a chamber (5) with controlled temperature and relative humidity. It is attached via hosing (2) to a measuring volume (3) where the size distribution is measured with the PDA (laser beams, 7). The measuring volume is connected via hosing (4) to the breathing simulator.....	106
Figure 3.13. The regional dose delivered by the Hudson T Updraft II and the Pari LC+ nebulizers. Test conditions were 50% RH, 23°C. Dosages are for an average Caucasian male with an inhalation flow rate of 300 cm ³ /s and a tidal volume of 0.75 liters. Error bars on the graph indicate the standard error in the measurements.....	110
Figure 3.14. The effect of tapping the nebulizer at a rate of approximately 4 taps per second during the nebulization session. The total dosage delivered to the respiratory tract increased from 0.261±0.005 mg (10.4±0.2% of nominal dose) to 0.352± 0.006 mg (14.1±0.2% of nominal dose), an increase of 35%. The regional distribution of the dose did not change. The inhalation flow rate was 300 cm ³ /s tidal volume 0.75 liters, and ambient conditions were 23°C and 26% RH. All values mean ± standard error.....	111

Figure 4.1. A schematic representation of the mouth and pharynx showing the cephalometric variables measured by Pae <i>et al.</i> (1994). Dimensions used in the creation of the model throat described here include: 1, tongue length; 2, tongue height; 4, maximum palate thickness; 7, inferior airway space; 8, vertical airway length.....	132
Figure 4.2. An isometric view of the physiologically realistic throat model showing the mouth, larynx, and pharynx. A square inlet is added to the front teeth. Note that the trachea has a total length of approximately 10 cm and extends out of the picture to allow for a more detailed view of the mouth and pharynx. The epiglottis is not shown in this view.	136
Figure 4.3: A view of the geometry through the symmetry plane showing the epiglottis and the internal structure of the model.....	136
Figure 4.4. A schematic of the geometry of the bent tube. The diameter of the pipe is exaggerated for display purposes.....	138
Figure 4.5. A partial view of the mesh used in the calculations showing the inlet and the mesh cross section. The large dot indicates the location of the end of the grid line used in the grid convergence studies.....	139
Figure 4.6. A plot of the speed of the fluid along a gridline for the three grid densities showing that the increasing the resolution of the grid beyond the base grid does not increase the accuracy of the results..	140
Figure 4.7. A plot of the pressure drop of the fluid along a gridline for the three grid densities showing that the increasing the resolution of the grid beyond the base grid does not increase the accuracy of the results.....	140
Figure 4.8. A typical plot of the dimensionless RMS residuals at each timestep for the calculations. In all cases, the maximum residuals at any grid point are less than one	

order of magnitude greater than the RMS value indicating that there are no local areas of high error.....141

Figure 4.9. A summary table of the mass flows from the same run shown in Figure 4.7.

It can be seen that the net flow is approximately 5 orders of magnitude lower than the average values on the boundaries for X and Y momentum and conservation of mass.142

Figure 4.10. The calculated deposition in a tube with a 90° bend compared to

experimental, theoretical, and other computational results. The results all show good agreement.144

Figure 4.11. A view of the mesh for the USP model throat. The flow enters parallel to

the X-axis, and exits at the bottom.....146

Figure 4.12. The grid for the USP model throat through the symmetry plane. the thick

line gives the approximate location of the grid line used in the grid convergence studies.....146

Figure 4.13. A plot of the speed of the fluid along a gridline for three grid resolutions of

the USP model throat showing that increasing the resolution of the grid beyond the base grid results in only a slight increase in accuracy (<1% at all points).....147

Figure 4.14. A plot of the pressure drop of the fluid along a gridline for three grid

resolutions of the USP model throat showing that increasing the resolution of the grid beyond the base grid results in only a slight increase in accuracy (<1% at all points).147

Figure 4.15. Mass flow summary for the flow solution on the base grid used in the

particle tracking calculations. The “Net Flow” in the X-momentum and Y-momentum is approximately 4 orders of magnitude less than the boundary values, and the “Net Flow” in continuity approximately 5 orders of magnitude lower than the boundary values.....149

Figure 4.16. A schematic of the experimental setup used to determine the deposition of radiolabelled aerosols in the USP throat model. The nebulizer (1) is attached to the USP throat model (2) via heat-shrink tubing. Aerosol passing through the model is collected on a filter (3) attached to a vacuum pump via hosing (4).....	150
Figure 4.17. A greyscale image of the deposition of radiolabelled aerosol in the USP model throat. Air enters on the left, and exits on the bottom. The darker areas correspond to areas of higher deposition.	152
Figure 4.18. Tracks of massless particles in the USP model throat viewed from the side of the model. The flow enters from the right, and exits out the bottom.....	154
Figure 4.19. Tracks of massless particles in the USP model throat viewed from the top of the model. The flow enters from the left, and exits into the page.....	154
Figure 4.20. Calculated deposition pattern for the USP model throat. (a) shows the pattern for a monodisperse aerosol equal to the MMAD of the aerosol produced by the nebulizer used in the experimental tests. (b) shows the calculated deposition pattern for a polydisperse aerosol with an MMD and GSD equivalent to the aerosol produced by the nebulizer.	155
Figure 4.21: Experimental deposition in the USP model throat. This figure uses the same data as Figure 4.17, and is shown here for comparison purposes.	155
Figure 4.22. A cross sectional view of the base grid for the physiologically realistic throat model. The thick lines indicate the approximate location of the grid lines used in the grid convergence studies.....	157
Figure 4.23. A summary table of the mass flows for the converged solution on the base grid used for the particle deposition calculations.....	158

Figure 4.24. A plot of the speed of the fluid along the two grid lines for the three grid densities showing that increasing the grid resolution beyond the base grid does not increase the accuracy of the results. LR=low resolution. HR=high resolution.....	159
Figure 4.25. A plot of the pressure drop in the fluid along the two grid lines for the three grid densities showing that increasing the grid resolution beyond the base grid does not increase the accuracy of the results. LR=low resolution. HR=high resolution..	159
Figure 4.26. A greyscale image of the deposition of radiolabelled aerosol in the mouth and pharynx of the model throat. The deposition mainly occurs on the surface of the tongue and the bottom of the larynx.	160
Figure 4.27. A greyscale image of the deposition of radiolabelled aerosol in the pharynx (a) and in the trachea (b). In (a), the bright spot corresponds to the bottom of the pharynx. In (b), the bright spot corresponds to the larynx. Significant deposition is also observed on the superior surface of the epiglottis.....	161
Figure 4.28: Calculated deposition pattern for the physiologically realistic throat model compared with the experimental results. (a) shows the deposition pattern in the trachea calculated with a monodisperse aerosol, (b) shows the experimental results (same data as Figure 4.27), and (c) shows the deposition pattern calculated using a polydisperse aerosol.	162
Figure 4.29: Calculated deposition pattern for the physiologically realistic throat model compared with the experimental results. (a) shows the deposition pattern calculated using a monodisperse aerosol, (b) shows the deposition pattern calculated using a polydisperse aerosol.	163
Figure 4.30: Experimental results of deposition in the mouth and pharynx. Same data as Figure 4.26.	163

List of Tables

Table 2.1. The dimensions of the Weibel 'A' model scaled to 3000 cm ³	15
Table 2.2. Values of the coefficients for the 3rd order polynomial fits to the normalized standard deviation vs. particle size data, where $\sigma_{n,norm} = a * d_n^3 + b * d_n^2 + c * d_n + d$	57
Table 3.1. Total mass Δm_{neb} leaving the nebulizer during each minute, the mass of solids m_s collected on the filter during each minute, and the measured concentration of the solute in the nebulizer solution at the end of each minute, for an initial volume of 5.0 ml in the nebulizer. All values are mean \pm standard error.....	84
Table 3.2. The calculated average concentration of the solution in the droplets over one minute of nebulizer operation compared to the concentration of the nebulizer solution measured at the end of the minute for an initial concentration of the nebulizer solution of 10.0 mg/ml (1.0 mg/ml salbutamol sulfate, and 9.0 mg/ml NaCl). All values are mean \pm standard error.....	87
Table 3.3. The calculated average concentration of the droplets produced by the nebulizer when averaging over different time intervals with Equation (3.5) from the data in Table (3.1). The measured concentration of the nebulizer reservoir solution at the end of the 7th minute of operation was 11.28 \pm 0.04 mg/ml.	87
Table 3.4. Total mass leaving the nebulizer during each minute, and the final concentration of solids (salbutamol sulfate and NaCl) in the nebulizer solution at the end of the nebulization period. All values are mean \pm standard error. The value in parentheses indicates the nebulized mass as a percentage of the initial mass of solution in the nebulizer	99
Table 3.5. Regional dosage of Ventolin [®] delivered to the respiratory tract by the Hudson T Updraft II nebulizer as a percentage of the nominal dose in the nebulizer. Individual	

dosage for 68% of the population would fall within the given ranges. Calculations are for a tidal volume of 0.75 liters, and an inhalation flow rate of 300 cm ³ /s.	104
Table 3.6. Regional dosage of Ventolin [®] delivered to the respiratory tract by the Pari LC+ nebulizer as a percentage of the nominal dose in the nebulizer. Individual dosage for 68% of the population would fall within the given ranges. Calculations are for a tidal volume of 0.75 liters, and an inhalation flow rate of 300 cm ³ /s.	109
Table 3.7. The percent of the nominal dose put in the nebulizer delivered to different regions of the respiratory tract calculated with three different treatments of the hygroscopic growth calculations. Total lung deposition is the sum of alveolar and bronchial deposition. All values are mean ± standard error.	113
Table 3.8. Comparison of the results of Ferron <i>et al</i> (1997) Figures 6 & 7 to the model presented here for an aerosol with an MMD of 2.8 µm and a GSD of 2.3. Results from our model for the droplet growth 30 seconds after creation differ in the 5th significant digit from those at 3.0 seconds and are not presented.	117
Table 4.1. Calculated total deposition in the USP throat model showing the effect of using a monodisperse vs. a polydisperse aerosol, and the effect of the turbulent tracking. The experimentally determined value is 5.9%	153
Table 4.2: Calculated total and regional deposition in the physiologically realistic throat model showing the effect of using a monodisperse vs. polydisperse aerosol. All values are a percentage of the total mass of aerosol entering the model.....	162

Symbols and Abbreviations

Letters

A	volume of droplets leaving the nebulizer per unit volume of air
BDF	backward differentiation
CFD	computational fluid dynamics
CT	computed tomography
C_{cor}	drag coefficient for spheres
C_f	number of photons emitted by the filter after exposure
C_m	number of photons emitted by the model after exposure
C_{p_a}	specific heat of air
C_{p_w}	specific heat of water
C_w, C_K	Knudsen correction
C_R	vapour pressure reduction at the surface of a droplet due to dissolved solids (e.g. Raoult's Law for ideal solutions)
c_o	water vapour concentration at the droplet surface (g/cm ³)
$c(t)$	concentration of solute in a droplet at time t
\bar{c}_{wall}	the average concentration of water at the airway walls
c_w	water vapour concentration
$c_{w,in}$	water vapour concentration of air entering a nebulizer
$c_{w,out}$	water vapour concentration of air leaving a nebulizer
$(\bar{c}_-^0)_k$	the average water vapour concentration of the continuous phase in the k th generation

c_{∞}	ambient water vapour concentration (g/cm ³)
d	diameter (of particle, droplet, or airway)
D	diameter of tube
D_w	diffusion coefficient of water in air
DE	deposition fraction
DPI	dry powder inhaler
F	external forces acting on a particle
f_k	fraction of inhaled aerosol that penetrates to the k th generation
g'_k	mass transfer coefficient in the k th lung generation
GSD	geometric standard deviation
h	diffusion parameter (Equation 2.18)
h'_k	heat transfer coefficient in the k th generation
k	turbulence kinetic energy
l	turbulence length scale
l_e	average size of a turbulent eddy
L	length, latent heat of vaporization
m	mass
\dot{m}'_{wall}	mass transfer of water vapour from the airway walls to the air
MDI	metered dose inhaler
MMAD	mass median aerodynamic diameter
MMD	mass median diameter
MRI	magnetic resonance imaging
$O(n)$	on the order of (n)
P	statistical probability

P_n	deposition probability
$P_{n,upper}$	upper bound of the 68% confidence interval on the deposition probability
$P_{n,lower}$	lower bound of the 68% confidence interval on the deposition probability
PDA	phase Doppler anemometer
Q	volumetric flow rate
\dot{q}'_{wall}	heat transfer from the airway walls to the air
Q_{ci}	conductive heat transfer
Q_m	latent heat transfer
r	radius
Re	Reynolds number
RMS	root mean square
SF	scaling factor for lung model dimensions
S	stopping distance
Stk	Stokes number
t	time
T	temperature
T_ϵ	characteristic dissipation timescale
$(\bar{T}_{wall} - \bar{T}_\infty)_k$	difference between the average wall temperature and temperature of the continuous phase in the k th generation.
USP	United States Pharmacopeia
U	fluid velocity, fluid velocity in X-direction
u_τ	friction velocity
V	volume
V_{dead}	instrumental dead space

V_0	initial volume of liquid in the nebulizer
v_f	fluid velocity
v'_f	instantaneous velocity of a turbulent eddy
v_p	particle velocity
v_s	settling velocity
V_T	tidal volume
W	volume of water vapor leaving the nebulizer per unit volume of air
x_h	hydrodynamic entrance length
x_i^o	old particle position
x_i^n	new particle position
\hat{y}	dimensionless distance from the wall

Subscripts

A	alveolar region of the respiratory tract
ae	aerodynamic
a, air	air
E	extrathoracic region of the respiratory tract
f	fluid
i	value at a particle surface
k	lung generation
l	liquid
o	initial value
p	particle
s	solid

<i>TB</i>	tracheobronchial region of the respiratory tract
<i>v</i>	vapour
<i>wall</i>	value at the wall

Superscripts

<i>hold</i>	inspiratory pause in the breathing cycle
<i>in</i>	inhalation portion of the breathing cycle
<i>n</i>	value at the new timestep
<i>o</i>	value at the old timestep
<i>out</i>	exhalation portion of the breathing cycle

Greek symbols

α	bifurcation angle
β	angle with horizontal (Equation 2.16)
$(\Delta c_{\infty}^0)_k$	the change in water vapour concentration between the beginning and end of the <i>k</i>th generation when no droplets are present
Δm_{neb}	change in total mass of a nebulizer
Δt_k	average residence time of a particle in a generation
$(\Delta T_{\infty}^0)_k$	temperature change in the continuous phase between the proximal and distal ends of the <i>k</i>th generation
δt	timestep for integration of particle trajectories
ε	sedimentation parameter (Equation 2.15), and turbulence dissipation
ϕ	ventilated fraction
η	filtering efficiency

κ_a	thermal conductivity of air
ρ	density
$(\bar{\rho}_{air}^0)_k$	average density of air in the k th generation
$\sigma_{n, norm}$	normalized standard deviation
τ_e	eddy lifetime
τ_w	wall shear stress
μ	dynamic viscosity
ν	kinematic viscosity
ψ	fraction of inhaled air passing through the mouth
∞	ambient, at infinity

1. Introduction

Aerosols are airborne suspensions of particulate matter, and are a natural component of our environment. The troposphere, i.e. the lowest 10 km or so of the atmosphere, contains between 10^2 and 10^6 particles per milliliter, most of which fall into the size range of 0.01-1.0 μm (Morrow, 1974). These particles are inhaled during normal respiration, and may be deposited in the respiratory tract by coming into contact with the surface of the airways. The deposition of inhaled particles has a probability that depends on the aerodynamic and thermodynamic properties of the particles, the morphology of the respiratory tract, and the airflow and mixing behavior in the airways. Inhaled particles may include toxic agents whose deposition in the respiratory tract may have adverse effects on the body. For this reason, predicting the deposition of these particles in the respiratory tract has attracted considerable interest.

The respiratory tract has elaborate defenses against particles that occur naturally in the atmosphere. The morphology and fluid mechanics of the respiratory tract have evolved so those particles in the size range most prevalent in the atmosphere (i.e. particles with diameters on the order of a few tenths of micrometers) have the least chance of depositing. Particles with diameters on the order of a few micrometers tend to deposit in

the conducting airways and are removed by the muco-ciliary transport system over a number of hours. Larger particles tend to deposit in the mouth and pharynx, and are quickly removed by coughing through the mouth, or swallowing and being passed through the digestive tract. Particles smaller than about $0.01\text{ }\mu\text{m}$ have quite high probabilities of depositing in the lungs, but do not occur frequently in the natural atmosphere and do not carry much mass, so their toxicological effects are usually minimal.

Industrial society has significantly changed the aerosols found in the atmosphere. Many of these aerosols are toxic, and are of different sizes than those seen naturally in the atmosphere, so the body is ill equipped to defend against them. This leads to the possibility of inhaled particles depositing in the respiratory tract and damaging the delicate tissues in the lungs thereby impairing its effectiveness, and of toxic chemicals gaining easy access to the circulatory system and being spread throughout the body.

These concerns have generated considerable interest in being able to predict the deposition of aerosols in the respiratory tract, with the goal of predicting the effects of human exposure to hazardous environments. Techniques have been developed to study the deposition of aerosols in the respiratory tract *in vivo*, and empirical models have been developed. Concurrently, research on aerosol behavior has lead to a greater understanding of the physics of aerosol deposition in the respiratory tract, and to the development of deposition models based on the theoretical expressions for the deposition of aerosol particles in tubes. The structure and functionality of the respiratory tract is an important feature of these deposition models, and their development has encouraged an

improved understanding of the morphology, fluid dynamics, and functionality of the human respiratory tract.

In the past century, aerosolized drugs (therapeutic aerosols) have been used to treat respiratory tract diseases and are the preferred means of delivering some medications (c.f. Williams, 1974). However, the performance and efficiency of devices used for producing therapeutic aerosols differ greatly, and it has been suggested that unsatisfactory clinical results may be due in part to the improper selection and operation of this equipment (Newman *et al.* 1986). Procedures which allow estimation of delivered dosages from these devices are useful in improving the device design and delivery protocols for therapeutic aerosols, and many of the techniques used to study the deposition of hazardous aerosols in the respiratory tract have been applied to the deposition of therapeutic aerosols to improve the efficiency and efficacy of aerosol therapy.

There are three types of devices that are commonly used for producing and delivering therapeutic aerosols. Nebulizers produce aerosol from a drug formulated as a solution, or as a suspension, using conventional air-water spray atomization technology. Metered dose inhalers (MDIs) contain a pressurized cylinder with drug, propellant, and excipients. Actuating the MDI results in a spray containing a precisely metered dose of the medication being released from the canister. MDIs are inexpensive and convenient, but are inefficient when not used correctly. In a dry powder inhaler (DPI), the drug is formulated as a powder, and the device is similar in size, cost and convenience to an MDI. However, for effective deposition in the lungs, DPIs require a minimum inhalation

flow rate that small children or patients with severe respiratory distress may not be able to accomplish.

Studies comparing the performance of these devices have often sided with MDIs because of their relatively good performance, convenience, and low cost. However, caution should be used when applying these results in general, since some of the devices used in these studies are much less efficient than newer devices (Finlay *et al.* 1997a). Reviews of aerosol therapy techniques and devices (e.g. Consensus Conference on Aerosol Delivery, 1991) discuss the advantages and disadvantages of each device type, and identify specific areas where each device type is most effectively used. Nebulizers excel at delivering large doses of medications to the lung (e.g. 15-20 mg/hr), and delivering medication over long periods of time during tidal breathing.

This manuscript addresses many of the issues surrounding the deposition of therapeutic aerosols in the respiratory tract, and in evaluating the performance of nebulizers. Issues involved in the performance and deposition from MDIs and DPIs is an area of ongoing research, although many results are available in the archival literature, and the reader is referred there for details.

Two dimensional (2-D) gamma scintigraphy is used in many clinical investigations of nebulizer deposition to estimate the amount of aerosol deposited in the extrathoracic, central, and peripheral regions of the lungs (Matthys & Köhler 1985, Johnson *et al.* 1989, Ilowite *et al.* 1991). These *in vivo* studies show a marked difference in the total deposition and the deposition pattern of a specific drug delivered by different nebulizers, and a specific nebulizer delivering different drugs. This indicates that

different drugs may need to be tested with each nebulizer to determine the most effective combination.

Difficulties in determining regional deposition using 2-D gamma scintigraphy have been discussed by Trajan *et al.* (1984). In particular, the three dimensional (3-D) structure of the lung is collapsed onto a 2-D image, making it difficult to estimate the true 3-D distribution of the aerosol. Single photon emission computed tomography (SPECT) provides 3-D images of the lung, and improved estimates of the ratio of aerosol deposited in the peripheral vs. central regions of the lung (Logus *et al.* 1984, Phipps *et al.* 1989), but the cost, complexity, and duration of the procedure limits its use (Logus *et al.* 1984). In addition, difficulties in determining gamma ray attenuation makes absolute dosage estimation difficult, limiting the results supplied by many researchers to relative dosage distribution estimates (e.g. penetration index).

Another method of investigating nebulizer performance, which is often used to compare different delivery systems (e.g. nebulizers vs. MDIs), is to consider the clinical effect of the delivered medication on respiratory system performance, often characterized by FEV₁ (Zainudin *et al.* 1990, Blake *et al.* 1992). This methodology provides physicians with estimates of how much medication to prescribe to their patients, but can not parametrically characterize the performance of the devices in detail, or provide a measure of the distribution of the medication in the respiratory tract.

As an alternative to costly and time-consuming clinical measurements, nebulizers are often characterized on the bench by collecting the aerosol on filters. These studies provide some information on the efficiency of the aerosol generation capabilities of the nebulizer, but they do not include any information on the inhalability of the aerosol, and

its probable sites of deposition in the respiratory tract. Most often, this information is combined with a characteristic description of the produced aerosol, usually in the form of a 'respirable fraction'. The respirable fraction is loosely defined as the percentage of the aerosol (by mass) contained in particles between 1 μ m and 5 μ m (or between 1 μ m and 6 μ m, or some other definition, depending on the author) which is generally viewed as the particle size range with the highest probability of deposition in the lungs. However, Finlay *et al.* (1997b) have shown that respirable mass is not a useful measure of nebulizer performance for many aerosol sizes.

This manuscript presents a different approach to the evaluation of nebulizer performance. A deposition model based on theoretical expressions for the deposition of aerosol particles in a model of the respiratory tract is used to predict the deposition patterns of the aerosol output by the nebulizer. Part 2 discusses the development of this model. Part 3 describes how the output of a nebulizer can be measured so it can be combined with the deposition model to produce regional dosage estimates as a method of evaluating nebulizer performance.

The downfall of these current evaluation methods is that at best they can predict regional deposition patterns, i.e. they do not address the local sites of deposition in the airways. For example, for mouth breathing, only one dosage or deposition probability is given for extrathoracic deposition, and there is no indication of the amount of aerosol deposited on the tongue vs. the larynx. In addition, while the predicted deposition is in reasonable agreement with population averages, these methods are not able to predict the deposition in individual subjects.

One technique that can overcome the previously mentioned deficiencies is computational fluid dynamics (CFD). CFD uses computers to solve the mathematical equations that describe fluid flow and particle motion, and may be able to be used to study the airflow and particle deposition in the respiratory tract. However, the airflow in the respiratory tract is complex, and accurate results may not be achievable under certain circumstances with current CFD technology. Part 4 of this manuscript discusses some issues that must be considered when using CFD techniques in the respiratory tract, and compares results of simulations of particle deposition in a model of the extrathoracic region to experimental data.

2. Deposition Modeling

2.1 Overview

A deposition model is a series of equations that predict the probability that a particle will deposit in the respiratory tract. There are a number of different types of deposition models described in the literature, and it is useful to define the descriptive terms used in this thesis. Here, we divide deposition models into two major categories: empirical models, and dynamical models. Empirical models consist of equations based solely on empirical curve fitting of data, and consist of models in which the equations are fit to experimental data, as well as models where the equations are fit to other data. (For example, the empirical model of Rudolf *et al.* (1990) duplicates the results of the Eulerian dynamical model of Egan & Nixon (1985)). Dynamical models are based on the dynamics of fluid flow and particle motion in the respiratory tract and are differentiated by the frame of reference used to describe the motion: an Eulerian model uses a fixed reference frame, while a Lagrangian model follows an aerosol bolus as it travels through the lung. Here, we discuss the development of a Lagrangian dynamical model.

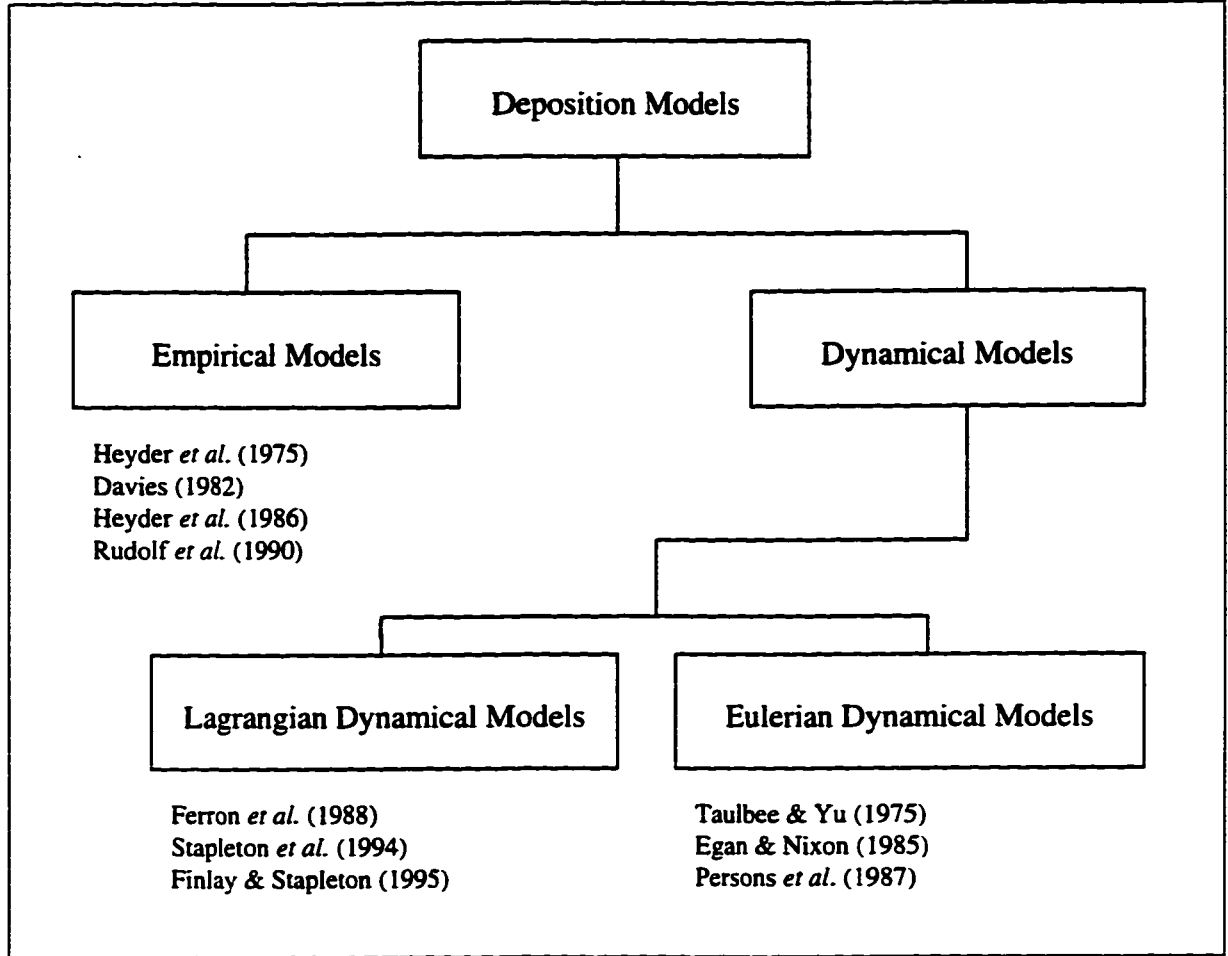


Figure 2.1: Classifications of deposition models

During breathing, air passes through different anatomical regions of the respiratory tract. Particles that do not deposit in the first region are passed to the second region, where they may deposit, or be passed on to the next region. It is therefore convenient to think of the different regions of the respiratory tract as filters, and equations can be written which describe the filtering capabilities of the region. On inhalation, aerosol passes in through the filters, each filter removing a percentage of the suspended particles. On exhalation, the aerosol passes back out through the same filters before exiting the respiratory tract.

The equations describing the filtering efficiency or deposition probability (the terms are used interchangeably here) in empirical deposition models typically depend only on the particle size, the tidal volume, and breathing frequency. Heyder *et al.* (1975) and Davies (1982) present empirical models for the total deposition of aerosol particles in the respiratory tract. Both models have only one equation, and therefore would correspond to having one filter representing the entire respiratory tract.

A multi-filter empirical model is presented by Heyder *et al.* (1986), which can predict aerosol deposition in the extrathoracic, bronchial, and alveolar regions. The deposition in the extrathoracic region, DE_E , is given by:

$$DE_E = \eta_E \phi_E \quad (2.1)$$

where η_E is an empirical expression for the deposition probability in the extrathoracic region, and ϕ_E is the fraction of the tidal volume that passes entirely through the extrathoracic region. The deposition in the tracheobronchial region, DE_{TB} , is given by:

$$DE_{TB} = (1 - \eta_E) \eta_{TB} \phi_{TB} \quad (2.2)$$

where η_{TB} is an empirical expression for the deposition probability in the tracheobronchial region, $(1 - \eta_E)$ represents the fraction of the initially inhaled aerosol which is available for deposition in the tracheobronchial region, and ϕ_{TB} is the fraction of the tidal volume that passes entirely through the tracheobronchial region.

Lagrangian dynamical deposition models are similar in concept, but may have more filters. The model described in this thesis has 51 filters, one filter for each generation of the lung model on inhalation and exhalation, and the deposition in filter k is given by:

$$DE_k = \left(\prod_{i=0}^{k-1} (1 - \eta_i) \right) \eta_k \phi_k \quad (2.3)$$

The difference between empirical and dynamical deposition models is the form of the equations for the deposition probabilities, η_k . In empirical models, the deposition probabilities are based on empirical fits to experimental data. In Lagrangian dynamical models, these equations are based on the physics of particle transport through an idealized lung model.

Lagrangian dynamical deposition models are based on the work of Findeisen (1935) who studied the deposition of NaCl aerosols in animal lungs, and recognized that aerosol deposition in the lungs was governed by the same physical laws that govern aerosol behavior in the atmosphere. By combining these laws with a simplified lung model, Findeisen was able to develop the first particle deposition model for humans.

Recent improvements in aerosol deposition modeling have occurred due to improved morphometric descriptions of the lungs, and a better understanding of aerosol behavior in systems of bifurcating tubes. Many of these improvements were spurred on by the development of improved *in vivo* imaging techniques, and a better understanding of *in vivo* aerosol deposition.

Structural differences between deposition models are reviewed in detail Heyder, & Rudolf (1984) for deposition models published before 1984. Heyder & Rudolf identify three “primary deposition models”, or “formalisms” upon which all others are based. The first primary deposition model was presented by Findeisen (1935), and is characterized by treating the respiratory tract as a system of discrete morphometric regions. Particles are removed from the air flowing through these regions by gravitational, inertial, and

diffusional forces. Breathing is approximated as a pattern of constant flow with adjustable periods of inhalation and exhalation. This type of model lends itself to empirical and Lagrangian dynamical deposition models and the description of a deposition model as a series of filters. The second primary deposition model identified by Heyder & Rudolf was presented by Altshuler (1959). Here, the respiratory tract is treated as a spatially continuous filter, but the breathing pattern is treated similarly to Findeisen primary deposition models. This formalism is rarely used. The third primary deposition model identified by Heyder & Rudolf was first presented by Taulbee & Yu (1975), although Pack *et al.* (1972) present a similar gas transport model which was later modified into a deposition model by Egan & Nixon (1985). Here, the respiratory tract is approximated by a channel with a variable cross-section along its one-dimensional length, and breathing is accounted for in the boundary conditions for the gas and aerosol transport equations. This formalism lends itself to Eulerian dynamical models. Since 1984, a model based on the Taulbee & Yu formalism has been presented by Persons *et al.* (1987), and models based on the Findeisen formalism have been presented by Ferron *et al.* (1988a, 1988b), the ICRP (1994), as well as the model presented here.

The following section describes the development of our Lagrangian dynamical regional deposition model. This thesis is not intended to be a comprehensive review of all aspects of pulmonary function and deposition modeling, and only deals with subjects directly involved in the development and use of our model.

2.2 Morphology and models of the human respiratory tract

2.2.1 Respiratory tract morphology

The human respiratory tract consists of the lungs and a series of passageways through which air is passed through the body to the lungs. Early studies of the structure of the lungs focused on the anatomical features, and it wasn't until the work of Findeisen (1935), and D'Arcy Thompson (1942) that modern engineering principles were applied to the flow of air in the body.

Thompson (1942) showed that biological systems obey the 'principle of similitude', that is, they do not violate basic physical laws in their development. Thompson showed that the asymmetrical dichotomous branching pattern seen in the lungs is consistent with the concepts of minimal energy loss and minimum volume. Indeed the lungs are a remarkable organ in that they provide a surface area of approximately 150 m^2 for gas exchange between the atmosphere and the blood stream in a volume of between 5 and 6 liters.

One of the first comprehensive morphological studies of the lungs was done by Weibel (1963). In his classic monograph, Weibel studied casts of 5 subjects, and presented average values for the dimensions of each generation of the bronchial tree. Dimensions for the first 10 generations were obtained by direct measurement of lung casts. To estimate the total number of bifurcation generations, Weibel dissected the lungs and studied the acini in detail (an acini is the largest structure in the lungs which contains only respiratory elements, i.e., it contains respiratory bronchioles, alveolar ducts and sacs distal to a single terminal bronchiole). Weibel concluded that most acini were composed

of three generations of alveolar ducts (i.e. ducts completely covered with alveoli), and three generations of transitional bronchi (i.e. ducts partially covered with alveoli). By estimating the number of alveoli on each tube in the acini, and the total number of alveoli in the lung, Weibel calculated that the lungs contained a total of 23 generations of homogeneous dichotomous branching.

Weibel presented his findings as two models; the most widely used of which is the Weibel 'A' model (Weibel 1963). The Weibel 'A' model assumes that the lungs are a network of cylindrical tubes which branch in a regular dichotomous fashion. The lengths and diameters of the first 10 generations are given by the average values from the cast measurements. Weibel's least squares gives the length of a tube in generation k as:

$$L_k(k) = L_0 \cdot e^{-0.92k} \quad (2.4)$$

for $0 \leq k \leq 3$ and $L_0 = 12$ cm, and

$$L_k(k) = L'_0 \cdot e^{-0.17k} \quad (2.5)$$

for $4 \leq k \leq 10$ and $L'_0 = 2.5$ cm, and the diameters as:

$$d(k) = d_0 \cdot 2^{-k/3} \quad (2.6)$$

for $0 \leq k \leq 10$ and $d_0 = 1.2$ cm. It is interesting to note that these functions are consistent with the concept of minimum energy loss (or minimum entropy gain) and minimum space for a network of tubes with a regular dichotomous branching pattern (Thompson 1942, Horsfield & Cumming 1967, Glansdorff & Prigogine 1971). Weibel found that the length and diameter of the terminal bronchiole leading into the acinus was consistent with it being generation 16 in his numbering scheme, and used Equations (2.5) and (2.6) to predict the length and diameters of the remaining conducting (or tracheobronchial) airways. The lengths and diameters of the tubes in the alveolar region (generations 17-

Generation	Length (cm)	Diameter (cm)	Cumulative volume (cm ³)
0	10.26	1.539	19.07
1	4.070	1.043	25.64
2	1.624	0.710	28.64
3	0.650	0.479	29.50
4	1.086	0.385	31.70
5	0.915	0.299	33.76
6	0.769	0.239	35.95
7	0.650	0.197	38.39
8	0.547	0.159	41.14
9	0.462	0.132	44.39
10	0.393	0.111	48.26
11	0.333	0.093	53.01
12	0.282	0.081	59.14
13	0.231	0.070	66.26
14	0.197	0.063	77.14
15	0.171	0.056	90.70
16	0.141	0.051	109.26
17	0.121	0.046	139.32
18	0.100	0.043	190.61
19	0.085	0.040	288.17
20	0.071	0.038	512.95
21	0.060	0.037	925.25
22	0.050	0.035	1694.17
23	0.043	0.035	3000.00

Table 2.1. The dimensions of the Weibel 'A' model scaled to 3000 cm³.

23) are not predicted well by these equations, and Weibel instead used average values from direct measurements of these airways. It should be noted that Weibel measured every generation in each cast up to generation 10, but only a representative sample of the more distal airways.

The Weibel 'A' model is not an accurate description of the respiratory tract for a number of reasons. First, and most obvious, the Weibel 'A' model assumes symmetrical dichotomous branching, whereas the airways in the human lung undergo asymmetric dichotomous branching. Secondly, because of the regular branching pattern, the model overpredicts the number of alveolar airways. However, symmetry and simplicity make it popular for modeling the geometry of the lungs.

The total volume of the Weibel 'A' model is 4800 cm³, which corresponds to approximately 75% of the functional residual volume (FRC) of an adult male (Weibel, 1964). Tidal breathing occurs at approximately 50% FRC, so the dimensions given by Weibel (1963) should be scaled when calculating deposition during tidal breathing.

Hughes *et al.* (1972) studied the effect of lung inflation on the dimensions of the airways in dogs and found that on average, they scaled with the cube root of the lung volume. A scaling factor, SF , can be calculated by:

$$SF = \sqrt[3]{\frac{3000}{4800}} \approx 0.86 \quad (2.7)$$

which when multiplied by the length and diameters of the airways will scale the model to 3 liters.

Hansen and Ampaya (1975) studied the morphology of the acini and proposed modifications to the Weibel 'A' model to overcome some of its shortcomings. They found that the respiratory bronchiolar and alveolar ductural cross-sectional area, and alveolar surface area increased more rapidly with generation than predicted by the Weibel 'A' model, and proposed a model based on their data, and Weibel's data for generations 0-10. Their model has fewer small bronchi and respiratory bronchi (generations 11-20), and has more alveolar ducts than the Weibel 'A' model.

Olson *et al.* (1970) considered the average geometrical parameters of the respiratory tract as well as a 'consideration of the series-parallel arrangement' of the airways in the lungs. They combined data from different lung morphology studies with their own observations of lung function and presented an asymmetric model which closely resembles the Weibel 'A' model, but has fewer airways at higher generations.

Yeh & Schum (1980) took a different approach and considered 'pathways' to alveolar sacs instead of generations of tubes. This focus allows them to consider both asymmetry of the branching structure, and portions of the lungs (e.g. one lobe). Their geometry is derived from measurements of casts, and the branching structure is very similar to Weibel.

Haefeli-Bleuer & Weibel (1988) studied the morphology of the acinus in detail using lung casts, and found that intraacinar airways branch dichotomously over 6-12 generations, with an average of 9 interacinar generations. With their measured acinar volume of 187 mm^3 , they calculated that the entrance to the acinii is at generation 14, a location consistent with the measured length and diameter of the terminal bronchiole as predicted by Equations 2.5 and 2.6. The modifications they propose to the Weibel 'A' model are limited to the length and diameter of generations 15-23, and a change in the location of the start of the alveolar region to the 15th generation.

With this variety of lung models, it is not obvious which is best to use with a deposition model. This issue was addressed by Yu and Dui (1982a) and Martonen (1983), who studied how different lung models would affect the deposition predicted by a mathematical deposition model. Both studies showed that the standard Weibel 'A' model, scaled to 3 liters, gave deposition probabilities which most closely approximated the population average results from experimental studies, and in spite of its morphometrical inaccuracies, it was suitable for use in deposition modeling studies. The deposition model described in this thesis uses a Weibel 'A' model scaled to 3 liters.

All of the above models assume that the lung is a series of cylindrical tubes, and there is no description of how the tubes are joined. This is an important question for

researchers studying the fluid flow in the airways, and the deposition of particles within the bifurcation. Olson (1972) studied the airflow through models of bifurcations obtained by averaging the geometry from over 500 bifurcations in lung casts. Olson (1972) describes the proximal 80% of the parent tube as being cylindrical. The last 20% of the parent airway is a transition zone to the daughter tubes. The cross section becomes more elliptical, while maintaining a constant cross-sectional area. When the minor axis of the ellipse is approximately equal to the radius of the daughter tube, the shape flattens, and the cross-sectional area increases until the carina bisects the tube, and forms the two daughter tubes. The carina is described as a curved wedge, with the radius of curvature proportional to the radii of the daughter tubes.

Heistracher & Hofmann (1995) noted that many researchers studying the flow through airway bifurcations do not specify how the transition region is modeled, and propose a bifurcation model similar to Olson (1972), with slight differences in the radii of curvature of the carina and transition zone.

The shape and size of the mouth, pharynx, larynx, and upper part of the trachea, which comprise the extrathoracic airways of the respiratory tract, are not as well defined, or modeled, as the lower airways. Many researchers creating computer models to predict aerosol deposition in the respiratory tract avoid this problem by using an empirical equation to predict deposition in the extrathoracic region, and thereby avoid any description of the extrathoracic airways.

The geometry of the upper airways has been studied by researchers in diverse fields. One such field is sleep disorder research, where craniofacial and pharyngeal morphology are the main contributors to obstructive sleep apnea (OSA) syndrome (c.f.

Lowe 1990). Lowe & Fleetham (1991) and Pae *et al.* (1994) provide the average locations of most anatomical features of the mouth and pharynx in the middle sagittal plane from CT scans of about 35 normal subjects (c.f. Figure 3.1). Rodenstein *et al.* (1990) study the transverse shape of the pharynx, and show that the pharynx is an elliptical cylinder, with the ratio of the major and minor axes dependent on whether the subject is normal, a simple snorer, or a patient with OSA.

Baer *et al.* (1991) used magnetic resonance imaging (MRI) techniques to measure the shape of the vocal tract superior to the glottis. Unfortunately, the measurements were done while the patient was producing vowel sounds, so the data has limited applicability to simple tidal breathing. Sorokin (1992) developed a mathematical model for predicting the shape of the mouth and pharynx, but again the model is focused on the shape of the airway during the production of speech.

The shape and mechanical properties of the larynx and vocal cords were studied and modeled by Titze (1973) and modified by Titze (1989). These models provide a detailed description of the morphology of the vocal cords and the larynx, although they ignore the false vocal cords which were included in the model of Miller *et al.* (1989). Scherer & Titze (1983) studied the fluid flow through models of the larynx, and describe a realistic model consistent with the other studies. The movement of the vocal cords during tidal breathing was studied by Stanescu *et al.* (1972) and Brancatisano *et al.* (1983) who measured the variation in glottal width with time.

The above-cited literature is used to construct an idealized model of the extrathoracic airways suitable for study with computational fluid dynamics techniques. Details of the model are given in Section 4.2.

2.2.2 Heat and vapour transport models

Inspired air needs to be conditioned to 37°C and 99.5% RH before it reaches the alveoli to ensure normal functioning of the lungs. This conditioning normally requires heat and vapour transport from the walls of the airways to the inspired air. Cole (1953) and Cranston *et al.* (1954) performed some of the initial thermal mapping of the airways, and this information was added to by many researchers up to and including McFadden *et al.* (1985) who used a thermal probe to study the temperature and relative humidities *in vivo* at different flow rates.

A number of models describing the heat and vapour transport between the walls of the respiratory tract and the inspired air have been published (Saidel *et al.* 1983, Ferron *et al.* 1985a, Hanna & Scherer 1985, Ingenito *et al.* 1986, Ferron *et al.* 1988a, Tsu *et al.* 1988, Daviskas *et al.* 1990). Tsu *et al.* (1988) performed a control volume analysis on the airways, and present a sophisticated model which can predict airway wall conditions as well as air temperature and relative humidity. Daviskas *et al.* (1990) present a model well suited for integration with a deposition model. Their model is based on an analytical solution to the heat transport equation in a cylindrical tube. The equations for the bulk temperature and water vapour concentrations are relatively simple, and do not require the computational expense of the other models (Daviskas *et al.* 1990). The temperature and humidity profiles predicted by this model are shown in Figures 2.2 and 2.3.

Eisner *et al.* (1990) and Graham & Eisner (1990) present a model of heat and vapour transport from the airway walls that includes the effects of inhaled aqueous aerosols. However, Eisner *et al.* (1990) and Graham & Eisner (1990) neglect momentum diffusion but include radial thermal and mass diffusion. This is not consistent, since the

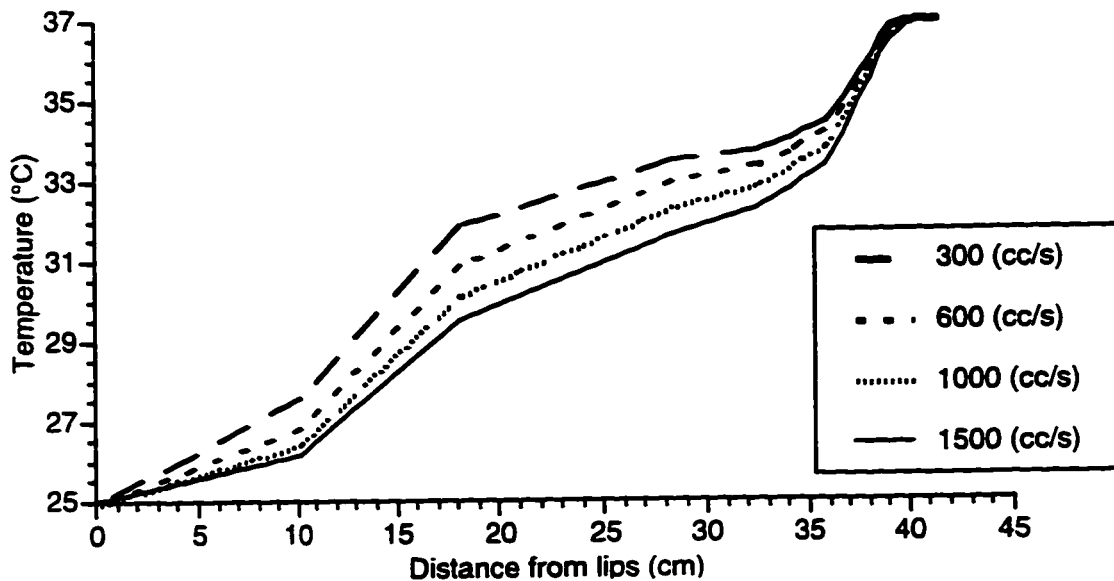


Figure 2.2. The mean end of inhalation temperature of the respiratory tract for inhalation flow rates representative of tidal breathing (300 cm³/s) through single breath inhalation maneuvers (1500 cm³/s) for a Weibel 'A' lung scaled to 3000 cm³. Data from Daviskas *et al.* (1990).

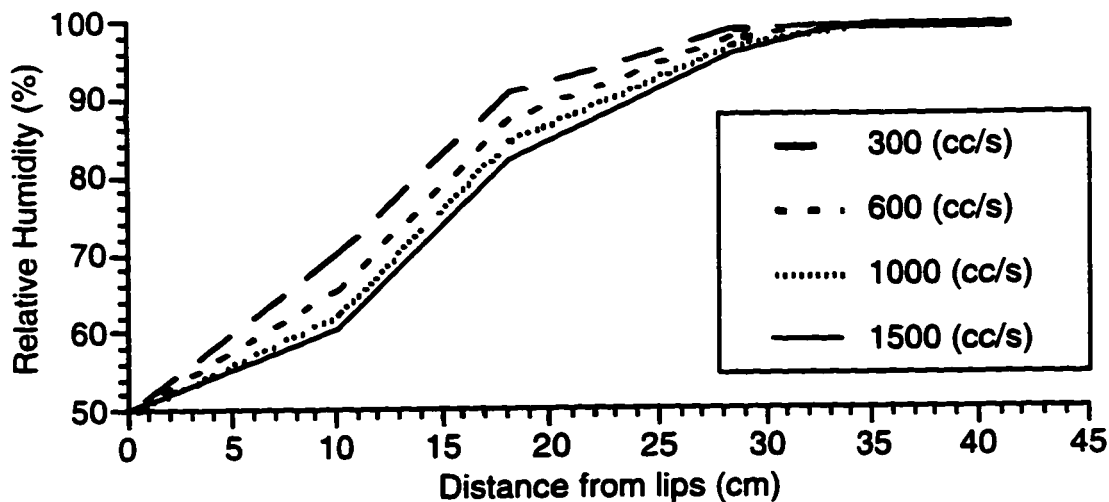


Figure 2.3. The mean end of inhalation relative humidity of the respiratory tract for inhalation flow rates representative of tidal breathing (300 cm³/s) through single breath inhalation maneuvers (1500 cm³/s) for a Weibel 'A' lung scaled to 3000 cm³. Data from Daviskas *et al.* (1990).

Prandtl number (which is the ratio of thermal diffusion to momentum diffusion) and the Schmidt number (which is the ratio of mass diffusion to momentum diffusion) are both of $O(1)$ for typical air/water vapour mixtures encountered in the respiratory tract.

2.3 Respiratory tract fluid dynamics

The ability of a flow to carry particles is partially influenced by the flow regime of the carrier fluid, and it is therefore useful to review the flow regimes in the respiratory tract. General reviews have been presented by Pedley (1977), Swift & Proctor (1977), Chang & Menon (1993), and Shadle (1996) among others.

During normal tidal breathing, flow rate through the extrathoracic regions is approximately $300 \text{ cm}^3/\text{s}$. The Reynolds number for this flow is approximately 1200, lower than the transition value of about 2300 for smooth, straight, circular tubes. However, separation from complex shapes and rough surfaces may produce turbulence, so it is unclear whether the airflow in the airways superior to the glottis during tidal breathing is completely laminar. Forced inhalation maneuvers can cause flow rates more than 10 times those seen in tidal breathing, resulting in Reynolds numbers of over 10,000; so turbulence is expected in these flows.

Dekker (1961) studied the transition between laminar and turbulent flow in plastic casts of the larynx, trachea and main bronchi. By injecting a dye stream into water flowing through these casts, Dekker found that “instabilities” developed at flow rates equivalent to $72 \text{ cm}^3/\text{s}$. At flow rates equivalent to $116 \text{ cm}^3/\text{s}$, Dekker found that the flow in the trachea became turbulent, and that the turbulence was still present in the main bronchi.

Early measurements of the flow characteristics in the extrathoracic airways focused on determining the relation between the pressure drop and flow rate (c.f. Jaeger & Matthys, 1969 and references contained therein). By assuming a power law relation and calculating the power of the relation, they determined the flow regime; for example, if there was a linear relation between the pressure drop and flow rate, then the flow should be laminar (fully developed Poiseuille Flow). Jaeger & Matthys (1969) measured the pressure drop between the mouth and trachea and found that the power of the flow rate vs. pressure relation was approximately 1.55 ± 0.07 (mean \pm standard error), which is between the values for fully developed laminar flow (1.0), and for fully developed turbulent flow (1.75).

One explanation for this result is that the flow is not fully developed. The relation between pressure drop and flow rate is only linear for fully developed laminar flow. The hydrodynamic entrance length, x_h , for a tube of diameter D is approximately

$$\frac{x_h}{D} \approx 0.05 \text{Re}_D \quad (2.8)$$

where Re_D is the Reynolds number based on the diameter of the tube. For flows typically seen in the extrathoracic region, the entrance length is on the order of 50 diameters, so laminar flow in the extrathoracic region would not exhibit a linear flow rate vs. pressure relation. The power of the relation between the flow rate and pressure drop may also be the result of secondary flows, or the onset of turbulence. These flow structures remove energy from the flows, and result in a greater power for the relation between flow rate and pressure drop.

From these results, we can conclude that turbulence is likely present in the flow inferior to (below) the larynx during normal tidal breathing. Superior to (above) the

larynx, the flow regime is not clear, but flows more complex than simple Poiseuille flow are expected.

In contrast with the extrathoracic region, the fluid mechanics of the lungs have been more extensively studied. Pedley (1977) reviews the research available at that time and concludes that the flow in the trachea and first few generations of the lungs can be expected to be turbulent. The depth to which the turbulence persists is unclear, but it is expected to decay quickly, as the Reynolds number drops to a few hundred after approximately 5 generations.

A rough estimate of how many generations through which the turbulence might persist can be found by considering the characteristics of the turbulence. As we are following a bolus of aerosol through the respiratory tract, the correct timescale for estimating the decay time is the Lagrangian timescale, T_L . By definition, the dissipation ϵ is equal to the time rate of change of the turbulence kinetic energy, i.e.:

$$\frac{1}{2} \frac{d}{dt} (q^2) = \frac{-q^2}{B_3 T_L} = \frac{3u_s^2}{B_3 T_L} = -\epsilon \quad (2.9)$$

where u_s is a velocity scale for the turbulent fluctuations. Snyder & Lumley (1971)

found $B_3 \cong 5.0$, so using Equation (2.9) and the viscous limit definition of ϵ , we can write:

$$T_L = 0.3 \frac{\lambda^2}{\nu} \quad (2.10)$$

where λ is a correlation length of the turbulence. If we now assume that production P is approximately equal to the dissipation, we can write:

$$P \cong u_s^2 \frac{U_s}{\delta} = \epsilon \cong \frac{u_s^3}{l} = \frac{\nu u_s^2}{\lambda^2} \quad (2.11)$$

where U , is the mean flow velocity, and δ is the boundary layer thickness. Solving Equation (2.11) for λ^2 and subbing into Equation (2.10) with the boundary layer thickness equal to the radius of the airway, we get:

$$T_L = \frac{0.3 \left(\frac{vd}{2U} \right)}{\nu} = 0.15 \frac{d}{U} \quad (2.12)$$

If decay takes five timescales, and the residence time t for a turbulent eddy in a generation is $t = L/U$, then the decay time can be written:

$$decay \cdot time = 0.75 \frac{d}{L} t \quad (2.13)$$

where d/L is the ratio of the diameter to the length of the generation, often on the order of 0.2 for the first few generations of a Weibel 'A' lung. Equation (2.13) shows us that the decay time for turbulence in a generation of the lung is a fraction of the residence time of the eddy in that generation. Therefore, we can expect that very little turbulence to be convected beyond the lung generation in which it is produced.

The depth to which turbulent flow can be expected in the lungs is therefore a question of to which depth the turbulence can be produced. In branching networks of tubes, turbulence can be produced at Reynolds numbers as low as 400 (Wilson, 1997). Depending on the inhalation flow rate, this level is reached in the first few generations of the lungs. Pedley (1977) suggests that turbulence is present in the flow in the 5th or 6th generation, which appears reasonable considering the turbulence scales.

Flow through central airway bifurcations has been extensively studied both experimentally (Schroter & Sudlow 1969, Olson *et al.* 1970, Olson 1972, Olson *et al.* 1973, Chang & Masry 1982, Isabey & Chang 1982) and computationally (Hofmann &

Balàshàzy 1991, Balàshàzy & Hofmann 1993, Ferron & Eisner 1996). All authors show strong secondary flows, and asymmetric velocity profiles in the daughter tubes. The strength of the flows is found to be strongly dependent on the geometry of the bifurcation and the flow rate. The geometry usually used in these studies corresponds to the first few generations of the lung, yet rarely do the studies consider the effect of a turbulent inlet profile, or the effect of secondary flows from upstream bifurcations.

Acinar fluid mechanics are more difficult to study owing to the poorly characterized geometry of these structures, and because they change size and shape with lung inflation (Haefeli-Bleuer & Weibel, 1988) and straight rigid tubes are often assumed. Based on the Weibel 'A' model, the Reynolds number of the flow in the acini is of $O(1)$, and creeping flow (i.e. no inertial forces and strong viscous forces) can be expected. Recently, Tsuda *et al.* (1996) studied the fluid mechanics and aerosol deposition in a rhythmically expanding acinus using both numerical and experimental techniques. They found that despite the low Reynolds number, the flow is not reversible, and this may contribute to the observed dispersion of inhaled aerosol boluses (c.f. Heyder *et al.* 1988b).

Breathing is inherently an unsteady and transient activity. Unsteady effects on the flow in the respiratory tract were reviewed by Pedley (1977) and argued to be negligible for tidal breathing. In addition, Finlay *et al.* (1996a) conclude that transient effects may only be important near the start or end of exhalation. Here we accept these arguments, and assume that transient and unsteady effects are not important factors affecting particle deposition during tidal breathing.

2.4 Particle deposition mechanisms

2.4.1 Particle deposition in bifurcating systems of cylindrical tubes

In our deposition model, the lungs are modeled as a series of bifurcating cylindrical tubes. The probability of a particle depositing in a tube is dependent on the dimensions of the tube and the flow velocity of the carrier gas. In general, larger particles are deposited by inertial impaction and gravitational sedimentation, while smaller particles tend to be deposited by diffusion. In a dynamical deposition model, equations are written for each of the three deposition mechanisms, and the probabilities are then combined to give a deposition probability for a given particle in a given generation of the lung model. Particles may also deposit by interception and electrostatic precipitation. No distinction is made here between interception and impaction, and it has been argued (Lippmann, 1977) that electrostatic precipitation is not an important deposition mechanism for aqueous therapeutic aerosols. For the deposition of therapeutic aerosols in the human respiratory tract, the most important deposition mechanisms are impaction, which dominates in the extrathoracic region and in the first few bronchial airways, and sedimentation, which is the most important mechanism deeper in the lung.

2.4.1.1 Inertial Impaction

The path followed by air as it is inhaled through the mouth and branching airways of the lungs has many bends. Each time the air changes direction, particles entrained in the air tend to maintain their pre-established trajectories, and may impact on an airway wall. The probability of a particle depositing at a bend in the flow is a function of the

stopping distance for the particle, S , and a characteristic dimension of the flow, D . The ratio of these quantities is the Stokes number, Stk :

$$Stk = \frac{S}{D} = \frac{\rho d_{ae}^2 U}{18\mu D} \quad (2.14)$$

where ρ = particle density;
 d_{ae} = particle aerodynamic diameter;
 U = characteristic velocity of the flow;
 μ = dynamic viscosity of the carrier gas;
 D = a characteristic dimension of the flow.

Figure 2.4 shows how the Stokes number varies in a Weibel 'A' lung geometry scaled to 3000 cm³ for particles with diameters of 2.5, 5.0, and 10.0 μ m, at flow rates of 300 cm³/s and 500 cm³/s. It can be seen that the Stokes number is much higher in the bronchial airways (generations 1 to 16) than in the alveolar regions (generations 17-23), so we might expect that inertial impaction is most important in the bronchial airways. This conclusion is supported by *in vivo* deposition studies (e.g. Lippmann, 1977) where researchers found that tracheobronchial deposition with a wide range of particle diameters and flow rates could be described by a single function of the "impaction parameter", $d^2 Q$, where Q is the inhalation flow rate. It follows from Equation 2.14 that the impaction parameter is directly proportional to the Stokes number.

Treatment of the deposition of particles by impaction in deposition models is not straightforward. Research in this area has been done with casts of the airways (e.g. Schlesinger *et al.* 1977, Chan & Lippmann 1980, Gurman *et al.* 1984), models of bifurcations (e.g. Johnston *et al.* 1977, Kim *et al.* 1994), and by theoretical analysis of the

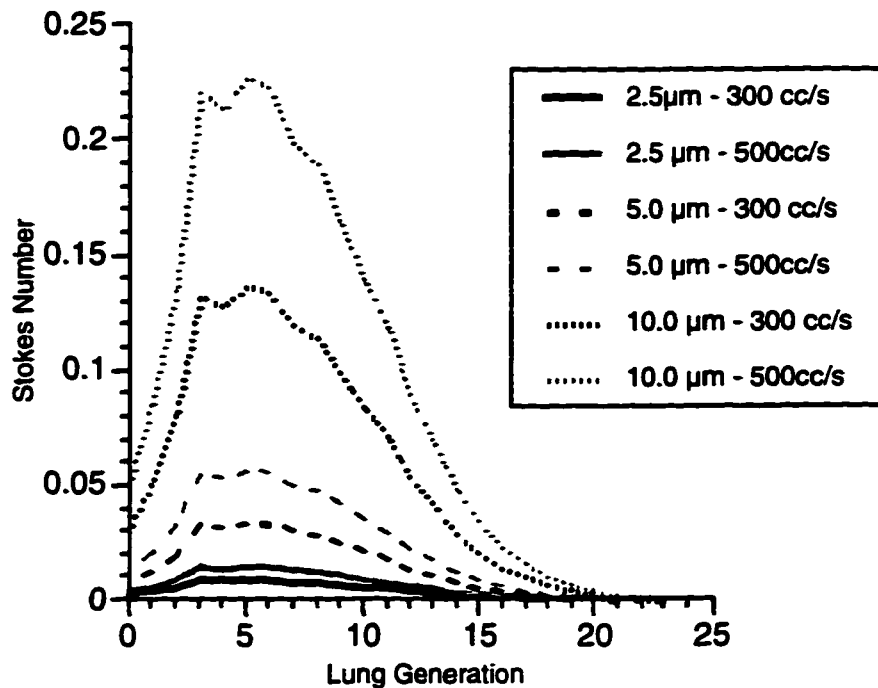


Figure 2.4. Plot of Stokes number (Equation 2.14) vs. lung generation for the scaled Weibel 'A' model lung for three particle sizes and two flow rates.

geometry and flow conditions (e.g. Gawronski & Szewczyk 1986, Cai & Yu 1988, Balàshàzy *et al.* 1991).

Schlesinger *et al.* (1977) present detailed results of the deposition of 2.5 - 8.1 μm particles in a six generation cast of the tracheobronchial airways including a trachea. The deposition probabilities they obtained in generations 1 and 2 were lower than those reported by Schlesinger & Lippmann (1972) who performed similar tests in a three generation cast without a trachea, suggesting that flow artifacts generated in the trachea decrease the deposition in the first two generations. Data on another cast with a trachea was collected by Chan & Lippmann (1980). They combined their data with that of Schlesinger *et al.* (1977) and obtained the following empirical equation to describe the

deposition due to impaction in any bifurcation based on the Stokes number of the parent airway (D = parent airway diameter, and U = parent airway air velocity):

$$\eta_{TB} = 1.606Stk + 0.0023 \quad (2.15)$$

Gurman *et al.* (1984) studied the deposition of 3 and 8 μm particles in casts of the bronchial airways with steady and cyclic flow and found that deposition with cyclic flow was significantly greater than with steady flow. However, Gurman *et al.* use a respiration frequency of approximately 40 breaths per minute, which is much higher than is seen in normal human breathing (ICRP, 1994). Thus, although their results may show that unsteady effects can affect the deposition of aerosol particles in airway bifurcations, the artificially high respiration frequency makes their results for cyclic flow of limited applicability for the inhalation of therapeutic aerosols during tidal breathing or forced inhalation maneuvers like those seen with patients using MDIs and DPIs. An equation based on an empirical fit to the data of Gurman *et al.* (1984) is used in the deposition model of the ICRP (1994).

Johnston *et al.* (1977) studied deposition in simple bends and bifurcating tubes. Experimentally, they found that both Stk and branching angle are important parameters characterizing deposition. Their results indicate that there is negligible deposition for $Stk < 0.1$, which is contrary to more recent experimental data in airway casts and from theoretical calculations, so their data is of limited use for deposition models.

Kim & Iglesias (1989), Kim *et al.* (1989), and Kim *et al.* (1994) studied experimental aerosol deposition in models of bifurcating airways. They found that the deposition probability depended mainly on the Stokes number in the parent tube, and slightly on the diameter ratio of the daughter and parent tubes. The bifurcation angle was

varied between 30 and 45 degrees, but did not have a significant effect on the results. Likewise, both symmetrical and asymmetrical bifurcations gave similar results. They present two equations to predict the deposition probability in bifurcations:

$$\eta_{TB} = 3.7417Stk^{1.16} - 0.0394 \quad (2.16)$$

for a daughter to parent diameter ratio greater than 0.8, and:

$$\eta_{TB} = 1.5714Stk^{0.62} - 0.1299 \quad (2.17)$$

for a daughter to parent diameter ratio of 0.64, where both equations are valid for $Stk \cdot 0.02$.

As an alternative to experimental measurements, an equation for the deposition of particles by impaction can be obtained by considering the forces acting on particles flowing through bent tubes. Findeisen (1934) and Landahl (1950) present crude equations based on the impaction of aerosols in 90° bends. More recently, Gawronski & Szewczyk (1986) used the concept of stopping distance to derive equations for the inertial deposition of particles in bent tubes which show good agreement with experimental deposition data from lung casts and bifurcation models:

$$\eta = \frac{16}{3\pi} \phi \cdot Stk \left(2 - \sqrt{\frac{4}{3} \phi \cdot Stk} \right) \quad (2.18)$$

where

$$\phi = 2 \left(\frac{d}{d_o} \right)^2 \sin \alpha ;$$

α = bifurcation angle;

d = diameter of daughter branch;

d_o = diameter of parent branch;

Stk = Stokes number of the daughter branch.

Cai & Yu (1988) found errors in this work, and rederived the equations while extending the theory to include the deposition of fibers. Their equations are a linear

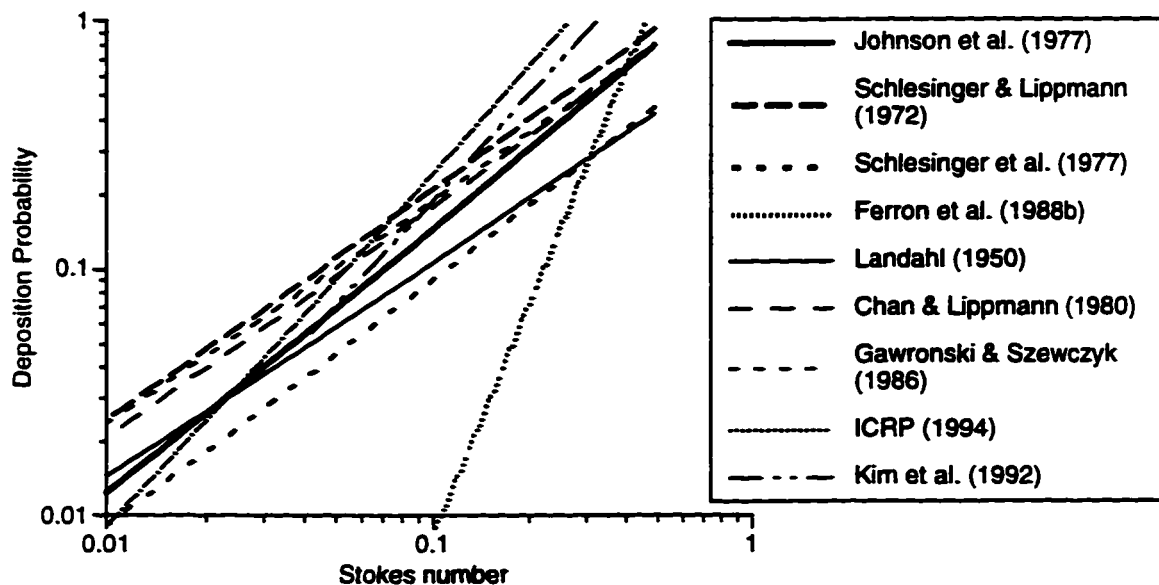


Figure 2.5. Common equations used to predict deposition due to impaction in deposition models.

function of the Stokes number of the parent tube, and include corrections for branching angle and parent/daughter diameter ratio. Balàshàzy *et al.* (1990) consider the forces acting on particles in bent tubes and present equations for deposition due to the combined action of inertial impaction and gravitational sedimentation in bent tubes and bifurcations with varying flow profiles. Their equations also predict the local deposition sites of the aerosol within the bifurcation, which agree well with the local deposition sites seen in the experimental results of Kim *et al.* (1989). The equations presented by both Cai & Yu (1988) and Balàshàzy *et al.* (1990) compare well with the experimental data of Schlesinger *et al.* (1977) and Chan & Lippmann (1980) for the deposition of aerosols in airway casts.

Care must be taken when comparing the various equations used to estimate inertial impaction in bifurcating airways due to the different definitions of the Stokes number. Figure 2.5 plots many of the equations commonly used to predict aerosol

deposition in bifurcations for Stokes numbers for aerosol particles between 1 μm and 10 μm in the respiratory tract. It can be seen in Figure 2.5 that the equations all behave similarly. Particle deposition predictions in the model presented in this thesis use Equation (2.15) from Chan & Lippman (1980) to predict the deposition due to inertial impaction. This equation was chosen because it is based on the deposition seen in multi-generation airway casts, and therefore includes the effects of secondary flows not included in the theoretical equations and the single generation studies with bifurcation models

2.4.1.2 Sedimentation

The theory of aerosol deposition from fully developed laminar flow in horizontal tubes (Walton, 1954, Thomas, 1958, Fuchs, 1964, Pich, 1972) is well developed, and can be described by:

$$\eta_s = \frac{2}{\pi} \left[2\epsilon \sqrt{1 - \epsilon^{2/3}} - \epsilon^{1/3} \sqrt{1 - \epsilon^{2/3}} + \arcsin(\epsilon^{1/3}) \right] \quad (2.19)$$

where

$$\epsilon = \frac{3v_s L}{8rU} \equiv \text{sedimentation parameter};$$

v_s = particle settling velocity;

L = length of tube;

U = average flow velocity;

r = tube radius.

Wang (1975) extended this theory to inclined tubes, and found different expressions for uphill and downhill flows. However, when the magnitude of the projection of the settling velocity of the particles in the direction of the fluid flow is small compared to the maximum velocity of the laminar flow, i.e.:

$$\frac{v_s}{u} \sin \beta \ll 1 \quad (2.20)$$

then the equations for both uphill and downhill flow can both be approximated by Equation (2.19) with the sedimentation parameter defined by:

$$\varepsilon = \frac{3v_s L}{8rU} \cos \beta \quad (2.21)$$

where β is the angle with respect to horizontal. Heyder & Gebhart (1977) experimentally validated Equations (2.19) and (2.21). Additionally, Heyder & Gebhart integrated Equations (2.19) and (2.21) through a network of randomly oriented tubes, and found that the deposition in the network differs by less than 2% from the deposition in a single tube inclined at $\beta=38.25^\circ$ from the horizontal for values of ε less than approximately 0.5, and by less than 10% for values of ε up to 1.0. Values of ε are typically less than 0.5 in the bronchial airways, so Equations (2.19) and (2.21) will give good predictions of the deposition probabilities due to sedimentation in the bronchial airways, but may underpredict the deposition probabilities by as much as 10% in the alveolar airways since values of ε in the range $0.5 \leq \varepsilon \leq 1.0$ often occur in these airways.

As discussed previously, it is likely that the flow in the trachea and the first few generations of the lungs is turbulent, making the applicability of Equation (2.19) in this region suspect. Brockmann (1993) discusses sedimentation from turbulent pipe flow, and shows that for values of ε less than 0.5 (given by Equation 2.21), the deposition probability does not differ significantly from that seen in laminar flows. During tidal breathing, ε is less than 10^{-3} in the first few generations of the lungs for an aerosol with an MMD of 5.0 and GSD of 1.7, so the assumption of laminar flow in those regions will not affect the deposition predictions significantly. Additionally, it has been argued by

many of the researchers studying the impaction of aerosols in the bronchial airways, that the probability of a particle depositing by sedimentation in the first few generations of the bronchial airways is not significant compared to the probability of the particle depositing by impaction. For these reasons, we use Equation (2.19) for predicting deposition due to sedimentation throughout all lung airways

2.4.1.3 Diffusion

Diffusion is an important deposition mechanism for particles smaller than approximately 1 µm. Above that size it is normally negligible, but is included here for completeness, and for improving the deposition estimates of particles in the range of 0.5µm to 1.0 µm.

Gormley & Kennedy (1949) developed an equation for the deposition of spherical particles from Poiseuille flow in tubes as a function of a diffusion parameter h :

$$h = \frac{Dt}{4r^2} \quad (2.22)$$

where:

D = diffusion constant;
t = residence time in tube;
r = radius of tube.

Gormley & Kennedy's derivation was confirmed by Ingram (1975) who added an extra term to the solution to give:

$$\eta_D = 1 - 0.819e^{-14.63h} - 0.0976e^{-89.22h} - 0.0325e^{-228h} - 0.0509e^{-125.9h^{2/3}} \quad (2.23)$$

to improve the predicted values of the deposition coefficient. Gormley & Kennedy give an asymptotic solution to their equation which is less than 1% different from Equation (2.23) for h less than approximately 0.1 (Ingram, 1975):

$$\eta_D = 6.41h^{2/3} - 4.8h - 1.123h^{4/3} \quad (2.24)$$

Cohen *et al.* (1990) measured the deposition of ultrafine particles with diameters between 0.04 μm and 0.2 μm in casts of the tracheobronchial airways and showed that Equation (2.23) underestimates the measured deposition probability, and theorize that this is the result of the equations not accounting for the secondary flows present in bifurcating airways. Yu & Cohen (1994) derive an expression that includes the effects of the secondary flows and predicts measured deposition probabilities for particles between 0.01 μm and 0.4 μm . The differences between the equation of Yu & Cohen (1994) and Equation (2.24) are less than 10^{-3} for particles larger than 0.5 μm . For an aerosol with an MMD of 5.0, and a GSD of 1.7, inhaled at 300 cm^3/s (which is typical for the aerosols considered here), values of the diffusion parameter h are less than 10^{-3} for more than 98% of the aerosol mass. We therefore use Equation (2.24) to estimate the deposition in the airways.

2.4.2 Extrathoracic deposition

As discussed previously, the geometry and fluid flow in the extrathoracic region of the respiratory tract is complex, and developing dynamical equations for predicting deposition probabilities in this region is difficult. For this reason, it is common to use empirical expressions to estimate the filtering efficiency of the mouth and throat. For mouth breathing, the filtering efficiency of the extrathoracic region can be approximated by (Rudolf *et al.* (1990):

$$\eta_{E, Mouth} = 1 - \left(1.10 \times 10^{-4} (d_{ae}^2 Q^{0.6} V_T^{-0.2})^{1.4} + 1 \right)^{-1} \quad (2.25)$$

where $\eta_{E, Mouth}$ = filtering efficiency of the region for mouth breathing;
 d_{ae} = aerodynamic particle diameter;
 Q = inhalation flow rate (cm^3/s);

V_T = tidal volume (cm³).

If a mask is used instead of a mouthpiece to conduct the aerosol from the nebulizer to the patient, then deposition in the nasal passages must be considered as well. For the aerodynamic deposition of aerosol particles in the nose, Rudolf *et al.* (1990) give:

$$\eta_{E,Nose} = 1 - \left((2.05 \times 10^{-4} d_{ae}^2 Q) + 1 \right)^{-1} \quad (2.26)$$

where Q is the flow rate through the nasal passages.

2.5 Respiratory tract deposition models

2.5.1 Calculation of deposition probabilities

In a Lagrangian dynamical respiratory tract deposition model, the respiratory tract is viewed as a series of filters, where each generation of the lung model is a filter. Particles deposit in each generation due to the combined actions of inertial impaction, gravitational sedimentation, and Brownian diffusion. The geometrical model of the airways consists of the mouth, throat (the larynx and pharynx are both considered to be part of the throat), trachea, and the 23 generations of the Weibel 'A' model. To assist with the programming of the model, we use an 'extended Weibel' numbering system in which the nose and mouth are generation 1, the throat is generation 2, the trachea is generation 3, and the Weibel lung generations are labeled generations 4 through 26, with generations 3-19 corresponding to the bronchial region, and generations 20-26 corresponding to the alveolar region.

There are three phases to a normal tidal breathing cycle: inhalation, inspiratory pause, and exhalation. Inhalation is followed by the inspiratory pause, and the rest of the

breathing cycle is exhalation. For tidal breathing, the average breathing cycle is approximately 4 seconds long, with a 1.74 second inhalation, 0.2 second pause, and a 2.06 second exhalation (ICRP, 1994). For tidal volumes smaller than the size of the lung model, only L generations will be ventilated, where $L \approx 26$. The normal tidal volume for an adult Caucasian male is approximately 700 cm^3 , giving $L = 24$.

2.5.1.1 Deposition during inhalation

For combined nose and mouth breathing, the filtering efficiency of the nose is written:

$$\eta_1 = (1 - \psi)\eta_{E,nose} \quad (2.27)$$

where $\eta_{E,nose}$ is given by Equation (2.26), and ψ is the fraction of the aerosol inhaled through the mouth. Since mouth deposition is considered part of pharyngeal deposition, and for nasal breathing the effect of the dead space is negligible, the deposition in generation 1 is given by Equation (2.1) and can be written:

$$DE_1^{in} = \eta_1 \quad (2.28)$$

During pure mouth breathing, all particles are assumed to deposit at the end of the pharynx (i.e. in the larynx). The probability that a particle inhaled through the mouth or nose will deposit in the pharynx is then given by Equation (2.3), i.e.:

$$DE_2^{in} = (1 - \eta_1)\eta_{E,mouth}\phi_2 \quad (2.29)$$

where $\eta_{E,mouth}$ is given by Equation (2.25), and ϕ_2 is the fraction of the tidal volume that passes entirely through the pharynx and is equal to:

$$\phi_2 = 1 - (V_{mouth} + V_{pharynx}) = 1 - \sum_{k=1}^2 V_k \quad (2.30)$$

where V_k is the fraction of the tidal volume occupied by generation k . For an adult male during tidal breathing, $\phi_2 \approx 0.85$.

In the lungs, inertial impaction, gravitational sedimentation, and Brownian diffusion each contribute to the filtering efficiency of each generation. Assuming that each process acts independently, the total filtering efficiency for generation k can be written:

$$\eta_k^{in} = 1 - (1 - \eta_i)(1 - \eta_s)(1 - \eta_D) \quad (2.31)$$

where η_i is given by Equation (2.15), η_s is given by Equation (2.19), η_D is given by Equation (2.24), and the values of the parameters (e.g. tube radius, Stokes number) in Equations (2.15), (2.19), and (2.24) correspond to the values for generation k .

Using Equation (2.31), the fraction of the inhaled aerosol which deposits in generation k can then be written:

$$DE_k^{in} = \left(\prod_{i=0}^{k-1} (1 - \eta_i^{in}) \right) \cdot \phi_k \eta_k^{in} = f_k \phi_k \eta_k^{in} \quad (2.32)$$

where f_k is the fraction of the inhaled aerosol that penetrates to generation k , and ϕ_k is the fraction of the tidal volume that passes entirely through generation k , and is given by:

$$\phi_k = 1 - \sum_{i=1}^k V_i \quad (2.33)$$

2.5.1.2 Deposition during the inspiratory pause

The probability that a particle will deposit in generation k during the inspiratory pause is equal to the fraction of inhaled particles which are in the generation at the end of inspiration, multiplied by the probability that the particle will deposit during the pause.

During the inspiratory pause, there is no flow through the airways, and therefore no deposition due to inertial impaction. Equation (2.31) becomes:

$$\eta_k^{hold} = 1 - (1 - \eta_s)(1 - \eta_D) \quad (2.34)$$

and the probability that an inhaled particle with deposit in generation k during the inspiratory pause is:

$$DE_k^{hold} = f_k (1 - \eta_k^{in}) \eta_k^{hold} V_k = f_{k+1} \eta_k^{hold} V_k \quad (2.35)$$

2.5.1.3 Deposition during exhalation

Particles that are available for deposition during exhalation must not have deposited during inhalation or the inspiratory pause. Therefore, the deposition during exhalation can be written:

$$DE_k^{ex} = f_{k+2} V_{k+1} (1 - \eta_{k+1}^{hold}) \eta_k^{ex} + \sum_{i=k+2}^L f_{i+1} V_i (1 - \eta_i^{hold}) \prod_{j=k+1}^{i-1} (1 - \eta_j^{ex}) \eta_{ik}^{ex} \quad (2.36)$$

where η_k^{ex} is given by the RHS of Equation (2.31), the same equation as was used to calculate η_k^{in} , and L is the last ventilated generation. It is assumed that there is no deposition in the extrathoracic region during exhalation.

2.5.1.4 Total and Regional deposition

The total deposition is calculated from:

$$DE_E = DE_1^{in} + DE_1^{hold} + DE_2^{in} + DE_2^{hold} \quad (2.37)$$

The total deposition in a lung generation can be calculated by summing the deposition during inhalation, the inspiratory pause, and exhalation, i.e.:

$$DE_k = DE_k^{in} + DE_k^{hold} + DE_k^{ex} \quad (2.38)$$

Tracheo-bronchial deposition is then calculated from:

$$DE_{TB} = \sum_{k=3}^{19} DE_k \quad (2.39)$$

and alveolar deposition is calculated from:

$$DE_{Alv} = \sum_{k=19}^L DE_k \quad (2.40)$$

The total deposition in the respiratory tract is simply the sum of the regional depositions given by Equations (2.37), (2.39), and (2.40).

2.5.1.5 Polydisperse aerosols

Polydisperse aerosols are easily treated by discretizing the aerosol distribution into evenly spaced diameter subdivisions, or ranges. Many of the deposition equations reviewed in Section 2.4 depend on the square of the particle diameter, indicating that relatively small changes in particle size can have a large change in deposition probability. For this reason, diameter subdivisions less than or equal to 1 μm are used.

Once the distribution has been discretized, the diameter of each particle class is allowed to fluctuate independently of each other. Hence, there is no restriction on the shape of the particle size distribution.

2.5.2 Hygroscopic effects

Most therapeutic aerosols contain hygroscopic substances, usually in the form of organic or inorganic hydrophilic salts. This complicates the calculation of deposition probabilities, since the aerosol particles may grow or shrink as they travel through the respiratory tract. This can dramatically affect their fate since the diameter of a particle is an important parameter in the estimating its deposition probability (c.f. Morrow, 1986,

and Hiller, 1989 for reviews on this subject). Gebhart *et al.* (1990) studied the deposition of initially solid NaCl particles in the respiratory tract, and found that the measured deposition in the respiratory tract is similar to that of non-hygroscopic particles approximately 4 times the initial size of the NaCl particles.

Various authors have modified models for predicting the deposition of non-hygroscopic aerosols to account for the size changes common with hygroscopic aerosols (Persons *et al.* 1987, Ferron *et al.* 1988b, Stapleton *et al.* 1994, Finlay & Stapleton, 1995). These models calculate the growth and shrinkage of the droplets in response to their environment. Modifications are made to basic deposition equations so that the particle size used in the deposition equation for a specific generation of the airway is the average size of the particle in that generation.

Many hygroscopic models only calculate the size changes of hygroscopic particles in response to the environment of the respiratory tract and neglect the effect of the particles on the environment. These are referred to as one-way coupled models. The model described here also considers the effects of particle size changes on the environment of the respiratory tract, and is called a two-way coupled model. As will be shown later, two-way coupling is an important consideration for calculating the correct deposition of therapeutic aerosols produced by nebulizers.

2.5.2.1 Governing Equations

The equations governing the transfer of heat and water vapour between aerosol droplets and the continuous phase are discussed in detail by Fuchs (1959), Mason (1971), Heidenreich (1994) and are used in the context of lung deposition modeling by Ferron

(1977), Persons *et al.* (1987), and Ferron & Soderholm (1990), among others, and are reviewed here for completeness. Assuming a polydisperse aerosol discretized into N evenly spaced diameter ranges with n_i particles per unit volume in the i th size range with an average diameter d_i , the equation governing the diameter of the i th particle size can be written as:

$$\frac{dm_i}{dt} = 2\pi d_i D_w C_w (c_\infty - c_{o,i}) \quad i = 1, \dots, N \quad (2.41)$$

where

- $m_i = \frac{\rho_i \pi d_i^3}{6}$ is the mass of a droplet of the i th size range with diameter d_i ;
- D_w = diffusion coefficient of water vapour in air;
- C_w = Knudsen correction (c.f. Ferron, 1977);
- c_∞ = water vapour concentration in the bulk continuous phase;
- $c_{o,i}$ = water vapour concentration at the surface of the droplet.

The density of the i th droplet is calculated from its initial solute and water content and its current size (c.f. Ferron, 1977), with mass changes due solely to the evaporation or condensation of water. The water vapour pressure reduction at the surface of the droplet due to dissolved NaCl is calculated with the empirical equation of Cintokai (1971) which includes non-linear changes in the dissociation constant with concentration. The vapour pressure reduction due to other dissolved components is calculated assuming dilute solutions (i.e. using Raoult's Law) and a constant van't Hoff factor. For many therapeutic aerosols based on normal saline, the contribution to the total vapour pressure reduction at the particle surface from components other than NaCl is negligible.

The equation governing the temperature of the i th particle size is:

$$m_i C_{p,i} \frac{dT_i}{dt} = Q_{c,i} + Q_{m,i} \quad i = 1, \dots, N \quad (2.42)$$

where C_{p_w} is the specific heat of water (and is assumed to be independent of temperature). Here, Q_m is the latent heat transfer, and Q_c is the conductive heat transfer. These are given by:

$$Q_m = \frac{dm_i}{dt} L \quad (2.43)$$

$$Q_c = 2\pi d_i \kappa_a C_T (T_\infty - T_i) \quad (2.44)$$

where

- L = the latent heat of condensation;
- κ_a = the thermal conductivity of air ;
- T_∞ = temperature of the continuous phase;
- T_i = temperature at the surface of the droplet.

The latent heat of condensation is negative and is assumed to be independent of temperature, while the thermal conductivity of air is assumed to vary linearly with temperature (Incropera and DeWitt, 1990). The Knudsen correction C_T in Equation (2.44) and C_u in Equation (2.41) account for noncontinuum effects and are discussed in detail elsewhere (e.g. Ferron & Soderholm, 1990), and their importance is discussed by Heidenreich & Büttner (1995).

The heat and mass transport from the droplets, given by Equations (2.41) - (2.44), is driven by the difference in temperature and water vapour concentration between the continuous phase, and the surface of the droplet. Heat and mass transferred to the continuous phase from the discrete phase changes the temperature and relative humidity of the continuous phase, which affects the heat and mass transfer rate. This coupling of the heat and mass transfer rates between the discrete and continuous phases requires that the water vapour concentration, c_w , and temperature, T , are calculated simultaneously with the particle size as the bolus moves through the respiratory tract.

The equation governing the water vapour concentration as the bolus carrying the droplets moves through the respiratory tract can be written as:

$$\frac{dc_{\infty}}{dt} = \dot{m}'_{wall} - \sum_{i=1}^N n_i \frac{dm_i}{dt} \quad (2.45)$$

The second term on the right-hand side of Equation (2.45) accounts for the mass transfer occurring at the droplet surfaces, and is obtained from a simple mass balance. The first term on the right-hand side of Equation (2.45), \dot{m}'_{wall} , accounts for the mass transfer from the airway walls to the continuous phase. This term can be evaluated using a mass transfer coefficient, g'_k , (Kays & Crawford, 1980) for each generation k in the lung, so that the mass transfer rate in the k th generation is:

$$\dot{m}'_{wall} = g'_k (c_{wall} - c_{\infty}) \quad (2.46)$$

The value of the mass transfer coefficient, g'_k , can be calculated from the known temperature and humidity profiles of the respiratory tract when no droplets are present in the inhaled air (Ferron *et al.*, 1988a, Daviskas *et al.*, 1990) from:

$$g'_k = \frac{(\Delta c_{\infty}^0)_k}{\Delta t_k (\bar{c}_{wall} - \bar{c}_{\infty}^0)_k} \quad (2.47)$$

where $(\Delta c_{\infty}^0)_k$ is the change in water vapour concentration between the beginning and end of the k th generation when no droplets are present, and $(\bar{c}_{wall} - \bar{c}_{\infty}^0)$ is the difference between the average water vapour concentration of the continuous phase in the k th generation and the average value at the airway walls when no droplets are present. The value of Δt_k in Equation (2.47) is the amount of time a bolus of air spends in the k th generation when traveling at the bulk flow velocity in that generation. Within each

generation, the mass transfer coefficient g'_k is assumed to be independent of mass transfer rate, implying an assumption of relatively low mass transfer rate (Kays & Crawford, 1980).

Similarly, the equation governing the temperature of the continuous phase as the bolus moves through the respiratory tract can be written:

$$(c_{\infty} C_{p_{\infty}} - \rho_{air} C_{p_a}) \frac{dT_{\infty}}{dt} = \dot{q}'_{wall} - \sum_{i=1}^N n_i Q_c, \quad (2.48)$$

where C_{p_a} is the specific heat of air (and is assumed to be independent of temperature), and ρ_{air} is the density of air. As in Equation (2.45), the second term on the right-hand side of Equation (2.48) accounts for the heat transfer to the continuous phase due to conduction from the discrete phase, and the first term on the right-hand side of Equation (2.48), \dot{q}'_{wall} , accounts for the heat transfer from the airway walls, and can be written:

$$\dot{q}'_{wall} = h'_k (T_{wall} - T_{\infty}) \quad (2.49)$$

where the heat transfer coefficient h'_k in the k th generation is evaluated in a manner similar to the mass transfer coefficient g'_k given in Equation (2.47) using the known temperature profiles in the lung when no droplets are present (Daviskas *et al.* 1990), and can be written:

$$h'_k = \frac{[(\bar{\rho}_{air}^0)_k C_{p_a} + (\bar{c}_{\infty}^0)_k C_{p_{\infty}}] (\Delta T_{\infty}^0)_k}{\Delta t_k (\bar{T}_{wall} - \bar{T}_{\infty}^0)_k} \quad (2.50)$$

where

$(\bar{\rho}_{air}^0)_k$ = average density of air in the k th generation;

$(\bar{c}_{\infty}^0)_k$ = average water vapour concentration of the continuous phase in the k th generation;

$(\Delta T_{\infty}^0)_k$ = temperature change in the continuous phase between the proximal

and distal ends of the k th generation;
 $(\bar{T}_{wall} - \bar{T}_{\infty}^0)_k$ = difference between the average wall temperature and temperature of the continuous phase in the k th generation.

All of the quantities in Equation (2.50) are evaluated when no droplets are present in the inhaled air.

It is common practice in Lagrangian dynamical models to neglect momentum boundary layers and assume a plug flow velocity profile within the airways. Since the Prandtl and Schmidt numbers are both of $O(1)$ in the continuous phase, it is then consistent to also neglect thermal and mass diffusion boundary layers. With this assumption, the aerosol bolus will remain as a continuous plug as it travels through the respiratory tract, and the heat and mass transferred per unit volume to the continuous phase from the airway walls in each lung generation are then the average amounts transferred per unit volume of flow through the generation.

Equations (2.41) - (2.50) represent a set of $2N+2$ coupled, nonlinear, ordinary differential equations that govern $2N+2$ unknowns associated with the diameters and temperatures of N droplet sizes, and the temperature and water vapour concentration of the continuous phase. These equations must be solved numerically. In addition, the number of droplets in the bolus is an important parameter in determining the water vapour concentration and temperature of the continuous phase from Equations (2.45) and (2.48), requiring Equations (2.41) - (2.50) to be solved simultaneously with the deposition equations.

2.5.2.2 Solution methodology

At the beginning of each generation, the coefficients g'_k and h'_k are calculated for the generation. An aerosol bolus is then tracked through the generation and their sizes calculated by solving Equations. (2.41) - (2.50) using the SFODE routine of the Naval Surface Warfare Center for numerical analysis library (Morris, 1993, Finlay & Stapleton, 1995). An average size for each particle size range is then calculated for the generation, and is used to calculate deposition probabilities for each particle size range using the equations described in Section 2.5.1. The number of particles per unit volume of the bolus is reduced by multiplication of the number densities with the calculated deposition probabilities so that particles deposited in this generation do not contribute to the heat and mass transport between the discrete and continuous phases in subsequent generations. This process is repeated for all generations of the lungs ventilated during the breathing.

The SFODE routine uses a variable order backward differentiation (BDF) method with adaptive, variable size time step. The BDF method is an implicit method, and therefore requires the solution of a $(2N + 2) \times (2N + 2)$ set of linear equations for each time step. For a typical therapeutic aerosol with an $MMD = 5.0$, and a $GSD = 1.7$, $N = 20$ is common, and this causes computation times to be approximately 100 times greater than those seen for non-hygroscopic aerosols.

2.5.2.3 One-way Coupling

In one way coupling, heat and mass transfer between the discrete and continuous phases does not affect the temperature or water vapour concentration of the continuous phase. This assumption is valid for aerosols with low number concentrations where the

water vapour and heat exchanged between the phases is negligible compared to the amount contained in the continuous phase. This assumption uncouples the $2N$ equations associated with Equation (2.41) and Equation (2.42), and the equations for each particle size can be solved independently of each other.

The model described in this thesis has the option of using one-way coupling to calculate the growth of hygroscopic particles. If this option is selected, the model is similar to that of Ferron *et al.* (1988b), although the temperature and water vapour concentration of the continuous phase is given by the model of Daviskas *et al.* (1990), and the vapour pressure reduction at the surface of the droplets due to dissolved NaCl is given by the empirical equation of Cintokai (1971). (Additionally, there are differences in the deposition equations for the extrathoracic region and deposition due to impaction in the airways.)

The main advantage of one-way coupling is that it greatly reduces the computational time required to calculate the size of the aerosol particles as they move through the respiratory tract. For the aerosol considered in Section 2.5.2.2 where $N = 20$, computation times are only approximately 5 times greater than those seen for non-hygroscopic aerosols, or 1/20 of those seen using two-way coupling.

Finlay & Stapleton (1995) show that for the aerosols typically produced by nebulizers, a one-way coupled model underpredicts the dosage delivered to the extrathoracic region by as much as 137%, with total and bronchial dosages in error by as much as 10%, and alveolar dosages in error by as much as 20% (see Section 3 of this thesis for a description of the methodology to calculate the dosage delivered to the regions of the lungs). Consequently, two-way coupling is preferred unless it can be

demonstrated that the number densities of the aerosol are low enough that one-way coupling can be used without incurring significant error.

2.5.2.4 Hygroscopic vs. Nonhygroscopic calculations

While it is accepted that most therapeutic aerosols are hygroscopic, it is not clear whether hygroscopic effects are an important consideration when estimating their deposition in the respiratory tract. Clark (1995) found that the relative distribution between the upper and lower airways determined *in vivo* with planar gamma scintigraphy is adequately modeled when hygroscopic effects are neglected, suggesting that the added complexity and cost of including hygroscopic effects in deposition models is unnecessary.

A possible explanation for Clark's observation is that the heat and mass transferred between the discrete and continuous phases may reduce the importance of hygroscopic size changes (Finlay *et al.* 1997c). Finlay *et al.* calculate the dosage delivered to the extrathoracic, bronchial, and alveolar regions of the respiratory tract for a variety of common jet nebulizers using three different hygroscopic models (i.e. non-hygroscopic, one-way and two-way coupled). They found that when the ambient relative humidity (RH) of the testing laboratory was 90%, hygroscopic effects are unimportant, since all three methods of treating hygroscopic effects gave similar results. At an ambient relative humidity of 50%, they found that significant errors in the estimates of the delivered dosages are seen for nebulizers that output low number density aerosols when assuming stable particles, or one-way coupling. At an ambient relative humidity of

15%, they found that two-way coupling was an important consideration for non-vented nebulizers.

The above data suggests that a non-hygroscopic deposition model may give adequate estimates of the deposition from some nebulizers, but because the coupled heat and mass transfer effects depend on many factors, including ambient relative humidity, properties of the inhaled aerosol, and the breathing pattern of the individual, it is not possible to make a general statement that hygroscopic effects are not important for nebulized aerosols (Finlay & Stapleton, 1996a, Finlay *et al.* 1997c). Therefore, caution must be exercised if a coupled hygroscopic model is not used when modeling the deposition of nebulized aerosols.

2.5.3 Intersubject variability

The Lagrangian dynamical deposition model described in this thesis uses an “average” lung geometry, and therefore predicts the deposition for an “average” person, as do all other deposition models using idealized lung geometries (e.g. Martonen *et al.* 1982, Persons *et al.* 1987, Xu & Yu 1985, Ferron *et al.* 1988b, among others). However, experimental data of aerosol deposition in the human respiratory tract shows that there are significant differences in deposition probabilities between one person and another (cf. Goldberg & Lourenço 1973, Stuart 1973, Lippmann 1977, Lippmann *et al.* 1980, Stahlhofen *et al.* 1989, Morrow & Yu 1993, and references contained therein) and the resulting variation in deposition probabilities is not accounted for in most deposition models. The main causes of intersubject variability in total lung deposition are unclear. Morrow & Yu (1993) argued that the main cause of the intersubject variability is

differences in lung morphology between individuals, and to a lesser extent, differences in breathing pattern. Heyder *et al.* (1982) and Heyder *et al.* (1988a) came to similar conclusions by comparing the deposition in subjects who were breathing spontaneously and with a controlled breathing pattern. However, Bennett (1988) reviewed the available literature and concluded that breathing pattern variability in humans is greater than variability in peripheral airspace size, and therefore breathing pattern played a more important role in the observed intersubject variability.

Because one of the main causes of intersubject variability is differences in lung morphology between individuals, Yu and Diu (1982a) consider using different lung geometries with a single deposition model as a possible way of estimating intersubject variability. They showed reasonable agreement with experimental data, and found that calculations performed with a Weibel 'A' lung geometry approximate the population average. However, this method has the disadvantage of requiring several times the computing time of a single lung geometry. Run times of tens of hours are seen on high-performance workstations (IBM RS6000 Model 59H) when dosage estimates are obtained for a nebulizer using the model described in this thesis with two-way coupled heat and mass transfer between the droplets and the surrounding continuous in a single lung geometry. Therefore, using multiple lung geometries is not a practical solution for estimating the intersubject variability in a reasonable number of delivery devices.

Yu and Diu (1982b) present a probabilistic model for predicting intersubject variability in regional deposition probabilities that agrees well with the experimental data of Stahlhofen (1981). However, this method requires a numerical integration of the deposition model over different lung volumes, which also requires multiple runs of the

deposition model, and is again currently impractical for use with two-way coupled, hygroscopic deposition models.

The empirical stable particle deposition model of Rudolf *et al.* (1990) includes equations for the 95% confidence intervals for extrathoracic, fast- and slow-cleared thoracic deposition. The equations are based on data from different labs and reflect different breathing patterns (i.e. controlled vs. spontaneous), and measurement techniques. It has been shown (Heyder *et al.*, 1978) that different measurement techniques can report different deposition in the same populations, so the intersubject variability reflected in the equations for the confidence intervals may over-estimate the true value. However, it may still be possible to estimate the variability in regional dosages from the spread seen in experimental results. Gebhart *et al.* (1990) summarizes the experimental data on the total deposition of hygroscopic aerosols, but to the authors' knowledge, there is no data on the regional deposition of hygroscopic aerosols. There are, however, a significant number of studies on the regional deposition of stable particles, and it may be possible to adapt these results to a hygroscopic deposition model to estimate intersubject variability.

2.5.3.1 Calculation of intersubject variability

To estimate the intersubject variability in the calculations, experimental data on the deposition of non-hygroscopic monodisperse aerosols in the respiratory tract is considered (Lippmann & Albert 1969, Foord *et al.* 1978, Chan & Lippmann 1980, Lourenço *et al.* 1971, Emmett *et al.* 1982). By convention, we assume that fast-clearance corresponds to tracheo-bronchial deposition, and slow-clearance corresponds to

alveolar, even though there is some uncertainty in making these assumptions (c.f. section 2.6 of this thesis). Stahlhofen *et al.* (1989) summarize the experimental data for the regional deposition of non-hygroscopic aerosols, and note that some of the differences in the deposition measured at different labs are caused by different controls on the breathing parameters: studies where both the tidal volume and flow rate were controlled showed less intersubject variability than those where the patient breathed spontaneously (or only the number of breaths per minute was controlled). For our purposes, we are interested in predicting the variability in the dosage delivered from an aerosol therapy device during tidal breathing, and wish to include the variability resulting from spontaneous breathing as well as morphological differences. We therefore only consider data from experiments where the inhalation flow rate and tidal volume are not controlled.

For studies satisfying this criterion, the standard deviation of the deposition probability among the individual subjects participating in each monodisperse experiment is calculated, and normalized by the mean value. Figures 2.6, 2.7, and 2.8 show the normalized standard deviation for the regional deposition plotted against aerodynamic particle diameter. A third order polynomial is fit to the data with a least squares method (Table 2.2 gives the coefficients). The deposition model calculates an average deposition probability, P_n , for the aerosol particle in each generation n of an extended Weibel 'A' model. Using the average size of the aerosol particle in each generation, a value of the normalized standard deviation, $\sigma_{n, norm}$, is calculated from the fitted curves, and the standard deviation of the deposition probability, σ_n , is calculated from:

$$\sigma_n = P_n \times \sigma_{n, norm} \quad (2.51)$$

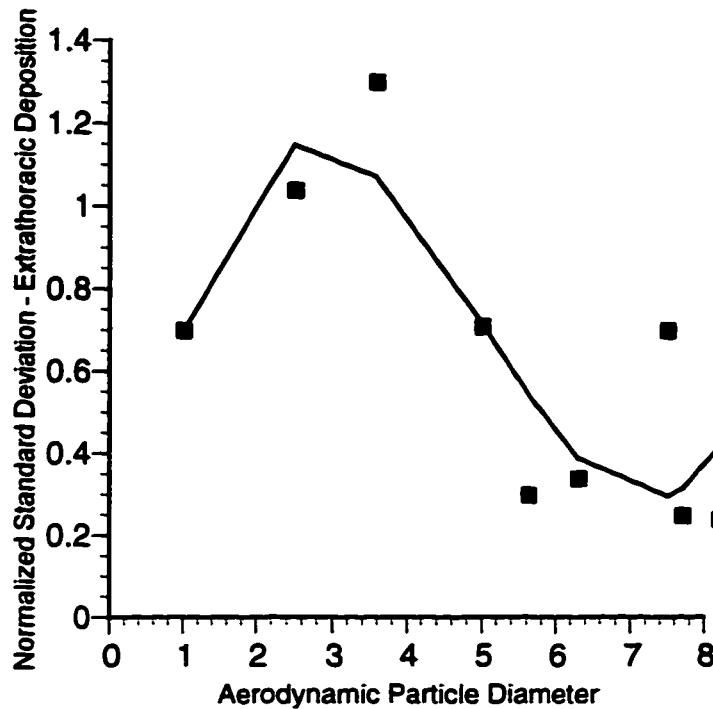


Figure 2.6. Normalized standard deviation vs. particle size for the extrathoracic region showing the 3rd order polynomial fit used in the model. Data from Lippmann & Albert (1969), and Foord *et al.* (1978).

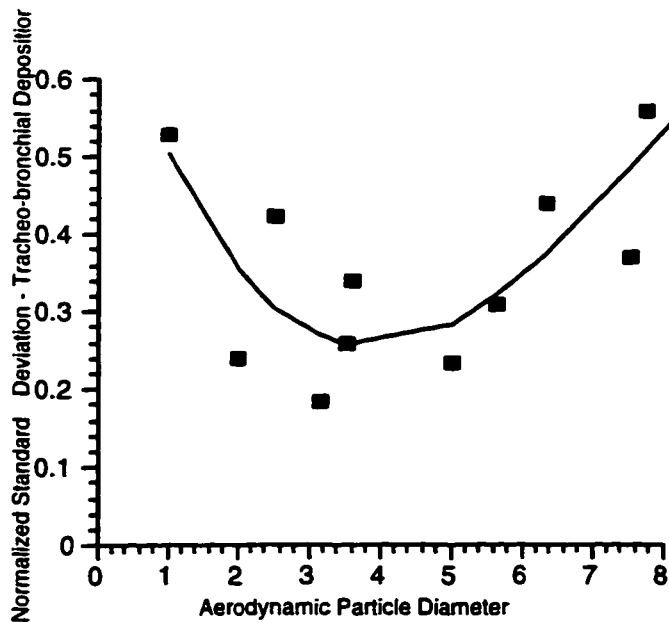


Figure 2.7. Normalized standard deviation vs. particle size for the tracheo-bronchial region showing the 3rd order polynomial fit used in the model. Data from Lippmann & Albert (1969), Chan & Lippmann (1980), Foord *et al.* (1978), Emmett *et al.* (1982), and Lourenço *et al.* (1971).

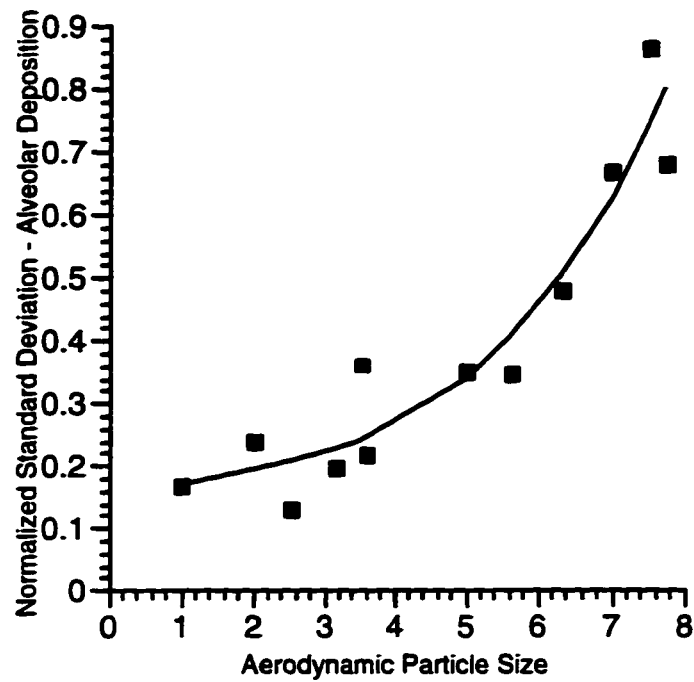


Figure 2.8. Normalized standard deviation vs. particle size for the alveolar region showing the 3rd order polynomial fit used in the model. Data from Lippmann & Albert (1969), Chan & Lippmann (1980), Foord *et al.* (1978), Emmett *et al.* (1982), and Lourenço *et al.* (1971).

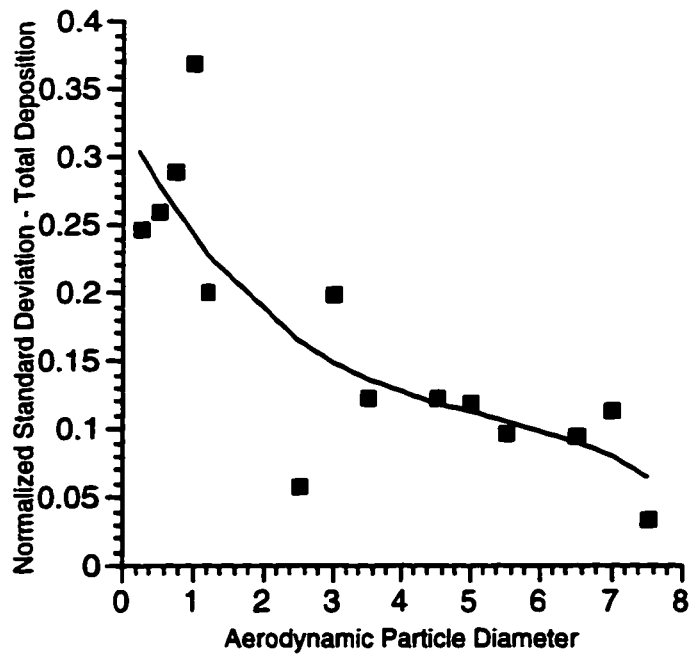


Figure 2.9. Normalized standard deviation vs. particle size for total deposition in the respiratory tract showing the 3rd order polynomial fit used in the model. Data from Lippmann & Albert (1969), Chan & Lippmann (1980), and Foord *et al.* (1978).

	a	b	c	d
Total deposition	-0.0012	0.0176	-0.1022	0.3279
Extrathoracic deposition	0.0183	-0.2739	1.0812	-0.1299
Tracheo-bronchial deposition	-0.0019	0.0470	-0.2771	0.7362
Alveolar deposition	0.0023	-0.0125	0.0468	0.1350

Table 2.2. Values of the coefficients for the 3rd order polynomial fits to the normalized standard deviation vs. particle size data, where $\sigma_{n, norm} = a * d_n^3 + b * d_n^2 + c * d_n + d$

The upper, $P_{n, upper}$, and lower, $P_{n, lower}$, values of the 68% confidence interval for the average deposition probability in each generation are calculated by standard statistical methods:

$$P_{n, upper} = P_n + \sigma_n \quad (2.52)$$

$$P_{n, lower} = P_n - \sigma_n \quad (2.53)$$

To assist in the verification of the procedure with available hygroscopic deposition data, the variation of the total deposition is required. To accomplish this, the procedure just described is used with experimental data on the total deposition of stable particles reported by Heyder *et al.* (1982), Giacomelli-Maltoni *et al.* (1972), Foord *et al.* (1978), and Lippmann *et al.* (1980). The variation of the normalized standard deviation with aerodynamic particle diameter is shown in Figure 2.9 along with the 3rd order polynomial fit. The coefficients for the fitted curve are given in Table 2.2.

2.6 Comparison with experimental data

The total and regional deposition of stable particles in the human respiratory tract *in vivo* has been well studied and reviewed in the archival literature (c.f. Goldberg & Lourenço 1973, Stuart 1973, Lippmann 1977, Lippmann *et al.* 1980, Stahlhofen *et al.* 1989, Morrow & Yu 1993, and references contained therein). Monodisperse aerosols labelled with a gamma ray emitter (typically technecium) are inhaled, and the lungs are imaged with a gamma camera.

Unfortunately, the deposition of hygroscopic aerosols has not been as extensively studied. A few measurements of the absolute total deposition of initially solid NaCl particles is available (Gebhart *et al.*, 1990), and deposition studies show a similar shape to that seen with solid particles if the deposition probabilities are plotted against equilibrium size of the particles (as opposed to the initially inhaled size). Additionally, some data is available for hygroscopic aerosols on the relative deposition between the central and peripheral regions of the lungs (e.g. Chan *et al.* 1994).

The regional distribution (or regional deposition) of aerosols in the lung is often studied by measuring the retention and clearance of aerosols from the respiratory tract. If it is assumed that aerosol deposited in the ciliated tracheo-bronchial airways are removed over a period of a few hours, then aerosol remaining in the lung over longer periods of time should be equivalent to alveolar deposition (Lippmann *et al.* 1980). By comparing gamma camera images over a number of hours, estimates of the tracheo-bronchial and alveolar deposition may be calculated.

There is some uncertainty in the assumption that fast-cleared aerosol is equivalent to bronchial deposition, and slow-cleared aerosol is equivalent to alveolar deposition

(ICRP, 1994). Inhalation studies with humans using aerosol boluses of solid particles and shallow breathing to control the deposition site in the airways have shown that a substantial fraction of the particles deposited in the bronchial airways may be cleared much slower than the conventionally assumed half-time of a few hours (Stahlhofen *et al.* 1987), and that the fraction of aerosol cleared after 24 hours decreases with decreasing particle size (Heyder *et al.* 1988b). Smaldone *et al.* (1988) suggests that solid aerosol particles depositing in the bronchial airways can be transported through the mucous layer, indicating that clearance times for particles in the ciliated bronchial airways can be on the same order as clearance times from the alveolar regions. Gehr *et al.* (1990) and Gehr *et al.* (1996) study this effect theoretically and experimentally, and show that latex particles can be pulled into the mucus layer toward the epithelium by interfacial forces.

This effect has not been proven to occur for the many different types of particles used in inhalation studies, so there may still be value in comparing the results of deposition models against clearance studies. Further validation of our model is given in Section 2.6.2 where we compare against experimental data on the deposition of hygroscopic aqueous aerosols, where the above mentioned uncertainties in interpreting clearance are not important.

2.6.1 Regional Deposition of Stable Aerosols

Figures 2.12, 2.13, and 2.14 show experimental data on the regional deposition of stable aerosols in the respiratory tract, along with the mean deposition probability predicted by our model, and our calculated 68% confidence interval. Breathing parameters used in the model calculations correspond to quiet breathing (tidal volume =

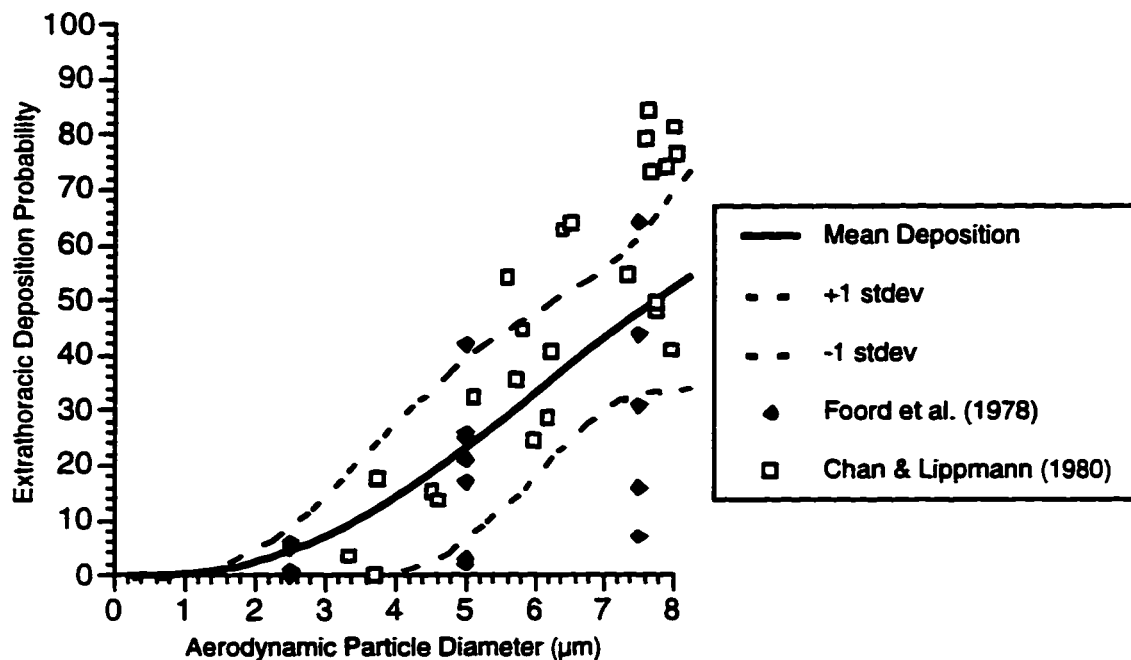


Figure 2.10: Experimental data on the deposition of stable particles in the extrathoracic region of the respiratory tract and the mean deposition and 68% confidence interval predicted by the model for a flow rate of 400 cm³/s and a tidal volume of 0.7 litres.

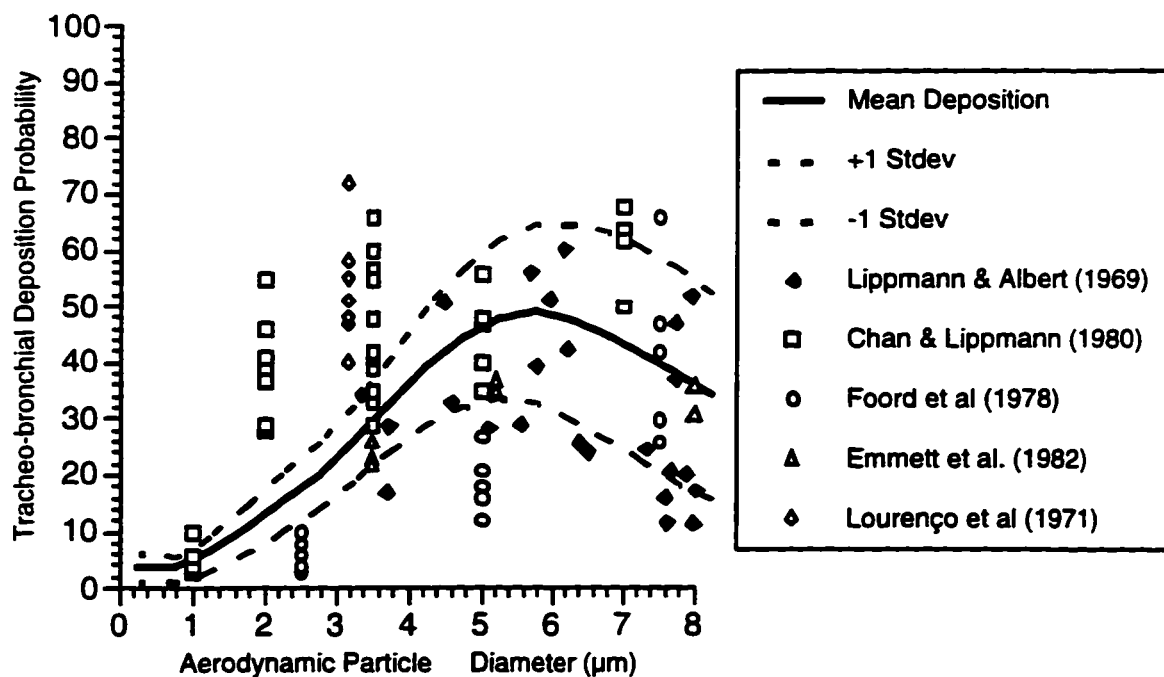


Figure 2.11. Experimental data on the deposition of stable particles in the tracheo-bronchial region of the respiratory tract and the mean deposition and 68% confidence interval predicted by the model for a flow rate of 400 cm³/s and a tidal volume of 0.7 litres.

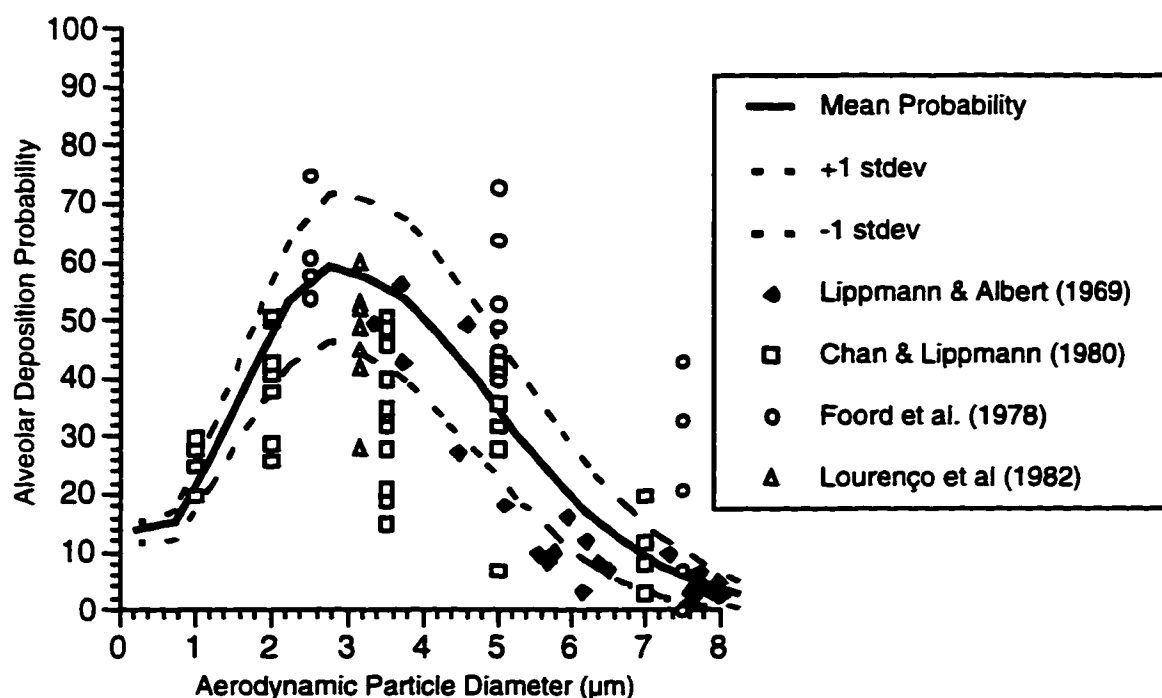


Figure 2.12. Experimental data on the deposition of stable particles in the alveolar region of the respiratory tract and the mean deposition and 68% confidence interval predicted by the model for a flow rate of 400 cm³/s and a tidal volume of 0.7 litres.

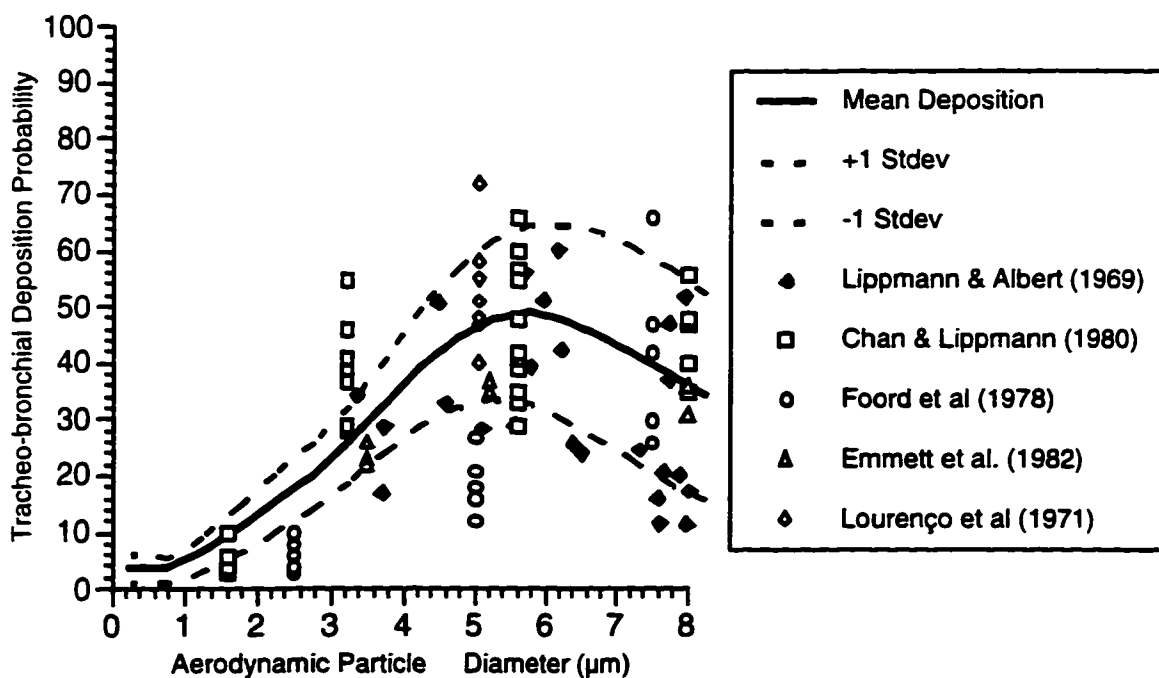


Figure 2.13. Experimental data on the deposition of stable particles in the tracheo-bronchial region of the respiratory tract and the mean deposition and 68% confidence interval predicted by the model for a flow rate of 400 cm³/s and a tidal volume of 0.7 litres. Iron oxide particles are corrected for hygroscopic growth.

700 cm³, inhalation flow rate 400 cm³/s, 4.0 second breathing cycle with a 1.74 second inhalation, 0.2 second breath hold).

In general, agreement between the model calculations and experimental data is good. In the extrathoracic region, 60% of the data points fall within the 68% confidence interval predicted by the model. In the alveolar region, 62% of the data points fall into the 68% confidence interval.

In the tracheo-bronchial region, 47% of the data points fall within the 68% confidence interval. The main cause of this disagreement is the lower mean deposition probability calculated by the model for particles between 2µm and 4µm compared to the experimental values. One possible explanation for this discrepancy is the mild hygroscopicity of iron oxide particles used in some of the studies. Gebhart *et al.* (1989) found that 2.4 µm iron oxide particles had a deposition probability similar to 3.8 µm oil droplets, suggesting approximately a 60% increase in the particle diameter as the iron oxide particles travel through the respiratory tract (ICRP, 1994). Figure 2.13 shows the same data as Figure 2.11, but with the size of the particles used in the iron oxide studies increased by 60%. The agreement with the experimental data is better, with 66% of the data points falling within the predicted 68% confidence interval. Note that the 7µm droplets from Chan & Lippmann (1980) shown in Figure 2.11 are not shown in Figure 2.13, and are not included in the above statistics.

Due to the relative scarcity of experimental data for the regional deposition of aerosols in the respiratory tract, most deposition models are validated against the same experimental data for nonhygroscopic aerosols shown here, and all show reasonable

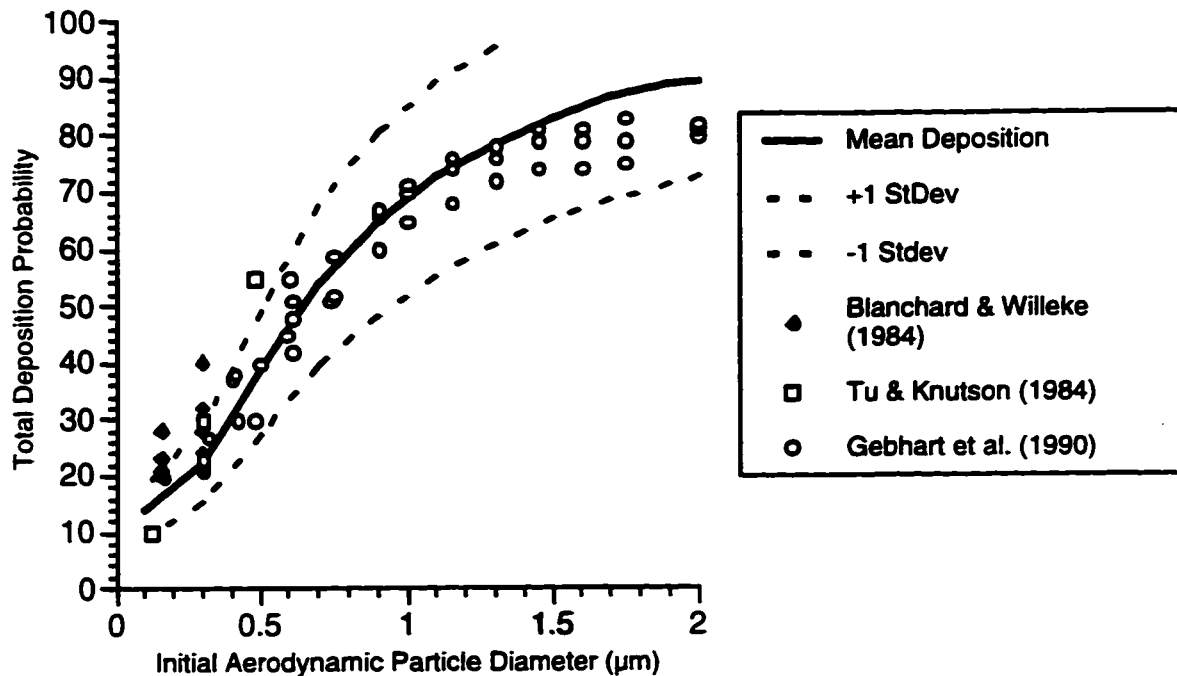


Figure 2.14. Experimental data on the total deposition of initially solid hygroscopic NaCl particles and the mean deposition and 68% confidence interval predicted by the model for a flow rate of 500 cm³/s and a tidal volume of 1.0 litres.

agreement with this data. We therefore do not include direct comparisons of the results of this model with the results of other models.

2.6.2 Total and Regional Deposition of Hygroscopic Aerosols

Gebhart *et al.* (1990) summarize the available experimental data on the total deposition of initially solid hygroscopic aerosols. Figure 2.14 shows this data plotted with the mean deposition probability predicted by the model, along with our calculated 68% confidence interval, for the breathing patterns used in the studies (all studies used a tidal volume of 1000 cm³ and an inhalation flow rate of 500 cm³/s). The mean deposition and variability predicted by the model agrees well with the experimental data, given the small number of subjects in the experiments. It should be noted that the inhalation flow

rate and tidal volume were controlled in the study of Gebhart *et al.* (1990) which may decrease their observed intersubject variability.

To the author's knowledge, there is no published experimental data on the absolute regional deposition of hygroscopic aerosols. However, data on the relative distribution of central to peripheral deposition for hygroscopic aerosols is available (Phipps *et al.* 1989, Phipps *et al.* 1994, and Chan *et al.* 1994). Finlay *et al.* (1996c) compared this experimental data to the predictions of the deposition model presented here and showed that there was no significant difference ($P > 0.05$) between the deposition measurements *in vivo*, and the results of this model. A complete description of the study is beyond the scope of this thesis, and the reader is referred to Finlay *et al.* (1996c) for details. However, a brief overview of the results is presented here for completeness.

In the experimental studies, the penetration index (PI) is defined as the ratio of the counts per pixel in the peripheral region divided by the counts per pixel in the central region. Therefore, the higher the penetration index, the more aerosol which deposits in the peripheral region. A 'd-value' is then defined to compare the penetration indexes of two aerosols such that (Phipps *et al.* 1989):

$$d = \frac{PI_1 - PI_2}{PI_1} \times 100 \quad (2.54)$$

where PI_1 and PI_2 are the penetration indexes of the two aerosols. In the study of Phipps *et al.* (1989), two aerosols of isotonic saline (MMAD 2.6 μm , GSD 1.4 vs. MMAD 5.5 μm , GSD 1.7) were compared. The d-value of the experimental study was 53.7 ± 12.3 (all values in this section are mean \pm standard deviation) and the value predicted by the deposition model was 54.2 ± 10.8 . The next study, by Phipps *et al.* (1994) studied the

deposition of two aerosols with similar size distributions, but with different solution concentrations (MMAD 3.8 μm , GSD 1.4, 0.3% NaCl, vs. MMAD 3.7 μm , GSD 1.4, 4.5% NaCl). Here, the d-value in the experimental study was 4.0 ± 10.5 , and the value predicted by the deposition model was 6.8 ± 10.8 . In the study of Chan *et al.* (1994), the number densities of the droplets were reduced (MMAD 3.8 μm , GSD 1.4, 0.3% NaCl, vs. MMAD 3.7 μm , GSD 1.4, 4.5% NaCl) to enhance the effects of the hygroscopic growth. The experimentally determined d-value was 5.6 ± 10.6 , and the d-value predicted by the deposition model was 10.9 ± 15.4 . Again, no difference ($P>0.05$) was found between the *in vivo* and computational results for either the mean value or the variance of the difference in peripheral to central deposition.

3. Regional Dosage Predictions from Medical Nebulizers

3.1 Introduction

As discussed earlier, our goal is to develop *in vitro* methods for evaluating the ability of different therapeutic aerosol delivery devices to deliver drugs to the respiratory tract. Deposition models such as those described in the previous section of this manuscript provide a way of estimating the regional deposition probabilities of inhaled aerosols, but cannot be used directly with therapeutic aerosol devices without considerable attention to a number of aspects. The purpose of Section 3 of this manuscript is to describe these aspects and the work we have done in order to use a deposition model to estimate regional dosages delivered to the respiratory tract by medical nebulizers.

It is useful to begin by considering what kinds of aerosols are produced by medical nebulizers, and what information will be required to calculate the regional deposition probabilities. For use in a nebulizer, drugs are usually formulated as an

aqueous solution (i.e. the drug is dissolved in water) or as a suspension (i.e. the drug is milled or dried into small particles and suspended in the water). In addition to the drug, the solution may contain NaCl and other salts in order that the tonicity and pH of the produced aerosol is similar to that of the airway surface fluid lining the respiratory tract. Surfactants and preservatives may also be present.

The aerosols produced by nebulizers will therefore be aqueous droplets, usually approximately lognormally distributed with a mass median diameter of between 3 and 9 μm , and a geometric standard deviation between 1.5 and 2.0. Nebulized aerosols can be expected to change size in response to changes in the temperature and relative humidity of their environment. This has two important implications. First, if the relative humidity of air entering the nebulizer is less than the equilibrium relative humidity of the droplets (see discussion of equation (3.7)), then the droplets will humidify the air in the nebulizer. The solution concentration within the droplets and nebulizer reservoir may then be different, and both will change with time. Second, a deposition model which accounts for the hygroscopic nature of the droplets will be required to correctly predict where they will deposit in the respiratory tract.

To use a hygroscopic deposition model to predict the deposition of a nebulized aerosol in the respiratory tract, the droplet size distribution, solution concentration in each droplet, and the droplet number density of the aerosol are required at the entrance to the respiratory tract. In the remainder of this chapter we discuss a methodology for determining these quantities. In short, the droplet size distribution is readily measured using, for example, phase Doppler anemometry. This measurement can be used to determine an estimate of the number density by considering a mass balance in the

nebulizer (see Section 3.3.1 for a detailed description). The solution concentration in the droplets cannot be readily measured directly, and requires additional considerations.

3.2 Nebulizer Types

There are three main types of nebulizers available today: unvented jet nebulizers, vented jet nebulizers, and ultrasonic nebulizers. Each type of nebulizer requires a different measurement approach, and it is useful to first review the performance features of each nebulizer type.

The simplest of the three nebulizer types is the unvented jet nebulizer, shown schematically in Figure 3.1. High pressure air (from a compressor, for example) enters through the bottom of the nebulizer, and is forced through a venturi (4). As the speed of the fluid increases through the venturi, the pressure decreases, and liquid is drawn into the airstream from the reservoir, forming the droplets. To exit the nebulizer, the aerosol passes through baffles (5) which allow only a certain size range of droplets to escape. Droplets outside this size range impact on the sides of the nebulizer and are returned to the reservoir in the bowl of the nebulizer (3) for renebulization. Droplets formed at the venturi are called primary droplets, and it has been estimated that over 99% of the primary droplets are returned to the reservoir for renebulization (Mercer *et al.* 1968, Smye *et al.* 1991).

Jet nebulizers are typically driven at compressor flow rates of approximately 6 liters/min, much lower than typical resting inhalation flow rates (for which 18 liters/min, or 300 cm³/s is a typical value). A T-mouthpiece (2) is used to mix in ambient air to make up the patient's inhalation flow rate.

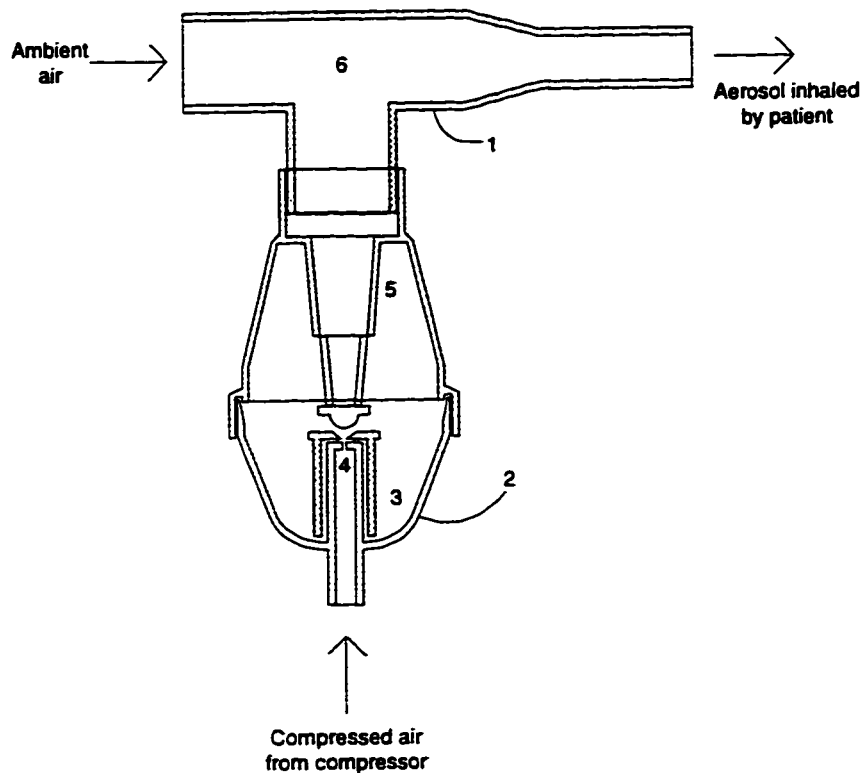


Figure 3.1. A schematic of an unvented jet nebulizer (2) with attached T-mouthpiece (1). The nebulizer has a reservoir (3), a venturi (4), and baffles (5). The aerosol produced by the nebulizer is mixed with ambient air at (6), which is also the point that the droplet size distribution is measured by the PDA system.

An important performance feature of unvented jet nebulizers is that ambient air entrained to make up the patient's inhalation flow rate does not travel through the droplet production region of the nebulizer. Therefore, the aerosol that exits the nebulizer (prior to mixing with ambient air at the junction of the T-mouthpiece) is independent of patient breathing.

Some jet nebulizers contain a vent in the body of the nebulizer to allow ambient air to pass through the nebulizer body. Here, these nebulizers are termed vented jet nebulizers, and a typical such nebulizer is shown schematically in Figure 3.2. The main

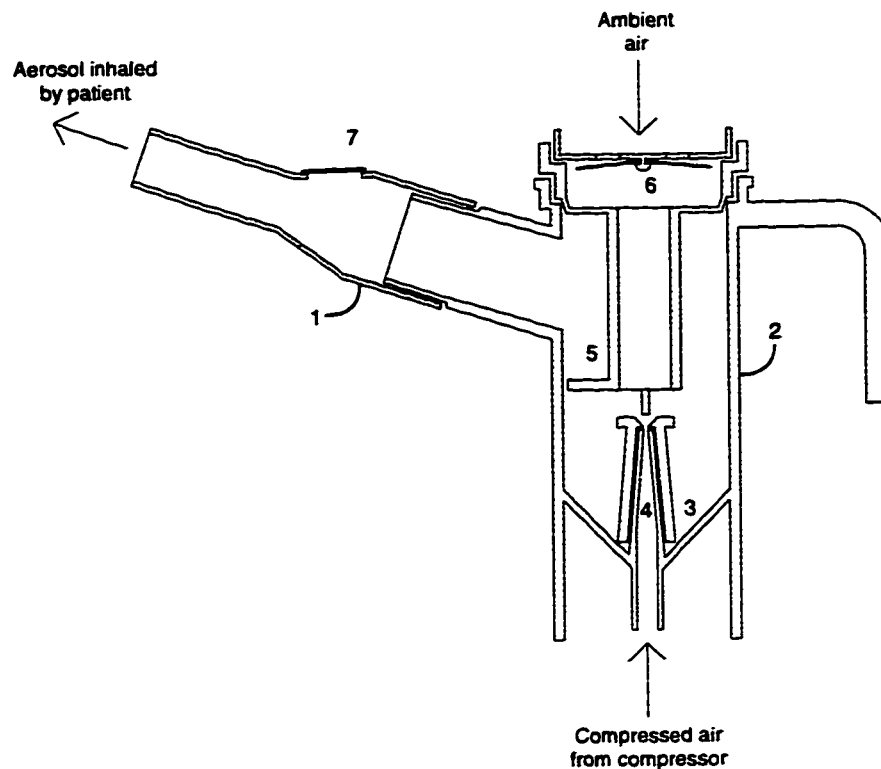


Figure 3.2. A schematic of a vented jet nebulizer (2) and attached mouthpiece (1) shown during inhalation. The nebulizer includes the reservoir (3), venturi (4) and baffles (5). When the patient inhales, air is drawn through the open inlet valve (6). During exhalation, the inlet valve (6) closes, and air is expelled through the exhalation valve (7).

difference between unvented and vented jet nebulizers is the air is drawn through the bowl of vented nebulizers during patient inhalation, in contrast to unvented jet nebulizers where ambient air needed to make up the patient's inhalation flow rate is drawn only through the mouthpiece.

It is important to note that during inhalation, the flow rate of air exiting the nebulizer mouthpiece is equal to the inhalation flow rate of the patient, which can vary in time. For many vented jet nebulizers, the mass flow rate of liquid leaving the nebulizer increases as the inhalation flow rate increases. For this reason, vented jet nebulizers are sometimes termed "breath enhanced" nebulizers. Depending on the design of the vented nebulizer, the number density of the aerosol (i.e. the number of droplets per cm^3) may

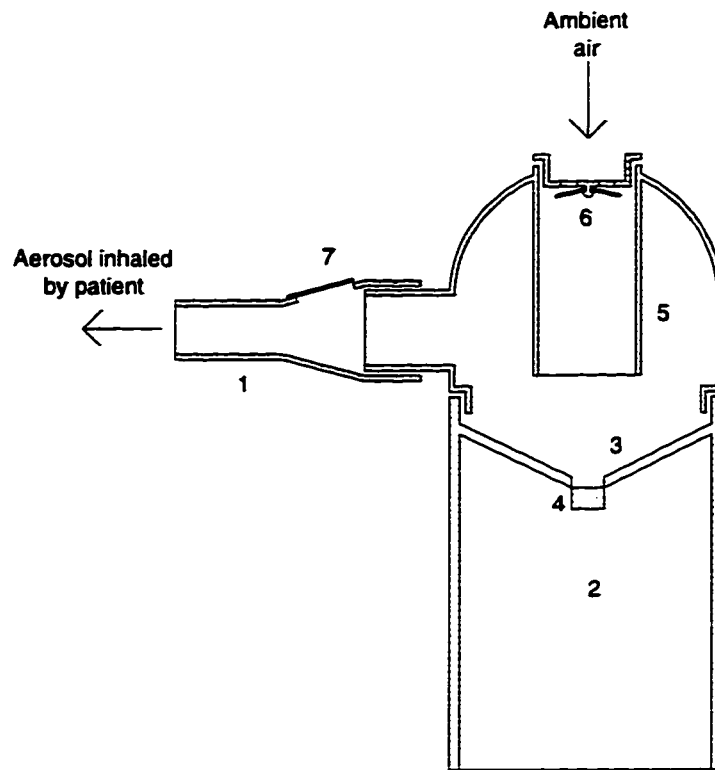


Figure 3.3. A schematic of an ultrasonic nebulizer (2) and attached mouthpiece (1) shown during inhalation. The nebulizer includes the reservoir (3), pizo-electric crystal (4) and baffles (5). Here, when the patient inhales, air is drawn through the inlet valve (6). During exhalation, the inlet valve (6) closes, and air is expelled through the exhalation valve (7). The electronics for the piezo-electric crystal are not shown.

increase, decrease, or remain constant with increasing flow rate (Knoch & Wunderlich, 1994). During exhalation, aerosol is still produced by the vented nebulizer and exits at a rate equal to the mass flow rate of the compressor air. The volumetric flow rate out of a vented jet nebulizer is therefore unsteady, and dependent on the breathing parameters of the patient.

Ultrasonic nebulizers do not use a compressed air source to produce the aerosol droplets. Instead, vibrations in the reservoir solution caused by a submerged piezo-electric crystal produce instabilities in the fluid that cause droplets to be formed (Mercer, 1981). Often, a series of one-way valves directs inhaled air through the nebulizer bowl as

in a vented jet nebulizer, and directs exhaled air through a vent in the mouthpiece.

However, during exhalation, there is often no air flow through the nebulizer, but aerosol is still produced. This aerosol collects in the dome of the nebulizer, so that when the patient begins the inhalation maneuver, the number density of aerosol droplets is initially very high, but then drops to a lower level for the remainder of the inhalation cycle.

3.3 Determining solution concentration within aerosol droplets output by nebulizers

The output characteristics of jet and ultrasonic nebulizers, such as aerosol size distribution, nebulizer solution temperature and concentration, and nebulization rate, have been reviewed in the literature (for example, Mercer *et al.* 1968, Mercer 1981, Clay *et al.* 1983, Sterk *et al.* 1984, Phipps & Gonda 1990, Smye *et al.* 1992, and Langford & Allen 1993). Statistical models of nebulizer performance have also been presented (Smye *et al.* 1991). However, the solution concentration of the aerosol droplets is not readily measured directly, but can be calculated from other measurements. The methodology to calculate the concentration of solute within aerosol droplets will first be described for unvented jet nebulizers producing an aerosol from an aqueous solution. Modifications to this procedure in order to adapt it for vented jet and ultrasonic nebulizers will then be discussed. Modifications to this methodology to include drugs formulated as suspensions is currently being investigated, and is not included here.

3.3.1 Theory

Consider a control volume surrounding an unvented jet nebulizer (Figure 3.4).

Conservation of mass indicates that during a given time period, t , the change in mass of the solution in the nebulizer is given by:

$$\Delta m_{neb} = m_{out} - m_{in} \quad (3.1)$$

where m_{neb} is the mass of solution in the nebulizer, m_{in} is the mass of water vapor entering the nebulizer during time t , and m_{out} is the total mass leaving the nebulizer during time t and is given by:

$$m_{out} = m_s + m_l + m_v \quad (3.2)$$

where m_s is the mass lost as solute, m_l is the mass lost as liquid water, and m_v is the mass lost as water vapor. By determining m_s , and m_l , the average solution concentration of the droplets over the time period t can be calculated. Note that the mass rate of air entering the nebulizer equals the mass rate of air leaving the nebulizer, and therefore, assuming that it does not interact chemically with the water or solutes, it does not appear in Equation (3.2).

In Equation (3.1), the change in total mass of solution in the nebulizer, Δm_{neb} , is easily measured by weighing the nebulizer before and after the time period t . The mass of water vapor entering the nebulizer, m_{in} , can be calculated knowing the temperature and relative humidity of the ambient air with the equation:

$$m_{in} = c_{w,in} \cdot Q \cdot t \quad (3.3)$$

where Q is the volume flow rate of air entering the nebulizer, and $c_{w,in}$ is the water vapor concentration in this air. The concentration of water vapor c_w is given by the

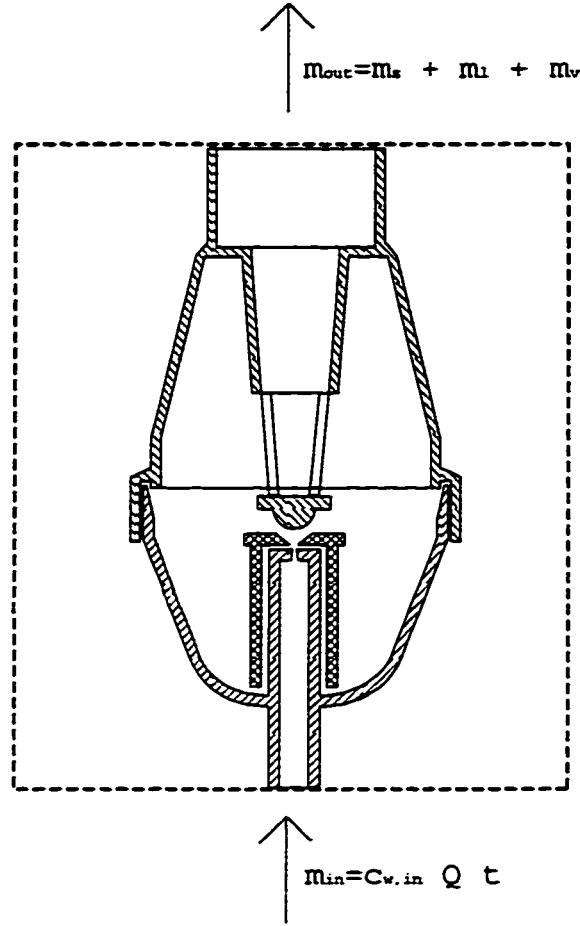


Figure 3.4. A schematic of the control volume around a jet nebulizer.

Antoine equation (Reid, Prausnitz, & Sherwood, 1977):

$$c_w = RH \cdot 363.8 \cdot \exp\left(\frac{-4943}{273.15 + T_a}\right) \quad (3.4)$$

where T_a is the air temperature in degrees Celsius, RH is the relative humidity of the air ($RH < 1.0$), and c_w is given in g/cm^3 . To calculate $c_{w,in}$, the temperature and relative humidity of the ambient air entering the nebulizer are used in Equation (3.4).

The mass of solids leaving the nebulizer, m_s , in equation (3.2) can be measured by collecting the aerosol droplets on a filter, then drying the filter and weighing the collected solids. The mass leaving the nebulizer as water vapor, m_v , is calculated in a

similar way to m_{in} , but using the dry bulb temperature of the aerosol leaving the nebulizer. Alternatively, m_s can be calculated by measuring the amount of solute remaining in the nebulizer from the concentration and mass of the reservoir solution at the end of each minute. Any solute not present in the reservoir solution will have left the nebulizer in droplets.

Equations (3.1) and (3.2) can now be solved for m_l , and the average solution concentration in the droplets c_{avg} is then given by:

$$c_{avg} = \frac{m_s}{\left(\frac{m_s + m_l}{\rho} \right)} \quad (3.5)$$

where ρ is the density of the solution, and is given by (Ferron, 1977):

$$\rho = \frac{m_w + m_s}{m_w + \left(\frac{m_s}{\rho_s} \right)} \quad (3.6)$$

where ρ_s is the density of the solid. It is assumed that the density of the solution is independent of the solution concentration to allow equations (3.1) - (3.5) to be solved without an iterative method. This assumption will be justified in Section 3.3.2.2.

The final piece of information that is required to calculate the solution concentration in the droplets is the relative humidity of the air leaving the nebulizer, so that the value of m_v can be calculated. However, the air output by medical nebulizers typically has a relative humidity of greater than 95% (often greater than 99%), and standard measurement techniques do not have sufficient accuracy in this range. Measurements are further complicated by the presence of the droplets. Fortunately, as will be shown later, the droplets leaving the nebulizer are in equilibrium with the

surrounding air, and this allows us to accurately predict the relative humidity of the output air.

Aerosols output by medical nebulizers are typically polydisperse, with geometric standard deviations ranging from approximately 1.5 - 2.0, indicating that these aerosols have a wide range of particle sizes. Evaporation rates and stabilization times for hygroscopic droplets are strongly dependent on droplet size (Ferron & Soderholm, 1990), with smaller droplets having higher evaporation rates and shorter stabilization times. Thus, the smaller droplets may have a different concentration from the larger droplets. However, droplets greater than 1 μm in diameter will all have the same concentration if they are in equilibrium with their environment. To see this, consider that an aerosol droplet in equilibrium with its environment satisfies the following equilibrium condition (Morrow, 1986):

$$RH = C_K \cdot C_R \quad (3.7)$$

where RH is the relative humidity of the surrounding air, C_K is the Kelvin correction for surface curvature, and C_R is the vapor pressure reduction due to dissolved solids (Raoult's Law for an ideal solution, or an expression for a non-ideal solution such as Cinkotai (1971) for NaCl). For droplets greater than approximately 1 μm in size, the Kelvin correction causes changes in the droplet size of less than 0.1% and can be neglected (Morrow, 1986). Thus, since there is no dependence on droplet diameter in C_R , the solution concentration in all droplets greater than approximately 1 μm in diameter will be the same if the aerosol is in equilibrium with its environment.

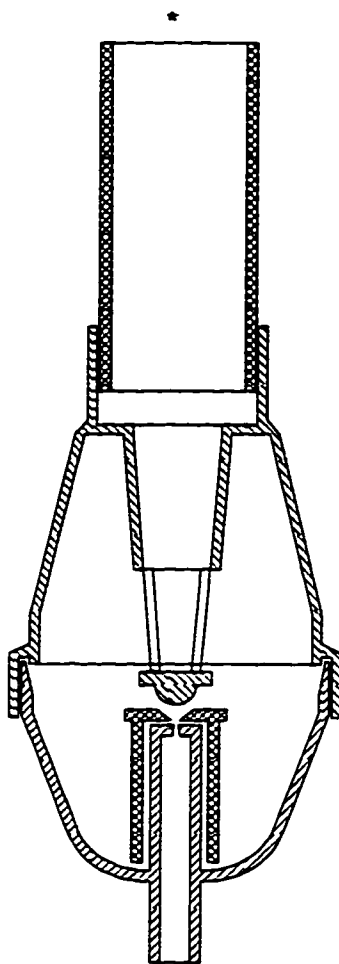


Figure 3.5. A schematic of a vented jet nebulizer with a length of tube attached vertically for measuring the equilibrium condition of the aerosol leaving the nebulizer. The asterisk marks the approximate measuring point.

3.3.2 Experimental Validation

3.3.2.1 Droplet Equilibrium

Before the above methodology can be applied to a nebulizer, it must be verified that droplets leaving the nebulizer are in equilibrium with the surrounding environment. The output distributions of three DeVilbiss Pulmo-Neb[®] disposable nebulizers (DeVilbiss Health Care (Canada) Inc., Barrie, ON, Canada) delivering normal saline (0.9% NaCl)

were measured using a phase Doppler anemometer, or PDA (Dantec Electronics Inc., Mahwah, NJ, USA), with 4 different lengths of plastic tubes (5 cm, 10 cm, 25 cm, and 40 cm in length, inside diameter 2.54 cm) attached vertically to the opening of the nebulizer (Figure 3.5). The tubes were attached vertically to minimize deposition of the aerosol due to gravitational settling (the settling velocity of the droplets considered here is at least an order of magnitude smaller than the fluid velocity, so sedimentation is not expected to influence the distribution significantly). Ambient laboratory conditions during the data collection were 23.0 ± 0.2 °C, and $34.0 \pm 2.5\%$ relative humidity measured by a calibrated thermometer and a hygrometer (Fisher Scientific, Mississauga, ON) respectively. The flow rate through the nebulizer was measured at 6.6 ± 0.1 litres/min by water displacement. At this flow rate, the 40 cm extension gives the aerosol approximately 2 seconds of transit time beyond the nebulizer exit before its exposure to ambient conditions.

Each nebulizer was first measured without an extension, then with each extension added. This procedure was repeated 10 times for each nebulizer to obtain a statistical measure of the nebulizer performance. Figure 3.6 shows the difference between the average diameter of the droplets measured without an extension and the diameter of the droplets measured with each of the extensions added. The dotted lines indicate the 4% measurement error of the phase Doppler anemometer. As can be seen in Figure 3.6, the measured average diameter of the droplets does not change significantly as the extra lengths of tubes are added to the exit of the nebulizer. Additionally, a statistical comparison showed no significant difference between the measurements (Student's *t*-test,

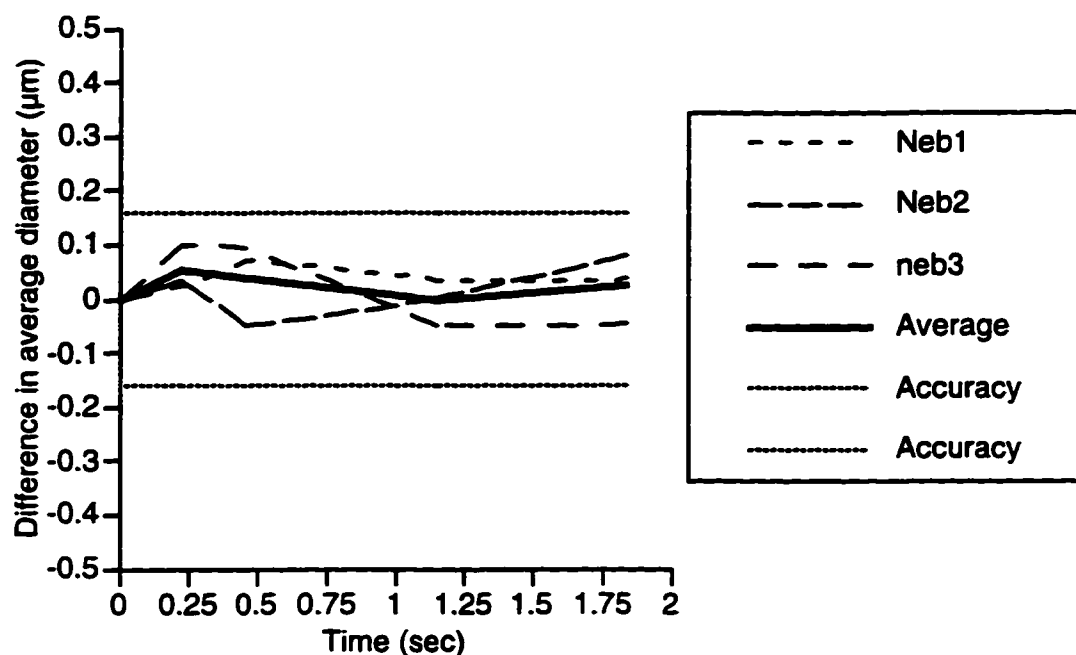


Figure 3.6. The change in average diameter of droplets with time after leaving the nebulizer, and before interacting with the ambient air. The dotted lines indicate the measurement error of the phase Doppler anemometer (4%)

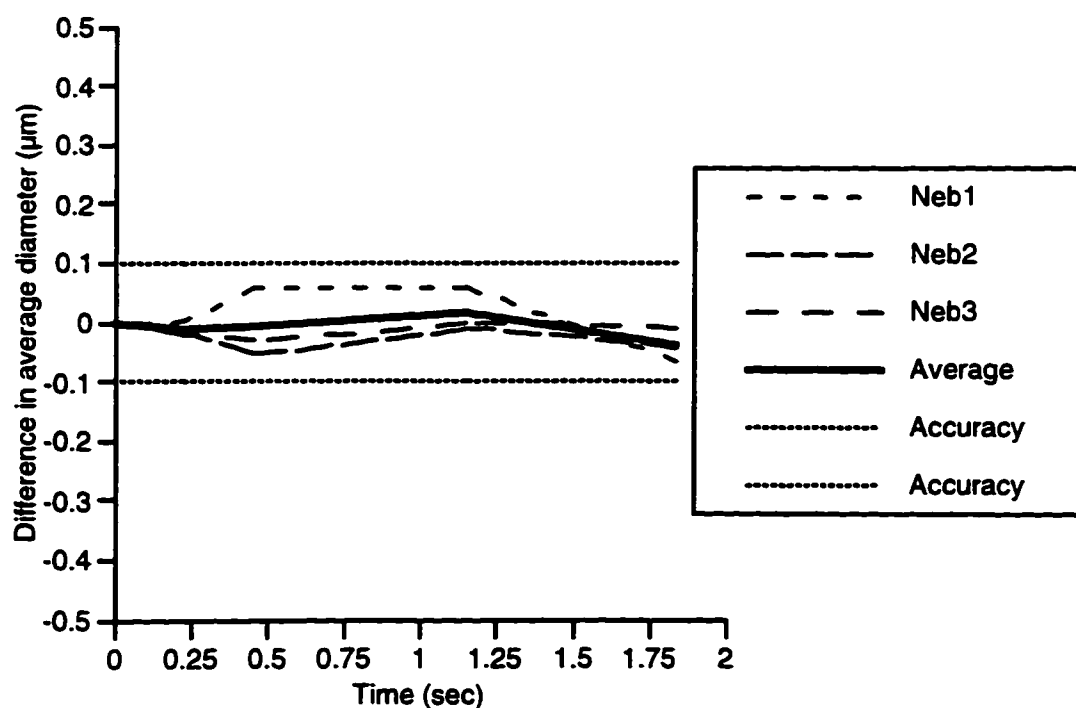


Figure 3.7. The change in average GSD of the droplet distribution with time after leaving the nebulizer, and before interacting with the ambient air. The dotted lines indicate the measurement error of the phase Doppler anemometer (4%)

$P > 0.1$). From this we can conclude that the average size of the droplets is not changing as they traverse the length of the extensions.

It has been shown (Ferron & Soderholm, 1990) that smaller droplets have a much faster stabilization time than larger droplets. This may manifest itself as a change in the distribution, without a significant change in the average diameter. To check this, similar tests to those performed on the average droplet diameter were performed with the geometric standard deviation (GSD) of the aerosol. Figure 3.7 shows the variation of the GSD of the droplet distribution with the addition of different lengths of tubes, and the measurement error of the PDA system. Again, both the graph, as well as statistical tests (F test, $P > 0.1$) indicate that there is no significant change in the GSD of the aerosol distribution.

Ferron & Soderholm (1990) estimate that the time required for a *single* pure water droplet with a size equal to the mass median diameter (MMD) of the droplet distribution measured here (on average, about $8\text{ }\mu\text{m}$ for these three nebulizers) to reach equilibrium with 99.5% air is approximately 20 seconds. Approximately the same time is required for a single solid salt particle to absorb water and become isotonic. This seems to indicate that the droplets may not be in equilibrium when they exit the nebulizer, and that the time allowed for the droplets to stabilize in this experiment is too short. However, Eisner *et al.* (1990) considered the stabilization time of aerosol clouds similar to those measured here at the exit of the nebulizer, including the effect of two-way coupling between the phases (see section 2.5.2 for more details) and predict stabilization times of only a few tenths of seconds. By considering aerosol clouds and the ability of the droplets to affect the relative humidity of the surrounding air, the amount of water that

must evaporate/condense from each droplet is small, and thus the length of time needed for the system to come into equilibrium is short. Additionally, if >99% of the droplets are returned to the reservoir then the droplet number concentration may be up to 2 orders of magnitude greater inside the nebulizer than in the aerosol exiting the nebulizer. This will have the effect of further reducing the amount of water from each droplet that must evaporate to humidify the air in the nebulizer, and further reduce the length of time required for the aerosol to come into equilibrium.

Recently, Ferron *et al.* (1997) calculated the hygroscopic growth of droplets through three nebulizers using the hygroscopic growth model of Ferron & Soderholm (1990) with a simple correction for the relative humidity of the air surrounding the droplets and found that more than 97% of any droplet growth happened in the first 0.1 seconds, which is approximately the average residence time of a droplet in the tested nebulizers. In the case of the PulmoNeb studied here, Ferron *et al.* show very little growth of the droplets from the point of creation to the exit of the nebulizer, and little change in the concentration in the droplets, which supports the conclusions drawn here. However, Ferron *et al.* also suggest that this is only the case with the PulmoNeb, and not a general conclusion for all nebulizers.

If this last suggestion is true, then the method described here would not be useful. However, Ferron *et al.* also predict large changes in the MMD and GSD of the aerosol during the next 3 seconds of the aerosol's existence. These large changes should be measurable using the technique described above, but are not observed in any of three different nebulizer models studied here. Ferron *et al.* do not present experimental evidence to support their conclusions. Additionally, calculations with the two-way

coupled model presented in Section 2 indicate that the droplets are in equilibrium upon exiting the nebulizer. These issues are addressed in more detail in Section 3.5.

Based on the theoretical considerations and experimental evidence, we can conclude that the droplets are in equilibrium as they exit the nebulizer. Further, from the discussion of Equation (3.7), we know that for all droplets with diameters greater than approximately 1 μm , the solution concentration in the droplets will be the same.

3.3.2.2 Droplet Solution

The methodology to measure the solution concentration described above is applied to the same model of nebulizer discussed above (DeVilbiss Pulmo-Neb[®] disposable nebulizer) driven by the same compressor (DeVilbiss Pulmo-Aide[®] compressor) and delivering two unit dose nebules (a total of 5 ml of solution). Each Ventolin[®] nebule (DIN 00897345, Glaxo Canada Inc., Mississauga, ON, Canada) contains 2.5 mg of salbutamol sulfate dissolved in 2.5 ml of normal saline (0.9% NaCl). Ambient laboratory conditions during data collection were 23.0 ± 0.2 °C, and $25.0 \pm 2.5\%$ relative humidity. The flow rate through the nebulizer was measured as 6.6 ± 0.1 l/min. A random sample of nebulizers from the same manufacturing lot was used to give a statistical sample of performance.

To calculate the concentration of the droplet solution, a nebulizer was weighed after the addition of the two Ventolin[®] nebules, then run for one minute, during which all droplets exiting the nebulizer were collected on a filter (Watman EPM2000) that collects 99.997% of particles >0.3 μm (Figure 3.8). At the end of the minute, the nebulizer was reweighed, and a 50 μl sample of the remaining nebulizer solution was removed to

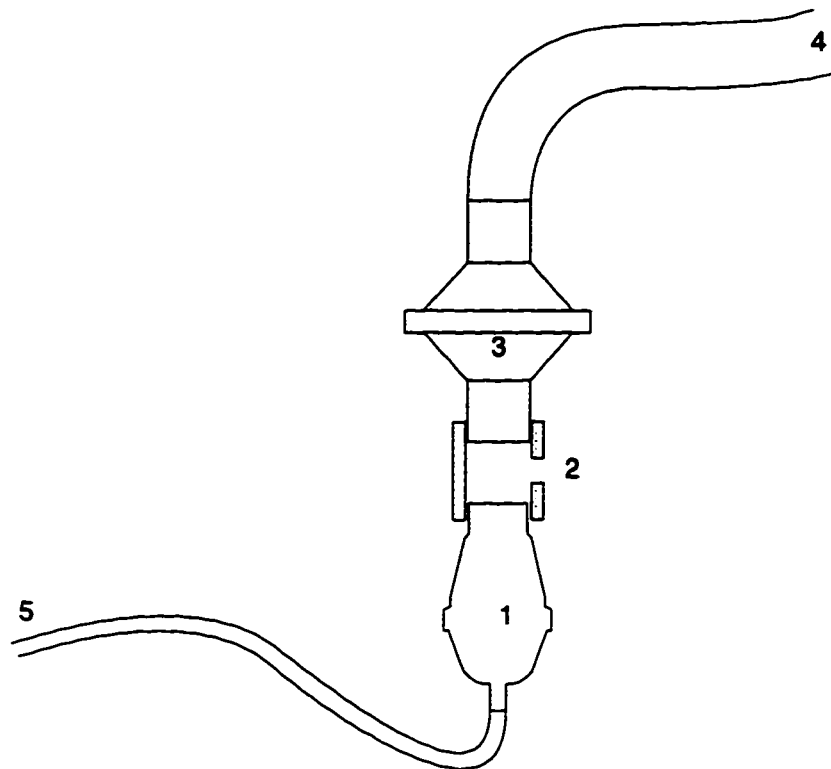


Figure 3.8. A schematic of the experimental setup to collect the solids output by a nebulizer. The nebulizer (1) is attached to the filter (3) via a short section of tube (2) with holes to allow ambient air to be entrained to match the flow rate of the vacuum pump. The compressor and vacuum pump are attached to the test apparatus via hosing (5) and (4) respectively

measure the solute concentration by freezing point osmometry (model 5004, Precision Systems Inc., Natick, Mass., USA).

For the second minute, the nebulizer was first weighed, then run for a minute, during which time the droplets were again collected on a filter. The nebulizer was weighed again, and another sample of the nebulizer solution was removed and its concentration measured. This procedure was repeated until the nebulizer began to operate intermittently. The results of these measurements are shown in Table 3.1. Data was not collected while the nebulizer operated intermittently. When the nebulizer is not running continuously, there is no droplet production, and no evaporation from the

Minute	Δm_{neb} (g)	m_s (mg)	Concentration (mg/ml)
1	0.302 ± 0.004	2.15 ± 0.08	10.21 ± 0.4
2	0.282 ± 0.007	2.10 ± 0.06	10.26 ± 0.03
3	0.267 ± 0.006	2.03 ± 0.07	10.41 ± 0.04
4	0.278 ± 0.004	2.18 ± 0.03	10.61 ± 0.05
5	0.276 ± 0.002	2.18 ± 0.01	10.79 ± 0.07
6	0.259 ± 0.005	2.05 ± 0.06	11.01 ± 0.04
7	0.265 ± 0.002	2.20 ± 0.02	11.28 ± 0.04

Table 3.1. Total mass Δm_{neb} leaving the nebulizer during each minute, the mass of solids m_s collected on the filter during each minute, and the measured concentration of the solute in the nebulizer solution at the end of each minute, for an initial volume of 5.0 ml in the nebulizer. All values are mean \pm standard error.

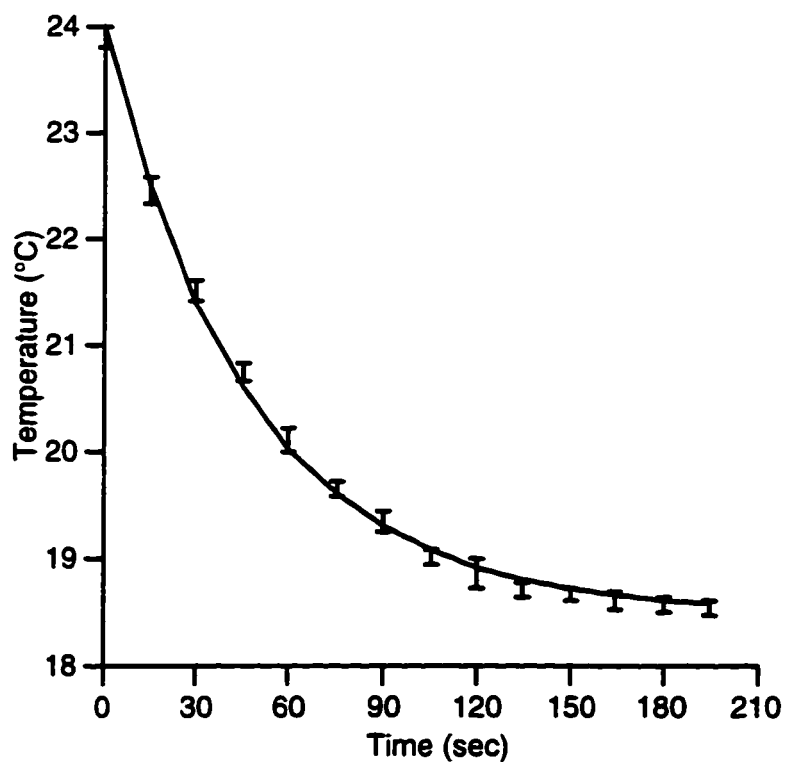


Figure 3.9. Plot of the temperature of the air exiting the nebulizer as a function of time (points with error bars) and Equation 3.8).

droplets, so the output water vapor content is no longer a simple function of time (c.f. Equation 3.9).

The temperature of the air leaving the nebulizer was measured with a thermocouple in the jet exiting the nebulizer and protected from droplet impaction by a small plastic shield, and was found to have an exponential character. Figure 3.9 shows the measured data and the function:

$$T_a = 18.5 + 5.5 \cdot \exp(-1.29 \cdot t) \quad (3.8)$$

where t is the time in minutes. This equation is substituted into the Antoine equation (Equation 3.4) to give an equation for the output concentration of water vapor, $c_{w,out}$, as a function of time. The output relative humidity of medical nebulizers delivering isotonic solutions has been estimated as greater than 99% (Ferron & Gebhart, 1988). Since we have found that the droplets are in equilibrium upon exiting the nebulizer, we can use Equation (3.8) to give us the relative humidity of the air exiting the nebulizer.

If the droplets exiting the nebulizer have a solution concentration equal to the initial concentration of the nebules (i.e. 0.9% NaCl, and 1 mg/ml salbutamol sulfate), the equilibrium relative humidity would be 99.48%. For a solution 10% greater than the initial concentration of the nebules, the equilibrium relative humidity would be 99.41%. Thus, the change in solution concentration during nebulization has little effect on the output relative humidity, and a constant output relative humidity of 99.4% is assumed here to allow Equations (3.1) - (3.5) to be solved without an iterative method.

Substituting Equation (3.8) into Equation (3.4) with a relative humidity of 99.4% gives:

$$c_{w,out} = 361.6 \cdot \exp\left(\frac{-4943}{291.65 + 5.5 \cdot \exp(-1.29 \cdot t)}\right) \quad (3.9)$$

Equation (3.9) is then multiplied by the flow rate of air out of the nebulizer to convert the units to g/sec, and integrated numerically to give the total amount of water vapor leaving the nebulizer in a given time period.

Integrating Equation (3.9) with the present data, the amount of water leaving the nebulizer as vapor during the first minute of operation is 0.124 ± 0.002 g, so that from Table 3.2 and Equations (3.1) and (3.2) we find the amount of solution leaving the nebulizer is $m_l + m_s = 0.212 \pm 0.005$ g. The average concentration of the solution in the droplets is then calculated by equation (3.5)

$$c_{sp} = \frac{0.00215 \pm 0.00008}{\left(\frac{0.212 \pm 0.005}{1.004} \right)} = 0.0102 \pm 0.0004 \frac{g}{ml} \quad (3.10)$$

Values for the other minutes of nebulizer operation are given in Table 3.2. In each minute, the average solution concentration within the droplets is within 2% of the concentration measured in the nebulizer solution at the end of the minute.

If the droplets are evaporating slightly to humidify the air in the nebulizer, then the concentration of the solution in the droplet can be expected to increase slightly as it moves from the point at which it was formed at the venturi, to the point at which it comes into equilibrium with the surrounding air. Therefore, at any given point in time, the concentration of solution in the droplets will be slightly different (in fact, slightly higher) than the concentration of the solution in the nebulizer reservoir, but the two concentrations will remain close, and they both will increase at approximately the same rate. This is seen in the above results in which the droplet solution concentration *averaged* over each minute is equal to the measured nebulizer reservoir solution concentration at the *end* of each minute.

Minute	Calculated average droplet concentration (mg/ml)	Measured nebulizer solution concentration (mg/ml)
1	10.2±0.4	10.21±0.04
2	10.2±0.5	10.26±0.03
3	10.4±0.5	10.41±0.04
4	10.5±0.4	10.61±0.05
5	10.6±0.2	10.79±0.07
6	10.9±0.4	11.01±0.04
7	11.3±0.3	11.28±0.04

Table 3.2. The calculated average concentration of the solution in the droplets over one minute of nebulizer operation compared to the concentration of the nebulizer solution measured at the end of the minute for an initial concentration of the nebulizer solution of 10.0 mg/ml (1.0 mg/ml salbutamol sulfate, and 9.0 mg/ml NaCl). All values are mean ± standard error.

Start Time (min.)	End Time (min.)	Averaging interval (min.)	Average Droplet Concentration (mg/ml)
0	7	7	10.6±0.1
1	7	6	10.7±0.1
2	7	5	10.8±0.1
3	7	4	10.9±0.1
4	7	3	11.0±0.17
5	7	2	11.1±0.2
6	7	1	11.3±0.3

Table 3.3. The calculated average concentration of the droplets produced by the nebulizer when averaging over different time intervals with Equation (3.5) from the data in Table (3.1). The measured concentration of the nebulizer reservoir solution at the end of the 7th minute of operation was 11.28±0.04 mg/ml.

Because the concentration is increasing over the nebulization period, the average solution concentration calculated with Equation (3.5) will depend on the time interval over which the averaging occurs. To investigate this, the concentration increase in the droplets is calculated from the data in Table (3.1) using time intervals from 1 to 7 minutes. It can be seen from the results in Tables (3.1) and (3.3) that measuring the concentration of the nebulizer reservoir solution at the end of each minute gives the best estimate of the average solution concentration in the droplets.

In a clinical setting, nebulizers are typically operated when there is not enough solution in the reservoir to continuously produce aerosol (i.e. the nebulizer operates intermittently or 'sputters'). It is therefore important to consider how the above results might be extrapolated to predict the concentration of the solution in the droplets produced when the nebulizer is sputtering. When the nebulizer is sputtering, the operation of the nebulizer is characterized by short periods where the nebulizer is running 'continuously', and periods when the nebulizer is not producing droplets. It has been reported by several authors (Mercer *et al.*, 1968, O'Callaghan *et al.*, 1989, Langford & Allen, 1993) that during the final period of the nebulization session, there was minimal drug output, but continued vapour water output by the nebulizers these authors tested. This is consistent with the loss of water directly from the nebulizer reservoir by evaporation during the periods when the nebulizer is not producing droplets. To account for this in the calculations, m_v in Equation (3.2) must include water losses due to this evaporation, or Equation (3.5) will underestimate the calculated average concentration in the droplets.

More important to calculations here is the effect that any evaporative losses during sputtering would have on the ability of the measurement of the nebulizer reservoir

solution concentration at the end of a minute to predict the average concentration of the droplets produced during that minute. It is reasonable to expect that any increase in concentration of the nebulizer reservoir solution when the nebulizer is not producing droplets will be at a rate equal to or lower than when the nebulizer is producing droplets, since the surface area available for evaporation is lower when the nebulizer is not producing droplets.

The evaporation rates of four PulmoNeb nebulizers were measured by blocking the flow of reservoir solution to the venturi to stop droplet production, and running the nebulizers for one hour. On average, 0.7818 ± 0.0034 g (mean \pm standard error) of liquid was lost over the hour, giving a rate of 0.0132 ± 0.0001 g/min. of liquid evaporating from the nebulizer solution, less than 5% of the rate of mass loss during droplet production. No solute was lost from the reservoir solution during the test period.

Estimating the effect that this evaporative loss will have on the calculated average solution concentration in the droplets is difficult since it is highly dependent on the performance of the nebulizer, and the length of time during which the nebulizer 'sputters'. Most studies of nebulizer performance end the nebulization session when there is a pause of 15 - 20 seconds in droplet output. We have chosen a pause of 15 seconds in the droplet output to signify the end of the nebulization session. Using this criterion, the PulmoNeb nebulizer sputters for less than 3 minutes before the nebulization session is stopped, and the total amount of time during the nebulization session that each PulmoNeb nebulizer did not produce droplets was between 1 minute, and 1 minute 15 seconds.

If we now consider an entire nebulization session that ends when there is a 15 second pause in droplet production, then the concentration of the reservoir solution at the end of each minute will accurately predict the average solution concentration in the droplets over the 1 minute time interval during the first part of the session when the nebulizer is continuously producing droplets. Near the end of the session when the nebulizer starts to sputter, the concentration of the reservoir solution may underestimate the average solution concentration in the droplets by up to 5-6% by the end of the nebulization session. The magnitude of this error will depend strongly on the performance of the nebulizer tested, particularly if the nebulizer sputters for a long time. However, it has been noted that most of the nebulizers tested in this lab sputter for shorter periods than the PulmoNeb, so the error can be expected to be less than the 5-6% estimated for the PulmoNeb.

3.3.3 Application to Vented Jet and Ultrasonic Nebulizers

The primary operational difference between normal jet and vented jet nebulizers is that on inhalation the patient draws air through the bowl of the nebulizer. This means that m_{in} in Equation (3.1) (the mass of water vapor entering the nebulizer during the time period t) is now the sum of the water vapor entering from the compressed air source and from the vent. Theoretically, m_{in} can be easily calculated from Equation (3.3) with Q equal to the inhalation flow rate of the patient. Then the rest of the theory is directly applicable to vented jet nebulizers.

However, this is not a practical method because the fluctuating flow rate through the droplet producing region of the nebulizer during the breathing cycle makes integration

of the mass losses by water vapour difficult. Here, for vented jet nebulizers, we assume that the concentration in the droplets is constant over the entire nebulization session. If the droplets are in equilibrium with the surrounding air, they can be collected during simulated tidal breathing on a Respiragard II filter (Marquest Medical Products Inc. Englewood, CO) placed between the nebulizer mouthpiece and the breathing simulator (see Figure 3.12) and their mass determined. (Because the droplets are in equilibrium with the surrounding air, they will not evaporate after depositing on the filter as the air passes through the filter from the simulated tidal breathing. The validity of this assumption was checked by additionally collecting the exhaled droplets, and accounting for all the mass of the system within 2%.) To determine the mass of solids collected on the filter, the filter was dried, treated with 5 ml of water, sonicated for 30 minutes, and the concentration of the remaining solution determined by freezing point osmometry (Precision Systems Inc., Natick MA). The average solution concentration was then determined by dividing the mass of solute by the total mass of liquids collected on the filter.

As with the unvented jet nebulizers, it is assumed that the droplets are in equilibrium with the surrounding air when they exit the mouthpiece of the nebulizer. To test this, a Pari LCJet+ nebulizer was driven by the same DeVilbiss Pulmo-Aide compressor as the unvented jet nebulizer tested above with a dry compressed air source (0% RH) line attached to the inlet vent on the nebulizer. Dry air was pumped through the nebulizer at 48 l/min, so that the flow rate of air exiting the nebulizer was 54 l/min (800 cm³/s), which is approximately equal to tidal breathing during light exercise (Rudolf *et al.* 1990).

The same lengths of tubes used with the unvented jet nebulizer considered previously were added to the exit of the vented nebulizer to allow up to 2 additional seconds for the droplets to come into equilibrium with the surrounding air. It was again found that there was no significant difference in the average size of the measurements (Student's t test, $P > 0.1$) or in the GSD (F test, $P > 0.1$) indicating that as for the unvented jet nebulizer, the droplets are in equilibrium with the surrounding air when they leave the nebulizer. In this experiment, dry air from a compressed air line was used instead of ambient air from the room to supply air to the nebulizer. If air from the room was used (e.g. RH = 34%), the droplets need to evaporate less to humidify the air, and they would come into equilibrium faster. The conclusion drawn from the experiment is unchanged.

The methodology presented in Section 3.3.2 was also adapted for a DeVilbiss Aerosonic[®] (Model 5000) ultrasonic nebulizer delivering single dose nebulized Ventolin[®] by Prokop *et al.* (1995a) who showed that the droplets are in equilibrium when they exit the nebulizer, although two distinct intervals in each breathing cycle can be identified by their differing MMDs and particle number concentration. Prokop *et al.* then modified Equations (3.1) - (3.5) to account for the noted variation in MMD and number density of the aerosol throughout the inhalation cycle. The reader is referred to Prokop *et al.* (1995a) for a detailed description of the modifications.

3.3.4 Calculation of Reservoir Solution Concentration for Unvented Jet Nebulizers

The above procedure for calculating the average concentration in droplets output by unvented jet nebulizers requires that a sample of the nebulizer reservoir solution be

extracted each minute. For a nebulizer that has a long run time, or for a nebulizer that has a very small volume of liquid in the reservoir at the end of the nebulization period, the extraction of this sample could significantly impact the measured performance of the nebulizer. In the above tests, this was avoided by using large volume fills, so the small amount of liquid extracted for concentration was not a significant portion of the total reservoir volume. However, when characterizing the output of nebulizers used in a clinical setting, it is important to use the volume fills typically used in clinical settings to correctly estimate the clinical performance. In this case, the procedure described above for calculating the solution concentration in the droplets may itself impact the results. To avoid these complications, a method of predicting the reservoir solution concentration during the nebulization session from a single measurement of the reservoir solution concentration at the end of the nebulization session is needed.

The concentration of solution in the reservoir of a nebulizer at time t is given by (Mercer, 1981):

$$\frac{c(t)}{c_0} = \left(\frac{V_0}{V_0 - (A + W)Q \cdot t} \right)^{\frac{W}{A+W}} \quad (3.11)$$

where c = solute concentration at time t

c_0 = initial solute concentration

V_0 = initial volume of liquid in the nebulizer

A = volume of droplets leaving the nebulizer per unit volume of air

W = volume of water vapor leaving the nebulizer per unit volume of air

Q = air flow rate through the nebulizer

The factor $V_0 - (A + W)Q \cdot t$, is simply the residual volume of the reservoir solution at time t and can be easily measured by weighing the nebulizer. As can be seen in Figure 3.10, the agreement between the measured values of the reservoir solution concentration and the values predicted by Equation (3.11) are excellent.

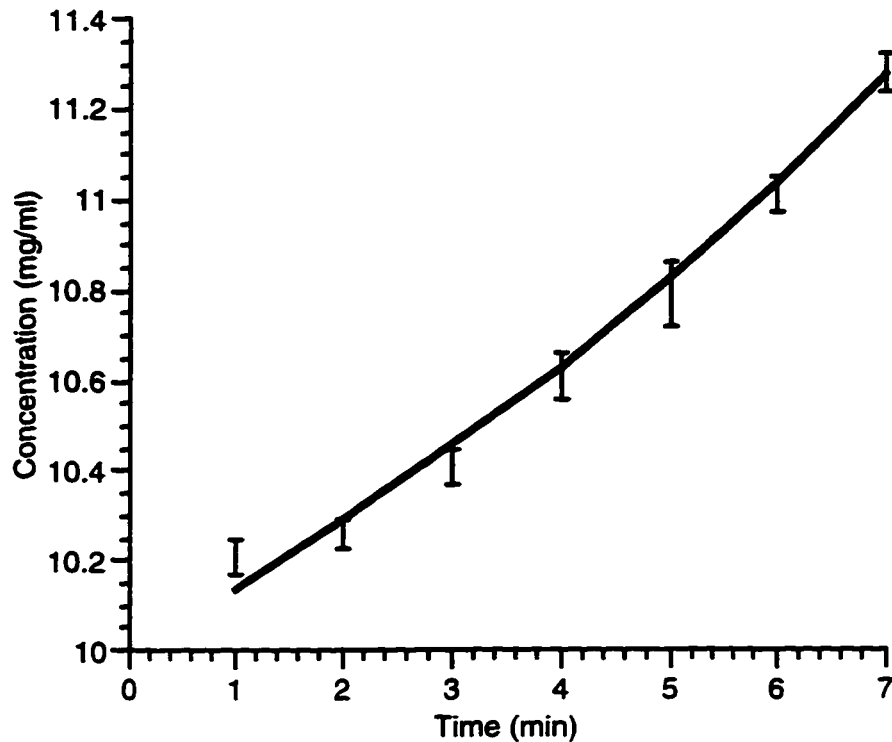


Figure 3.10. Measured concentration of the reservoir solution for 8 PulmoNeb disposable nebulizers given in Table 3.1 and the values predicted by Equation (3.11). Error bars indicate standard error of the measurements.

3.3.5 Miscellaneous issues

There are a number of issues that need to be addressed before a nebulizer can be tested with this methodology. First, it must be determined if the droplets are in equilibrium with the surrounding air when they exit the nebulizer using the procedure described in Section 3.3. If the droplets are not in equilibrium when they exit the nebulizer, then this methodology is not directly applicable.

To characterize the output of the nebulizer accurately, the size distribution, and the number of droplets per second exiting the nebulizer are required. Since the PDA system used here only measures the droplets over a small measuring volume (typically

10^{-3} mm^3) the size distribution of the entire output must be determined from values measured at a series of locations.

To determine the number of such measurement locations required, the variation of nebulizer output across the nebulizer opening was investigated by measuring the droplet size distribution at 2 mm intervals across the exit of a PulmoNeb nebulizer without a mouthpiece (inside diameter of exit tube = 18.7 mm). The measured distributions were tested for similarity using the same procedure used in Section 3.3.2.1 to determine if the droplets are in equilibrium when they exit the nebulizer. No significant change was found in the MMD or GSD of the droplet distribution as the measuring volume was moved across the interior of the opening. However, when the measuring volume was directly over the edge of the opening, there was a slight decrease in the measured MMD, which may be due to shrinkage of droplets caused by the entrainment of ambient air by the plume exiting the nebulizer. Additionally, the number of droplets counted by the PDA varied monotonically by approximately 16% over the nebulizer opening, with the minimum recorded when most of the aerosol cloud was between the measuring volume and the sensing optics. This may be due to rescattering of the refracted light by other droplets, since rotating the nebulizer had no effect on the results.

As long as the measuring point was inside the opening of the nebulizer, and the measuring point was no more than 0.5 cm from the top of the opening, the measurement of the MMD and GSD of the droplet distribution was found to be independent of the location of the measuring volume with respect to the opening of the nebulizer. The measuring point was chosen to be as close to the center of the opening and to the top of the nebulizer as possible to minimize any possible droplet shrinkage from the entrainment

of ambient air. Correction for the droplets not counted due to the optical depth of the cloud was done by a mass balance, and will be described in Section 3.4.1.1.

The humidity and temperature of the air available to the compressor were controlled by placing the compressor in a chamber, described by Prokop *et al.* (1995b), in which dried air was mixed with saturated air to obtain a continuous supply of air of 50% RH, and 23°C. Temperature and relative humidity were measured with a thermometer and hygrometer (Fisher Scientific, Ottawa, ON) respectively, placed in the chamber.

3.4 Calculation of Regional Dosage

We now possess the tools to predict the regional dosage delivered from a nebulizer to different parts of the lung. The first step in this procedure requires a series of bench-top measurements that characterize the output of the nebulizer. Next, this information is input into a computer program which first processes the data into a form usable by the deposition model described in the previous chapter. The computer program then uses the deposition model to calculate the probability of the aerosol droplets depositing in different generations of a Weibel 'A' lung scaled to a total lung capacity of 3000 cm³. Finally, the program converts the deposition probabilities to regional dosages for the extrathoracic, bronchial, and alveolar regions of the lung, and outputs the results. This section describes which measurements are taken on the bench, and overviews how the computer program calculates the regional dosages from the given data. A flowchart of the program is given in Figure 3.11, and the data files are listed in Appendix A (input files) and Appendix B (output files).

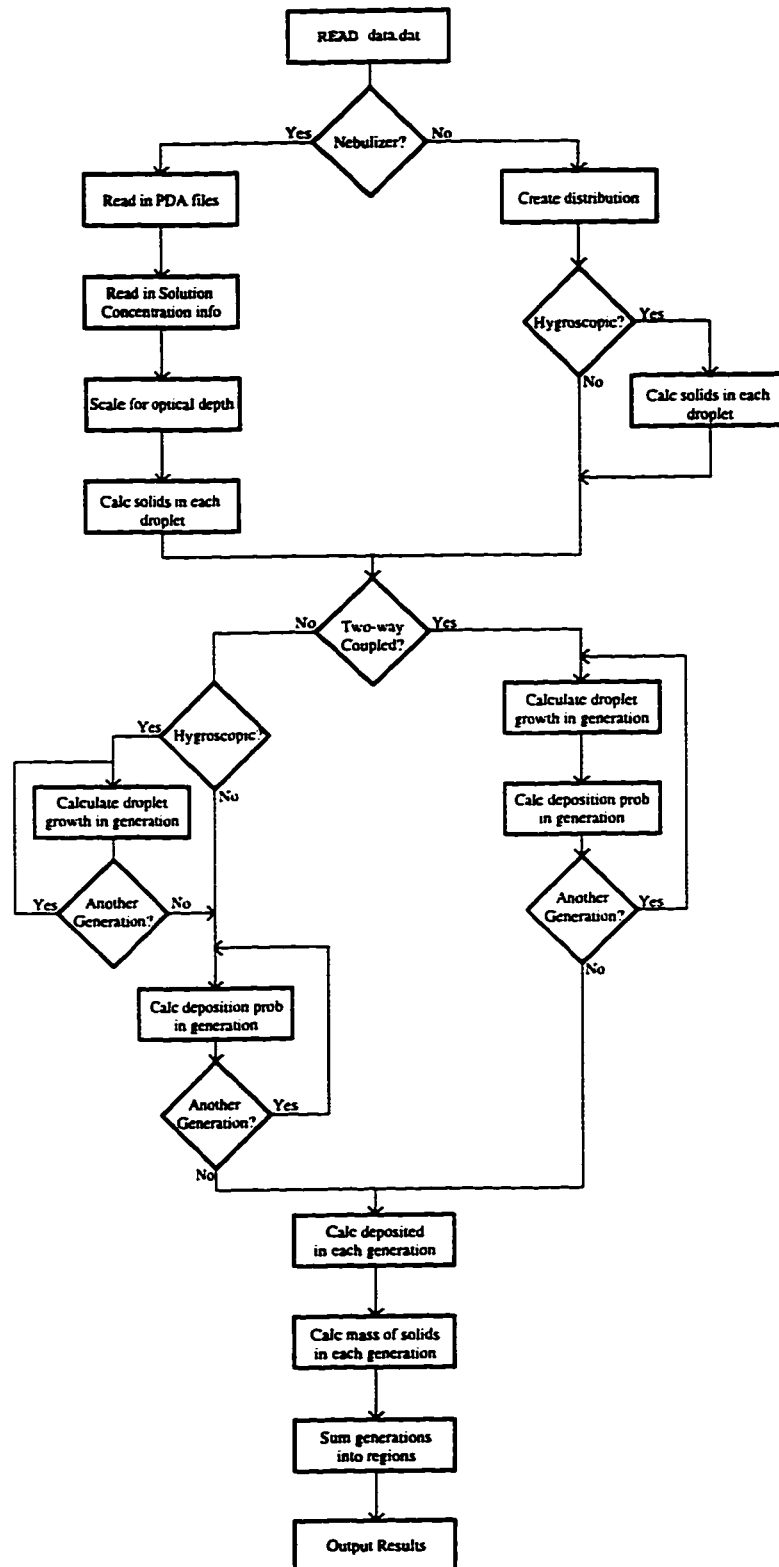


Figure 3.11. A flowchart for the program to calculate the dosage delivered to different regions of the respiratory tract.

As an example of an unvented jet nebulizer, this methodology will be applied to the Hudson T Updraft II nebulizer (Model 1732, Hudson RCI, Temecula, CA) driven by a DeVilbiss Pulmo-Aide compressor delivering a single unit dose nebule of Ventolin®. The modifications to the procedure needed to predict the regional dosage from a vented jet nebulizer will also be discussed. Primarily, these modifications are in the bench measurements and the preprocessing of the data, since the hygroscopic growth calculations, the calculation of the deposition probabilities, and the calculation of the dosages are the same. As an example of a vented jet nebulizer, this methodology will be applied to a Pari LCJet+ nebulizer (Pari GmbH, Starnberg, Germany) driven by the same compressor, and delivering the same drug. Modifications necessary for predicting the regional dosages from one particular ultrasonic nebulizer were discussed by Prokop *et al.* (1995a), and the reader is referred there for details.

3.4.1.1 Unvented Jet Nebulizers

Six Hudson T Updraft II nebulizers were tested to give a statistical sample of nebulizer performance. The nebulizer was weighed before and after the addition of the solution to be nebulized. The nebulizer was then run for 1 minute using the compressor in the controlled humidity and temperature chamber, during which time the droplet distribution was measured with the PDA. At the end of the minute, the nebulizer was reweighed. This constitutes the data for the first minute of nebulizer operation. The second minute of data was collected by running the nebulizer for an additional minute, during which time a measurement of the size distribution was taken with the PDA. The nebulizer was then reweighed at the end of the minute. This procedure was repeated until there was a period of 15 seconds occurred during which no droplets were produced by the

Data Minute	Nebulized Mass (g)	Concentration (mg/ml)
1	0.189±0.024	
2	0.193±0.025	
3	0.197±0.025	
4	0.206±0.015	
5	0.189±0.011	
6	0.182±0.012	
7	0.177±0.019	
8	0.146±0.021	
9	0.117±0.022	
10	0.090±0.022	
11	0.079±0.017	1.23±0.04
Total	1.76±0.07 (70.4%)	

Table 3.4. Total mass leaving the nebulizer during each minute, and the final concentration of solids (salbutamol sulfate and NaCl) in the nebulizer solution at the end of the nebulization period. All values are mean ± standard error. The value in parentheses indicates the nebulized mass as a percentage of the initial mass of solution in the nebulizer

nebulizer. At the end of the nebulization session, the nebulizer was weighed a final time, and a sample of the reservoir solution was removed for concentration assay.

Table 3.4 gives average results of the measurements just described. The droplet size distribution was essentially lognormal with a mass median diameter (MMD) of 5.57 ± 0.16 μm and a geometric standard deviation (GSD) of 1.95 ± 0.10 . The average run time for the nebulizers was 10.6 ± 0.2 minutes, and is rounded up to 11 minutes for presentation purposes.

Many of the parameters commonly used to characterize the performance of nebulizers can be calculated from this data. For example, the efficiency of the nebulizer is defined as the amount of drug that leaves the nebulizer as an aerosol divided by the initial amount of drug in the nebulizer, and can be calculated to be 63.6% here (using the average values). If the size distribution is assumed to be perfectly log normal, then the respirable fraction (fraction of mass contained in droplets between 1 μm and 6 μm) can be calculated to be 0.56. The delivered respirable fraction is defined as the product of the efficiency and the respirable fraction, and can be calculated to be 35.5%.

Cipolla *et al.* studied the performance of the T-Updraft II for delivering RhdNase and found a similar respirable fraction of 50.5%, a lower efficiency of 46.4%, yielding a delivered respirable fraction of 23.4%. Additionally, Loffert *et al.* (1994) studied the T-Updraft II and measured an efficiency of 64.8% and a delivered fraction of 40.1%. No respirable fraction is reported, but a value of approximately 62% can be inferred.

However, these performance measures may not provide an accurate representation of the ability of the nebulizer to deliver drug to the respiratory tract as the hygroscopic nature of the droplets is not accounted for, and the filtering capabilities of the respiratory tract are only crudely estimated by the respirable fraction. Most importantly, for an unvented jet nebulizer used with equal inhalation and exhalation period, half of the inhalable aerosol will be lost to the atmosphere during exhalation, and is not available for inhalation. An in depth discussion of these points is provided by Finlay *et al.* (1997b).

3.4.1.2 Computer Calculations of Regional Dosage

The computer program to calculate the dosages delivered to the three regions of the lungs (extrathoracic, bronchial, and alveolar) is written in FORTRAN and runs on the

IBM RS/6000 family of engineering workstations. This section will describe the necessary input, and outline the calculation procedure.

Three data files are required in addition to the size distribution files from the PDA system. The first file contains the names of the PDA size distribution files. The second data file contains the mass lost during each minute of nebulizer operation, and the concentration of the reservoir solution at the end of the nebulization period. The third data file contains all other required data, as well as the flags for computation options within the code. The reader is referred to Appendix A for a listing of the input files, and a detailed description of the input fields.

Once all data files are read in, the number of droplets exiting the nebulizer in each minute is calculated from the number densities measured by the PDA system and corrected to match the mass lost as a liquid from Equation (3.2). This correction accounts for any droplets not counted due to the optical depth of the cloud. To illustrate how the correction is calculated, consider the n th minute of data for the Hudson T Updraft II. The average size distribution measured during the n th minute of data collection is integrated to calculate the total mass contained in the droplets. The correction for the n th minute is defined as:

$$corr_n = \frac{m_{l,n}}{m_{int,n}} \quad (3.11)$$

where $m_{l,n}$ is the mass lost as liquid in the n th minute, and $m_{int,n}$ is the mass obtained by integrating the size distribution for the n th minute. The number of droplets in each size class is then multiplied by $corr$, to obtain the corrected distribution.

Next, Equation (3.11) is used to calculate the reservoir solution concentration at the end of each minute, or equivalently, the average solution concentration of the droplets during each minute. Multiplying the average solution concentration by the volume of the average particle size for the class gives the average amount of solid in each droplet in the class. This is important since regardless of the hygroscopic growth of the droplet, the amount of solute contained in the droplet is assumed to be constant during its transit through the respiratory tract.

In an unvented jet nebulizer, ambient air is entrained in the mouthpiece to make up the difference between the output flow rate of the nebulizer and the inhalation flow rate of the patient. Here, the aerosol from the nebulizer and the entrained air are assumed to mix instantly, diluting the number density of the aerosol. The heat and water vapour content of the ambient air, and the cooled aerosol from the nebulizer are combined to calculate the temperature and relative humidity of the inhaled air. The droplets are given an initial temperature equal to that of the aerosol exiting the nebulizer.

The next step in the program is the calculation of the droplet growth, and the calculation of the deposition probabilities in each region of the lung model. In each size class, the droplets are assumed to be the same size, and each size class is effectively treated as a monodisperse aerosol. Inclusion of polydispersity in the hygroscopic growth calculations is discussed in Section 2.5.2. Two-way coupled heat and mass transfer is used in the calculations here unless otherwise stated. One-way coupling is available as an option, as is the assumption of inert particles.

The deposition probabilities are calculated using the average size of each particle class in the generation. The deposition model calculates the probability that an inhaled

droplet will deposit in a specific generation. To convert this to a dosage, the total number of inhaled droplets is required.

In an unvented jet nebulizer, the drug inhaled per minute can be determined from the total number density of droplets in each class present in the inhaled air, by the inhalation flow rate, and the total number of seconds per minute occupied by inhalation. For example, it has been suggested that an average breathing cycle consists of a 1.74 second inhalation, 0.2 second inspiratory pause, and a 2.06 second exhalation for a total breathing cycle of 4.0 seconds (ICRP, 1994). In this case, the distribution would be multiplied by 26.1 sec to obtain the number of inhaled droplets in each size class in each minute. Here, for simplicity, we assume equal inspiratory and expiratory times (so the distribution is multiplied by 30.0 sec).

Because of the extremely large number of inhaled droplets in each class, the probability that a droplet will deposit in a generation can be interpreted as the percentage of inhaled droplets depositing in the generation. (The number of inhaled droplets per minute in each particle size class is often $O(10^8)$, while the smallest deposition probabilities are $O(10^{-4})$, so we can expect $O(10^4)$ droplets to deposit in a generation.) Multiplying this percentage by the number of inhaled droplets calculated above gives the number of droplets in each size class that deposit in each generation. Since we know the amount of solids that each droplet contains, the number of droplets deposited in each generation can be easily converted to the mass deposited in each generation, and the dosage of drug delivered to each generation can be determined.

Summing the dose delivered to generations 3 through 19 gives the predicted dosage delivered to the bronchial airways, while the dose delivered to generations 20

through 26 is the predicted alveolar dosage. Total predicted lung dosage is the sum of the bronchial and alveolar dosages. The intersubject variability intervals are converted to dosages in the same way as the mean probabilities.

3.4.1.3 Results

From an initial 2.5 ml nebulizer of Ventolin® (1 mg/ml salbutamol sulphate), the Hudson T-Updraft II® disposable nebulizer delivered, on average, 0.246 ± 0.017 mg ($9.8 \pm 0.7\%$ of the nominal dose) of Ventolin® to the extrathoracic region, 0.279 ± 0.11 mg ($11.5 \pm 0.5\%$ of the nominal dose) to the bronchial airways, and 0.173 ± 0.005 mg ($4.9 \pm 0.3\%$ of the nominal dose) to the alveolar airways. Total lung deposition was 0.402 ± 0.013 mg ($16.1 \pm 0.5\%$ of the nominal dose). The number density of the aerosol was $(2.3 \pm 0.2) \times 10^5$ droplets per cm^3 , indicating that two-way coupling should be used to correctly account for hygroscopic effects. Dosages are for an average Caucasian male breathing with a tidal volume of 0.75 liters and with an inhalation flow rate of $300 \text{ cm}^3/\text{s}$. Ambient conditions for the test were 50% RH, and 23°C .

Region	% of Nominal Dose Delivered	68% Confidence interval
Extrathoracic	9.8 ± 0.7	5.2 - 14.5%
Bronchial	11.2 ± 0.5	7.1 - 15.2%
Alveolar	4.9 ± 0.3	3.4 - 6.4%
Total Lung	16.1 ± 0.5	11.8 - 20.4%

Table 3.5. Regional dosage of Ventolin® delivered to the respiratory tract by the Hudson T Updraft II nebulizer as a percentage of the nominal dose in the nebulizer. Individual dosage for 68% of the population would fall within the given ranges. Calculations are for a tidal volume of 0.75 liters, and an inhalation flow rate of $300 \text{ cm}^3/\text{s}$.

3.4.2 Vented Jet Nebulizers

As with the unvented nebulizers, it was first determined that the droplets were in equilibrium with the air exiting the Pari LC+ nebulizer. This was done using the procedure described in Section 3.3 with 12 l/min of dry air supplied to the vent of the nebulizer so that the flow out the mouthpiece equaled the 300 cm³/s that would be used as the inhalation flow rate in the experiments. It was found that the droplets were in equilibrium at the exit of the nebulizer.

Vented jet nebulizers require a significantly different experimental setup than unvented nebulizers due to the different operating principal. First, both the relative humidity and temperature of the air supplied to the compressor and the vent must be controlled, and be the same. This is done by placing the nebulizer in the same humidity control chamber as the compressor. The mouthpiece of the nebulizer protrudes through the side of the chamber and is connected to a measuring chamber to allow the measurement of the droplet sizes by the PDA system while the inhaled aerosol is being collected on the filters. The chamber consists of two optically clear lenses oriented perpendicularly to the axes of the transmitting and receiving optics of the PDA system and an airtight volume (see Prokop *et al.* 1995 for a detailed description). It was determined that the measuring volume had no affect on the droplet size measurements by measuring the size of polystyrene spheres of diameters 1.5 µm, 2.5 µm, and 6.0 µm. In each case, the measured size of the spheres was within the 4% error of the PDA system. The measuring volume was connected to a cellulose filter to collect the inhaled aerosol, which was connected to the breathing simulator. See Figure 3.12 for a schematic of the experimental setup

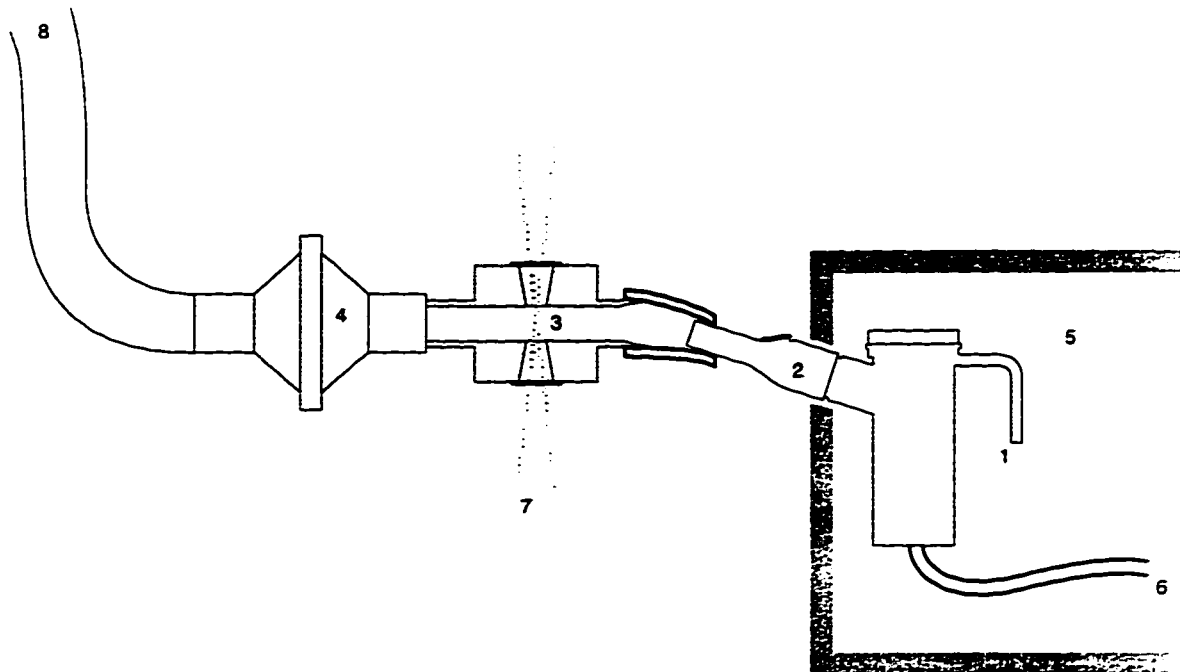


Figure 3.12. A schematic of the experimental setup for a vented jet nebulizer. The nebulizer and mouthpiece (1) and compressor are placed in a chamber (5) with controlled temperature and relative humidity. The nebulizer is attached via hosing to a measuring volume (3) where the size distribution is measured with the PDA (laser beams, 7). The measuring volume is connected via hosing (4) to the breathing simulator

Because aerosol is drawn through the droplet producing region of a vented jet nebulizer, and the output rate of the nebulizer may be dependent on the inhalation flow rate, patient breathing should be simulated to obtain meaningful results. This is done using a computer controlled stepper motor driving a piston connected via hosing to the filter. The in-house motor controller software allows a wide range of breathing patterns, flow rates, and tidal volumes. For these tests, a square wave breathing pattern was used with equal inspiratory and expiratory times and no inhalation or exhalation pause. The tidal volume was set to 0.75 liters, and the inhalation flow rate to $300 \text{ cm}^3/\text{s}$.

3.4.2.1 Bench Measurements

Ten Pari LC + nebulizers were tested to give a statistical sample of nebulizer performance. The nebulizers are weighed before and after the addition of the solution to be nebulized. Additionally, the filter and integral holder were weighed before testing. Each nebulizer was then placed in the humidity chamber and connected to the measuring volume. The breathing simulator and the compressor were started simultaneously, and the nebulizer was run until a 15-second pause in output was noted. Size measurements of the inhaled aerosol were taken at one-minute intervals. At the end of the nebulization session, the nebulizer was reweighed, and a sample of the remaining reservoir solution was removed for concentration analysis by freezing point osmometry. The filter was then weighed, and the amount of solids collected determined by the procedure described in Section 3.3.3.

An additional concern in this methodology is the connection volume between the mouthpiece and the filter. If this volume is a significant percentage of the tidal volume, then the mass of droplets collected on the filter will not be an accurate measurement of the droplets actually inhaled. To correct for this, the masses collected on the filter are multiplied by a scaling factor defined as:

$$scale = \frac{V_T}{V_T - V_{cv}} \quad (3.13)$$

where V_T is the tidal volume, and V_{cv} is the connection volume. The connection volume was measured to be 102 cm³, so the scaling factor is 1.157 for the 0.75 liter tidal volume used here.

After correction for the connection volume, the average mass collected on the filters was 0.386 ± 0.012 g, and the average mass of solids collected on the filter was 5.55 ± 0.18 mg. The average MMD of the aerosol was 5.91 ± 0.09 μm , and the GSD was measured at 1.72 ± 0.01 . The average mass lost during the nebulization session was 1.27 ± 0.04 g, and the average concentration of the reservoir solution was 1.21 ± 0.02 mg/ml. A respirable fraction of 52% can be calculated from the size distribution as for unvented nebulizers. However, because the mass collected on the filters is only inhaled mass, a nebulizer efficiency and delivered respirable fraction cannot be compared directly with those calculated for the Hudson T-Updraft II.

3.4.2.2 Calculation of Regional Dosages

After reading in the data files, the aerosol size distributions measured at one minute intervals during the nebulization session are averaged to obtain an average distribution for the entire session (It was found that the MMD and GSD of the aerosol changes very little during the nebulization session). The averaged distribution is then integrated and scaled as described in Section 3.4.1.3 with the total inhaled mass collected on the filter to calculate the total number of droplets inhaled during the nebulization session. The total mass of inhaled solids is then distributed through the droplets so that each droplet has the same concentration (this is justified by knowing that the droplets are in equilibrium when they exit the nebulizer, therefore they all have the same solution concentration). After this, the procedure to calculate the regional dosages is the same as for unvented jet nebulizers.

3.4.2.3 Results

On average, the Pari LC+ nebulizer delivered an estimated 0.498 ± 0.008 mg ($19.9 \pm 0.3\%$ of the nominal dose) of Ventolin® to the respiratory tract from an initial 2.5 ml nebule (1 mg/ml salbutamol sulphate). The estimated dose was distributed as follows: 0.172 ± 0.005 mg ($6.9 \pm 0.2\%$) to the extrathoracic region, 0.236 ± 0.006 ($9.4 \pm 0.2\%$) to the bronchial region, and 0.090 ± 0.003 ($3.6 \pm 0.1\%$) to the alveolar region. These estimated dosages and the estimated intersubject variability ranges are given in Table 3.6. The number density of the aerosol was $(8.8 \pm 0.3) \times 10^5$ droplets/cm³. Deposition is for an average Caucasian male breathing with a tidal volume of 0.75 liters and with an inhalation flow rate of 300 cm³/s. Figure 3.13 compares the output of the Pari LC+ and the Hudson T Updraft II.

Region	% of Nominal Dose Delivered	68% Confidence interval
Extrathoracic	6.89 ± 0.2	4.0 - 9.81%
Bronchial	9.44 ± 0.2	5.88 - 13.0%
Alveolar	3.59 ± 0.1	2.35 - 4.83%
Total Lung	13.03 ± 0.3	9.26 - 16.8%

Table 3.6. Predicted regional dosage of Ventolin® delivered to the respiratory tract by the Pari LC+ nebulizer as a percentage of the nominal dose in the nebulizer. The 68% confidence interval indicates the range within which estimated dosages for 68% of the population would fall. Calculations are for a tidal volume of 0.75 liters, and an inhalation flow rate of 300 cm³/s.

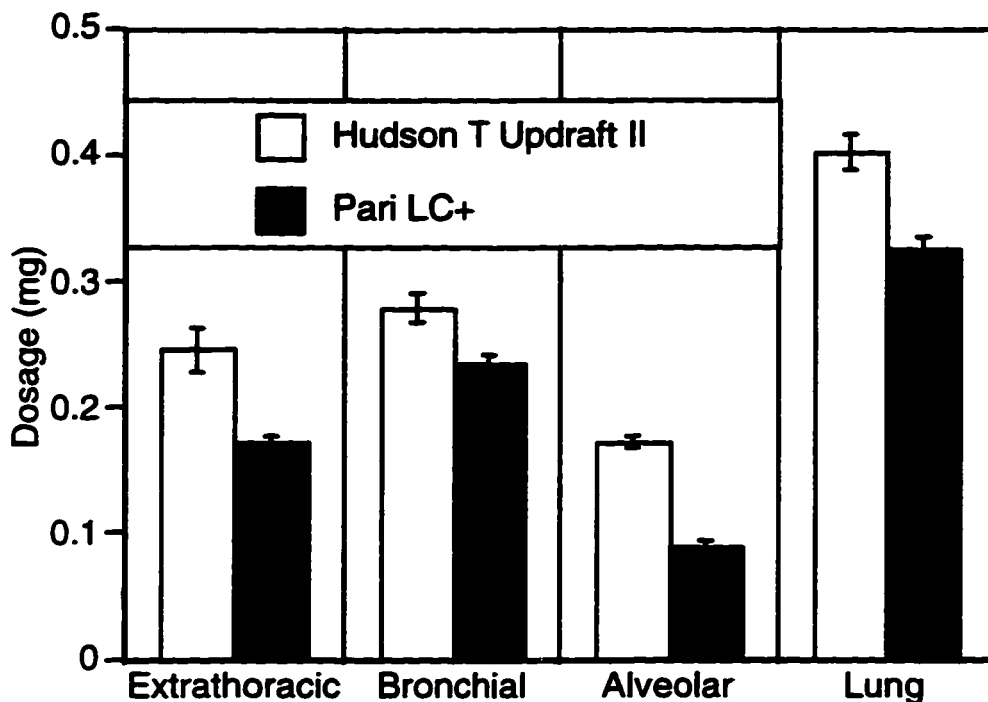


Figure 3.13. The regional dose delivered by the Hudson T Updraft II and the Pari LC+ nebulizers. Test conditions were 50% RH, 23°C. Dosages are for an average Caucasian male with an inhalation flow rate of 300 cm³/s and a tidal volume of 0.75 liters. Error bars on the graph indicate the standard error in the measurements.

3.4.3 The Effect of Tapping

Tapping the side of the nebulizer during operation promotes the return of nebulizer solution attached to the sides of the nebulizer by surface tension (in the form of drops), to the reservoir for renebulization. This is particularly important during the final phase of the nebulization session when the nebulizer is sputtering. Stapleton *et al.* (1994) predicted the regional dosage delivered by the PulmoNeb® disposable nebulizer with the above procedure with two protocols: first with no tapping, and the second where the nebulizers were tapped with a finger on the side of the nebulizer at a rate of approximately 4 taps per second whenever the nebulizer was not outputting aerosol.

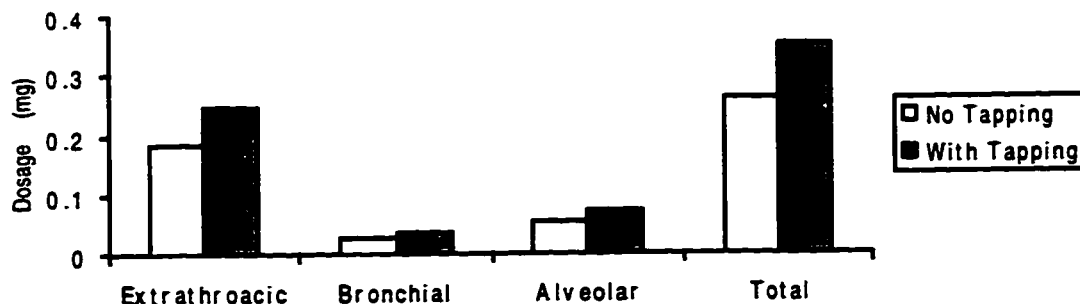


Figure 3.14. The effect of tapping the nebulizer at a rate of approximately 4 taps per second during the nebulization session. The total dosage delivered to the respiratory tract increased from 0.261 ± 0.005 mg ($10.4 \pm 0.2\%$ of nominal dose) to 0.352 ± 0.006 mg ($14.1 \pm 0.2\%$ of nominal dose), an increase of 35%. The regional distribution of the dose did not change. The inhalation flow rate was $300 \text{ cm}^3/\text{s}$ tidal volume 0.75 liters, and ambient conditions were 23°C and 26% RH. All values mean \pm standard error.

They found that the nebulization session increased from 4 to 6 minutes, and that the mass output by the nebulizers increased by 35%.

When the tapping protocol was used, the estimated dose of Ventolin[®] delivered to the respiratory tract increased from 0.261 ± 0.2 mg (10.4% of the nominal dose) to 0.352 ± 0.006 mg (14.1% of the nominal dose), an increase of 35% over the estimated dosage delivered when no tapping was used. Note, however, that the relative regional distribution of the estimated dosage is not changed.

3.4.4 Effect of different treatments of hygroscopic growth

The hygroscopic growth calculations can be performed assuming either two-way or one-way coupling between the droplets and the surrounding air, or by assuming that the droplets do not change size. Finlay & Stapleton (1995) showed that for polydisperse aerosols typical of those produced by nebulizers, differences in the calculated dosages for the three calculation modes can be as high as 137%. In the tests discussed above, the

Hudson T Updraft II produced an aerosol with approximately 2.3×10^5 inhaled droplets/cm³, and the Pari LC+ produced an aerosol with approximately 8.8×10^5 inhaled droplets/cm³. Both of these are in the range in which Finlay & Stapleton suggest two-way coupling should be used. However, because of the added expense of two-way calculations, it is useful to consider how the different hygroscopic treatments might affect the regional dosages for the nebulizers here.

As can be seen in Table 3.7, using one-way coupling to calculate the hygroscopic growth of the droplets results in a decrease in the predicted extrathoracic deposition and an increase in the predicted alveolar deposition. For the Hudson T-Updraft II, the difference in the predicted extrathoracic deposition between two-way and one-way coupling is approximately 40%, and for the Pari LC+ it is approximately 30%. The differences between the predicted alveolar dosages 53% and 47% respectively, and the differences between the predicted bronchial dosages are approximately 13% and 6% respectively. For the two nebulizers considered here, one-way coupling in the hygroscopic growth calculations will lead to significant errors in the estimated regional dosages.

In the case of the Pair LC+, assuming inert particles is superior to 1-way coupling, resulting in differences of less than 5% for all estimated dosages between two-way coupling and inert particles. For the Hudson T-Updraft II, the difference in the estimated dosage between two-way coupling and inert particles is as high as 15%, still significantly less than the difference between one-way and two-way coupling. The cause of this effect is that the high number densities of the aerosol are likely buffering the hygroscopic

Nebulizer	Region	2-way coupling	1-way coupling	Inert particles
Hudson T Updraft II	Extrathoracic	9.8±0.7	7.0±0.6	10.6±0.7
	Bronchial	11.2±0.5	9.9±0.4	11.4±0.4
	Alveolar	4.9±0.2	7.5±0.4	4.2±0.2
	Total Lung	16.1±0.5	17.4±0.5	15.7±0.4
Pari LC+	Extrathoracic	6.8±0.2	5.2±0.4	6.6±0.3
	Bronchial	9.4±0.2	8.9±0.3	9.3±0.2
	Alveolar	3.6±0.1	5.3±0.3	3.8±0.2
	Total Lung	13.0±0.3	14.2±0.4	13.1±0.3

Table 3.7. The percent of the nominal dose put in the nebulizer delivered to different regions of the respiratory tract calculated with three different treatments of the hygroscopic growth calculations. Predicted total lung deposition is the sum of alveolar and bronchial deposition. All values are mean ± standard error.

growth of the droplets. It is important to note that this may not be the case with all nebulizers.

Recently, Finlay *et al.* (1997c) studied the effect of the different treatments of the hygroscopic effects on the deposition of aerosol from 7 different nebulizers. They found that at ambient humidities of approximately 90%, two-way coupling, one-way coupling, and neglecting hygroscopic growth entirely all gave similar results. At lower ambient humidities, they found errors up to 65% occurred by using a one-way coupled model. These results are consistent with those found here.

3.5 Comparison with other methodologies

To the author's knowledge, there are no other published models for predicting the regional dosage of nebulized drug delivered to the respiratory tract. Other models for

calculating the regional deposition probabilities of inhaled particles were discussed throughout Section 2. Methods for characterizing the performance of nebulizers were briefly discussed above, and by Finlay *et al.* (1997b).

As was discussed briefly in Section 3.3.2.1, Ferron *et al.* (1997) investigated the stability of aqueous droplets produced by jet nebulizers using a hygroscopic growth model similar in some ways to that presented here. While the benchtop data collected from the nebulizers is also similar, hygroscopic growth model is quite different from that presented here. It is useful to compare the two methodologies in some detail.

Briefly, Ferron *et al.* measure m_{out} , the total mass output of the nebulizer, and m_s , the total mass of solids leaving the nebulizer by weighing the nebulizer, and measuring the solids output over the nebulization session (e.g. by collecting the dried solids on a filter). Next, the mass of liquid in the droplets immediately after creation is calculated by dividing m_s by the initial concentration of the nebulizer reservoir solution. Any additional mass lost from the nebulizer is assumed to have evaporated from droplets that impact on the walls of the nebulizer that have returned to the reservoir. The water vapour which evaporates from droplets returning to the nebulizer is assumed to instantly mix with the air at the venturi and this provides the initial water vapour content of the air for the calculations. The size distribution of the droplets immediately after creation is assumed to be either a distribution measured at the exit of the nebulizer, or is calculated by drying the droplets, measuring the distribution of the dry particles, and inferring an initial size based on a growth factor (the dry residual method, see e.g. Sterk *et al.* 1984). The temperature of the air and the droplets are assumed to be constant and equal to ambient conditions. (This assumption is in error, as will be discussed shortly). From

these initial conditions, the growth of the droplets is calculated using a methodology similar to the one-way coupled model described here, with the difference that after each time step, any mass gained/lost by the droplets is subtracted/added to the water vapour content of the surrounding air.

Ferron *et al.* present calculations for the DeVilbiss PulmoNeb[®] tested here, and indicate that the aerosol is relatively stable after only 0.1 second, less than the average residence time of 0.5 seconds for a droplet in the nebulizer, and supporting the conclusion presented here that the droplets are in equilibrium when exiting the nebulizer. However, Ferron *et al.* suggest that this is not the case for other nebulizers, which differs from the suggestion of the results presented here, and from experience with other nebulizers in our laboratory. Possible sources for the discrepancy can be seen by comparing the details of each method.

The differences between the methods are subtle, yet important. First, in the methodology presented here, the growth calculations are begun after the droplets exit the nebulizer, while Ferron *et al.* begin the calculations immediately after droplet creation. While the size distribution of the droplets can be easily measured at the exit of the nebulizer and their concentration calculated by the procedure detailed in Section 3.3, the distribution at the creation point must be assumed or indirectly calculated. This adds another source of uncertainty to the accuracy of the size distribution beyond those associated with the measurement method, and neglects any change in the solute content of the droplets. (It is well known that the concentration of the reservoir solution increases with time, and often this increase is as high as 50% above the initial concentration. Using a constant growth factor, this could have two effects: first, the size distribution of the

droplets produced at the end of the nebulization session will be overestimated, and second, if the solute particles are collected over an entire nebulization session, the GSD of the distribution may be overestimated.)

Secondly, and more importantly, Ferron *et al.* neglect the cooling of the reservoir solution and the output air. At the end of one minute of operation, the temperature of the air exiting the PulmoNeb nebulizer is 3 °C below ambient, so the initial water vapour concentration calculated by Ferron *et al.* corresponds to 95% relative humidity, compared to the 80% calculated using ambient temperature. After two minutes of operation, the temperature of the air exiting the nebulizer has dropped another degree, and the calculated relative humidity is now over 100%, which according to the method of Ferron *et al.* indicates that the droplets should no longer shrink, and therefore the concentration of the solution in the nebulizer should no longer increase. This is not the case, as can be seen in Table 3.1, where the concentration continues to increase for 7 minutes. The temperature profiles for the other nebulizers used by Ferron *et al.* are not known, although it is common for the output air to drop 5 to 10 degrees C in less than 2 minutes (Phipps & Gonda, 1990). In general, the initial conditions used by Ferron *et al.* are only representative of the first few seconds of nebulizer operation, but are not representative of an entire nebulization session.

The third difference is in the treatment of the coupling between the droplets and the surrounding phase. For one-way coupled calculations, the equations used by both methods are similar and only differ in their treatment of the vapour pressure reduction at the droplet surface due to dissolved solids (Ferron *et al.* assume dilute solutions and use Raoult's Law; here, a nonlinear equation for NaCl is used), and the treatment of some

	Ferron et al. (1997)	This Model	Ferron et al. (1997)	This Model
Time	0.1 sec	0.1 sec	3.0 sec	3.0 sec
Salt MMD	2.2 μm	2.68 μm	2.15 μm	2.65 μm
Salt GSD	2.87	2.56	2.44	2.55
Mass MMD	3.6 μm	3.03 μm	2.45 μm	3.00 μm
Mass GSD	2.3	2.27	2.53	2.26
Final Temperature	20°C	16 °C	20°C	16°C
Relative Humidity	87%	99.5%	99.1%	99.5%
Water vap. conc.	15 $\mu\text{l/ml}$	13 $\mu\text{l/ml}$	17 $\mu\text{l/ml}$	13 $\mu\text{l/ml}$

Table 3.8. Comparison of the results of Ferron *et al* (1997) Figures 6 & 7 to the model presented here for an aerosol with an MMD of 2.8 μm and a GSD of 2.3. Results from our model for the droplet growth 30 seconds after creation differ in the 5th significant digit from those at 3.0 seconds and are not presented.

parameters such as the diffusion coefficients (Ferron *et al.* assume constant values, while values which change with temperature are used here). These differences have been found to have minor effects on the growth rates (Stapleton *et al.* 1995).

However, for two-way coupled calculations, the treatment differs dramatically. Ferron *et al.* assumes quasi-steady droplet growth, and calculate the mass added to the surrounding phase from the evaporation of the droplets. A similar process could be applied to the temperature of the surrounding phase, although in this specific instance, Ferron *et al.* assume that the temperature of the droplets and the surrounding air is constant and equal to the ambient temperature. The treatment of the coupling of the heat and mass transport between the continuous phase and the droplets is inconsistent since it assumes that mass transfer can occur between the droplets and the continuous phase

without heat transfer. Using this explicit scheme, the mass flow from each particle size class remains uncoupled from the others and can be calculated individually. In the model presented here, the droplet growth equations for all particle size classes remain coupled, and an implicit method is used to solve for all the droplet growth rates, droplet temperature, and the temperature and humidity of the surrounding phase simultaneously.

It is useful to compare the two models using the same initial conditions. To do so, the data from the Pari IS-2 nebulizer given by Ferron *et al.* will be used since it shows the greatest variation in the aerosol properties. The initial conditions for the run are an aqueous aerosol of 0.9% NaCl by weight with an MMD of 2.8 μm and a GSD of 2.3. The initial temperature of the air and droplets is 20.0°C, and the initial RH is 67%. By integrating the lognormal distribution, 2.3×10^7 droplets/cm³ are required to obtain the initial concentration of water of 11.892 $\mu\text{g}/\text{cm}^3$ calculated by Ferron *et al.*

The droplet growth was calculated at the following times after droplet creation: 0.1 seconds, corresponding approximately to the average residence time of the droplets in the nebulizer; 3.0 seconds, corresponding to the time Ferron *et al.* suggest that is required for the droplets to achieve equilibrium; and 30.0 seconds, as a check to ensure that the droplets are in equilibrium.

As can be seen in Table 3.8, Ferron *et al.* (1997) predict significant changes in both the MMD and GSD of the aerosol, while the model presented here indicates far smaller changes in these quantities. Most importantly, the hygroscopic growth model presented here does not predict significant changes in the properties of the aerosol after 0.1 seconds, indicating that the droplets are in equilibrium at that time. Changes in the MMD and GSD of the salt distribution with respect to the mass distribution seen with the

present model are consistent with a 0.9% increase in the average concentration of the droplets compared to the initial concentration.

4. CFD studies of particle deposition in the extrathoracic region of the respiratory tract

4.1 Introduction

The modeling of aerosol deposition in the human respiratory tract described in the previous sections of this thesis provides a powerful tool for the evaluation of inhaled aerosols and the devices which produce them. However, at best they provide estimates of the dosage delivered to three regions of the respiratory tract: the extrathoracic region, the tracheo-bronchial region, and the alveolar region; but they do not predict local sites of deposition within the regions, or local deposition patterns within specific airways. Experimental investigation can provide some insight into these areas, but such investigations depend on the availability of accurate casts (and therefore must deal with issues such as post-mortem changes in the airway geometry). Additionally, *in situ* experiments are difficult owing to the size and accessibility of the airways, often forcing the experimentalist to use surrogate geometries (usually based on a Weibel lung model).

Computational fluid dynamics, or CFD, is a popular research and design tool in many engineering disciplines and complements experimental research by providing the ability to manipulate specific features of the flow (e.g. the inlet profile) and by providing a

different paradigm from which to view a fluid flow problem. CFD refers to the use of numerical methods to solve the Navier-Stokes equations, which are the partial differential equations governing the flow of a single-phase Newtonian fluid. CFD can produce detailed simulations of fluid flow, and particles can be tracked through the flow to predict local deposition sites, and filtering efficiencies. The benefits of using CFD to study air flow and particle deposition in the respiratory tract include the use of more realistic geometric lung models, and not requiring drastic assumptions about the flow regime (i.e. 1-D plug flow).

Recently, commercially distributed, general purpose CFD software packages are becoming popular research tools in many areas, including aerosol research. Contributing to this increasing popularity are easy-to-use graphical interfaces, inexpensive computers, and robust solvers. However, CFD programs have not matured enough that they can be used without considerable attention to the validity of results they produce. This is true for codes written for specific geometries, and even more so for commercial, general purpose software packages. It is far beyond the scope of this thesis to discuss all of the issues involved in using CFD, but there are numerous textbooks which discuss in detail the use of CFD techniques for obtaining flow simulations, from an introductory level (e.g. Anderson, 1995) through to an advanced level (e.g. Fletcher, 1991) that a reader can reference. Additionally, Finlay *et al.* (1996) briefly discuss some of the issues involved in the use of these techniques in the context of simulating fluid flow and particle deposition in the respiratory tract. Some of the issues discussed in these references are reviewed here for completeness.

One of the main issues in the use of CFD is the nature of the equations being solved. The Navier-Stokes equations are a system of three-dimensional, nonlinear, coupled partial differential equations, and the complete equations (without simplifying

assumptions) contain all of the physics governing the motion of Newtonian fluids. Unfortunately, the highly nonlinear, three-dimensional nature of the equations means that analytical solutions cannot be obtained except in a handful of simple geometries (see e.g. Wang 1991, Panton, 1996). Furthermore, the complete Navier-Stokes equations are impractical to solve numerically in all but the simplest of geometries, and on the computers of today, solution in many geometries is only possible if certain aspects of the flow, such as turbulence, are modeled.

Additionally, the nature of the Navier-Stokes equations themselves make it difficult to extrapolate from one geometry to another, so that even experienced CFD users may be able to supply little *a priori* knowledge regarding the flow in a new geometry.

The purpose of this section of the thesis is to investigate the usefulness of CFD techniques for studying fluid flow and aerosol deposition in the respiratory tract. A commercial general purpose CFD software package (TASCflow3D, Advanced Scientific Computing Ltd., Waterloo, ON) is used to study the fluid flow and particle deposition in a novel geometrical model of the extrathoracic airways of the respiratory tract (c.f. section 3.3 for a complete description). TASCflow3D solves the Reynolds-averaged Navier-Stokes equations on block-structured, non-orthogonal, body fitted grids with equal-order velocity-pressure interpolation (Prakash & Patankar, 1985). TASCflow3D is unique among commercial CFD codes in that the equations are written in strong conservation form and solved using a finite volume method, while a finite element method is used to describe the geometry and grid transformations. (The strong conservation form of the Navier-Stokes equations provides some programming convenience, as well as some numerical advantages over a non-conservation formulation. Finite volume methods provide an advantage in that continuity is satisfied at each iteration, not only when the solution has converged. See Anderson (1995) for a detailed explanation.)

The CFD software will be tested in three stages. First, the particle deposition will be calculated for flow through round tubes with a 90° bend and compared to experimental results available in the archival literature. Second, the flow and particle deposition in a geometry similar to the model throat used with an impinger (USP, 1995) was calculated. The deposition patterns and filtering efficiencies were determined experimentally by viewing the deposition of a radiolabelled aerosol in a fiberglass model of the geometry, then comparing with the CFD results. Finally, the flow and particle deposition in a novel throat geometry was calculated and compared with experimentally determined filtering efficiencies and deposition patterns from viewing the deposition of radiolabelled aerosol in a fiberglass model of the geometry. Additionally, the filtering efficiencies of the model throat are compared with estimates of the *in vivo* deposition probabilities in the extrathoracic region available in the archival literature.

A priori, CFD is expected to perform poorly in the USP model throat and the physiologically realistic throat model. First, the Reynolds numbers of the flows in these models is on the order of a few thousand, so transition flow between laminar and turbulent flow can be expected. (In the case of the USP model throat, a scale model of the geometry was tested in a water channel with fluorescent dye illuminated by a sheet laser, and turbulent flow was observed. In the extrathoracic airways, the flow is known to be turbulent, see e.g. Dekker, 1961) Current turbulence models are known to perform poorly with these flows. Additionally, turbulence models are known to perform poorly in flows such as these with recirculation regions and curved streamlines.

Relatively few articles are available in the archival literature describing the use of CFD for studying the fluid flow and particle deposition in the respiratory tract. CFD has been used successfully to study the air flow and particle deposition in airway bifurcation's corresponding to the 4th to 5th bifurcation in a Weibel lung (see e.g. Hofmann &

Balàshàzy 1991, Balàshàzy & Hofmann 1993, Hofmann *et al.* 1996) where the Reynolds number is on the order of a few hundred, and the flow can be expected to be laminar.

Martonen *et al.* (1993) used a commercial CFD package to solve the two-dimensional, laminar, Navier-Stokes equations in an axisymmetric model of the larynx, trachea, and main bronchi. Unfortunately, the presented solution is for laminar flow, when the flow in the trachea is clearly turbulent at the flow rates studied (see Section 1.3 for a detailed discussion and references), so the results have limited applicability to the flow in a human.

Recently, Yu *et al.* (1996) used a commercial CFD code to study the flow patterns and the deposition of ultrafine particles in a model of the trachea and main bronchi and show reasonable agreement with the experimental data of Schroter & Sudlow (1969), who experimentally studied the flow patterns in airway bifurcation's over a wide range of Reynolds numbers. While the computational results seem to be sufficient for the bifurcation model studied, caution must be used when applying these results to the respiratory tract because, similarly to the above mentioned work, laminar flow is assumed in the trachea. Additionally, Yu *et al.* comment on the sensitivity of their results to the inlet boundary conditions, and yet they neglect any effects that the larynx may have on the flow in the trachea.

Katz & Martonen (1996a) present numerical simulations of flow through a model of the larynx using FIDAP (Fluid Dynamics International, Inc., Evanston IL), a commercially available CFD package that uses a finite element method to solve the Navier-Stokes equation. The geometry is based on laryngeal casts (Martonen & Lowe, 1983), with the glottal opening approximated as an ellipse. The oral and pharyngeal cavities are not simulated, and the trachea is assumed to be a circular cylinder. Three glottal openings are studied, corresponding to sedentary, light work, and heavy work flow rates (15, 30, and 60 liters/min., respectively). In the companion paper, Katz & Martonen (1997b) use the

particle tracking features of FIDAP to predict time averaged particle paths through the geometry. However, the purpose of the article is to investigate the air flow through the larynx using the tracks of massless particles to visualize the flow field. No information on the size of the particles is given, and the filtering properties of the model are not investigated.

4.2 Calculation of particle trajectories

In CFD, particle deposition probabilities are calculated by tracking individual particles through the geometry, and if a particle contacts a wall, then the particle is said to have deposited in the geometry, and the deposition location is recorded. By tracking many particles through the geometry, a statistical description of particle deposition can be obtained.

Particle trajectories are calculated by solving the equation of motion of a rigid sphere in the flow which was derived by Basset, Boussinesq and Oseen (Hinze, 1975), and is discussed in detail by Maxey & Riley (1983) and Berlemont *et al.* (1990), and is briefly reviewed here. In this work, we assume one-way coupling between the particles and the flow, that is, the flow influences the paths of the particles, but the particles do not affect the flow. This is a reasonable assumption for the particle number densities output by jet nebulizers. (It is important to distinguish the coupling used with the particle tracking and the coupling used with the hygroscopic growth calculations. Two-way coupling between the droplets must be considered with the hygroscopic growth calculations. The source terms in the momentum equations from the particles are approximately 5 orders of magnitude lower than the other terms of the momentum equations for the aerosol number densities typically output by jet nebulizers, and may be ignored). In this preliminary work,

we choose to avoid the added complications of hygroscopic particles, and only consider inert particles.

The equation of motion for a particle traveling in a continuous fluid is (Maxey & Riley, 1983):

$$m_p \frac{dv_p}{dt} = 3\pi\mu d C_{cor} (v_f - v_p) + \frac{\pi d^3 \rho_f}{6} \frac{dv_f}{dt} + \frac{\pi d^3 \rho_f}{12} \left(\frac{dv_f}{dt} - \frac{dv_p}{dt} \right) + \frac{3}{2} d^2 \sqrt{\pi \rho_f \mu} \int_{t_0}^t \frac{\left(\frac{dv_f}{dt'} - \frac{dv_p}{dt'} \right)}{\sqrt{t - t'}} dt' + F \quad (4.1)$$

where m_p = particle mass
 v = instantaneous velocity
 ρ = density
 μ = dynamic viscosity
 F = external forces on the particle (e.g. gravity, electrostatic forces);
 C_{cor} = drag coefficient for spheres (dependant on Reynolds number)

and t_0 is the starting time. The subscript, f , refers to the fluid and the subscript, p , refers to the particle. The first term on the right-hand side of Equation (4.1) is the Stokes drag (or viscous drag) on the particle. The second term is the force applied on the particle from the stress gradients (usually pressure) in the fluid surrounding the particle. The third term on the right-hand side is the virtual mass term, and accounts for the force necessary to accelerate the virtual mass of the fluid in the volume occupied by the particle. The fourth term on the right-hand side is the Bassett history term, and is essentially an unsteady correction to the Stokes drag term.

For particles that are significantly heavier than the surrounding fluid, Equation 4.1 reduces to:

$$\frac{\pi d^3 \rho_p}{6} \frac{dv_p}{dt} = 3\pi\mu d C_{cor} (v_f - v_p) + F \quad (4.2)$$

Here, the force on the particle is essentially given by the sum of the Stokes drag and any external forces.

To account for the influence of turbulent fluid fluctuations on particle motion, an eddy lifetime model is used. It is assumed that a single characteristic eddy can be defined for the flow with a characteristic fluctuating velocity, v'_f , lifetime, τ_e , and length, l_e , which are calculated from the local turbulence properties of the flow. When a particle enters an eddy, the fluctuating velocity v'_f is added to the mean fluid velocity to obtain the instantaneous fluid velocity used in Equation. (4.1). The particle will remain in the eddy, responding to the same instantaneous fluid velocity as long as the particle/eddy interaction time is less than the eddy lifetime, τ_e , or the displacement of the particle relative to the eddy is less than the eddy length, l_e . If either of these conditions is exceeded, the particle is assumed to be entering a new eddy with new characteristic v'_f , τ_e , and l_e .

The fluctuating velocity, eddy lifetime and length are calculated based on the local turbulence properties of the flow:

$$v'_f = \Gamma \left(\frac{2k}{3} \right)^{1/2} \quad (4.3)$$

$$l_e = \frac{C_\mu^{3/4} k^{3/2}}{\varepsilon} \quad (4.4)$$

$$\tau_e = \frac{l_e}{(2k/3)^{1/2}} \quad (4.5)$$

where k and ε are the local turbulence kinetic energy and dissipation, C_μ is a turbulence constant, and Γ is a normally distributed random number to account for the randomness of turbulence around a mean value. Note that each eddy will have three fluctuating velocities (u' , v' , w'), one for each coordinate direction, and that each is calculated separately using Equation (4.3).

Particles are distributed randomly over the inlet boundary, and are tracked individually through the computational domain using an explicit Euler integration of the particle velocity over the timestep δt ,

$$x_i^n = x_i^o + \frac{dx_i^o}{dt} \delta t \quad (4.6)$$

where the superscripts o and n refer to the old and new values, respectively, and the particle velocity is $v_{p_i} = dx_i/dt$. For heavy particles as considered here, the velocity at each timestep is calculated using the analytical solution to Equation (4.2) given by:

$$v_p = v_f + (v_p^o - v_f) \exp\left(\frac{-\delta t}{\tau}\right) + \tau F \exp\left(\frac{\delta t}{\tau}\right) \quad (4.7)$$

where

$$\tau = \frac{d^2}{18\mu C_{cor}} \left(\rho_p + \frac{\rho_f}{2} \right) + \frac{d}{C_{cor}} \sqrt{\frac{\rho_f \delta t}{4\pi\mu}} \quad (4.8)$$

Here, v_p^o is the particle velocity at the start of the time step.

The timestep δt used in the calculation of the particle trajectories is independent of the timestep used in the main flow calculations, and is limited by three criterion:

1. a particle cannot travel beyond a flux element boundary;
2. a particle can travel a maximum of 1/5 of the characteristic flux element length (this fraction is user definable, and the default value of 1/5 is used here);
3. for turbulent flows, a particle cannot travel beyond an eddy, and the timestep must be smaller than the eddy lifetime.

The particles are tracked until they either contact a wall of the geometry, or until they exit the geometry through the outlet boundary.

4.3 Turbulence models and boundary conditions for turbulent flows

Before modeling a flow using current CFD methods, it must be decided whether the turbulent or laminar model equations are to be used. The USP model throat and the physiologically realistic throat model described in the next section will be studied at a flow rate of 28.3 liters/min, corresponding to the flow rate through an Andersen Mark II cascade impactor. The Reynolds number of the flow at the exit of the impinger model throat is approximately 1550, slightly less than the transition value of 2300 for straight tubes. However, because of the complex geometry, turbulence may be present in the flows. A scale model of the geometry was built and tested in a water channel, and turbulent flow was observed. In the physiologically realistic model described in Section 4.4, the Reynolds number through the larynx at the same flow rate is 2600, so turbulence may be expected. Recall from Section 2.3 that turbulence is present in tracheal flow at Reynolds numbers lower than those considered here. Thus for both geometries, the flow is unlikely to be laminar. The choice of turbulence model used in the calculations is an important consideration as it has implications on the structure of the grid that can be used. (Two turbulence models are available in TASCflow3D, a standard $k - \varepsilon$ model, and a two-layer model which will be described later in this section) The reader is referred to one of the many texts on turbulence modeling (e.g. Wilcox, 1993) for a complete discussion of this topic, and only a few of the issues directly applicable to the work here will be discussed.

It can be shown that the equations used in a standard $k - \varepsilon$ turbulence model do not accurately predict the flow profiles near solid boundaries (see e.g. Wilcox 1993).

Therefore, unsatisfactory results may be obtained if an attempt is made to apply the no-slip boundary condition for fluid flow at a wall and integrate through the boundary layer. To

avoid this, an algebraic expression is used to calculate values of the turbulence kinetic energy and the dissipation at the grid point closest to the wall. These algebraic expressions are called wall functions, and are only valid in the log layer, normally considered to be $30 \leq y^+ \leq 500$, where y^+ are dimensionless wall units defined as:

$$y^+ = \frac{u_\tau y}{\nu} \quad (4.9)$$

where: $u_\tau = \sqrt{\tau_w / \rho}$ is the friction velocity
 τ_w = wall shear stress
 y = distance above the wall
 ν = fluid kinematic viscosity

Therefore, to use wall functions, the first grid point away from the wall should be at a y^+ value of $30 \leq y^+ \leq 500$, and grid generation often becomes an interactive process where a grid is created, then a solution obtained, and it is then determined if the grid point closest to the wall requires repositioning.

In the case of the USP model throat, this creates a difficulty as the diameter of the inlet tube is on the order of a few hundred y^+ units in diameter. This would require that the first grid point be approximately 1/4 of the way from the wall to the centerline, and more than 3/4 of the cross sectional area of the flow would be predicted by the first layer of nodes away from the wall.

Overcoming these shortcomings requires the use of a low Reynolds number turbulence model. Often, damping functions are added to the standard $k - \varepsilon$ model equations in the region $y^+ \leq 50$ to allow integration through the viscous sublayer. TASCflow3D uses a different approach, and uses a one-equation turbulence model near the wall, and a standard $k - \varepsilon$ turbulence model away from the wall. (The model used here solves the turbulence kinetic energy equation and uses an algebraic expression with a damping function to calculate the dissipation. The equation for the turbulent viscosity also

contains a damping function.) Patel *et al.* (1985) compares this method with other low Reynolds number turbulence models and finds that it is both robust and accurate. If a low Reynolds number turbulence model is used, then the grid points near the wall must properly resolve the viscous sublayer, which typically requires on the order of 10 nodes below $y^+ \approx 10$.

4.4 Physiologically realistic throat model

Qualitative descriptions of the extrathoracic region of the airway are available in anatomy textbooks (c.f. get some anatomy text reference). These textbooks provide the reader with a detailed description of the features of the airway, their function, and their location in relation to other structures. However, they do not provide the quantitative information necessary to construct a model for use with CFD.

Taking measurements of the extrathoracic airways is complicated by the presence of soft tissues, for example, the tongue. It is well known that the tongue changes the shape of the pharynx and mouth for the production of speech (c.f. Baer *et al.*, 1991, Sorokin, 1992), and the glottal width varies through the breathing cycle (Brancatisano *et al.* 1983). The presence of these soft tissues also complicates the use of casts, as it is difficult to preserve the shape of these tissues post mortem.

Here, we choose to base our geometrical model on data from computed tomography (CT) scans, magnetic resonance imaging (MRI) scans, and direct observation of living subjects. Where possible, the model is based on information available in the archival literature, and supplemented with measurements from CT scans of patients ($n = 10$) at the University of Alberta Hospital with no visible airway abnormalities, and by personal observation of living subjects. By using these dimensions, and simple geometric shapes, a model of the extrathoracic airways suitable for study with CFD is developed.

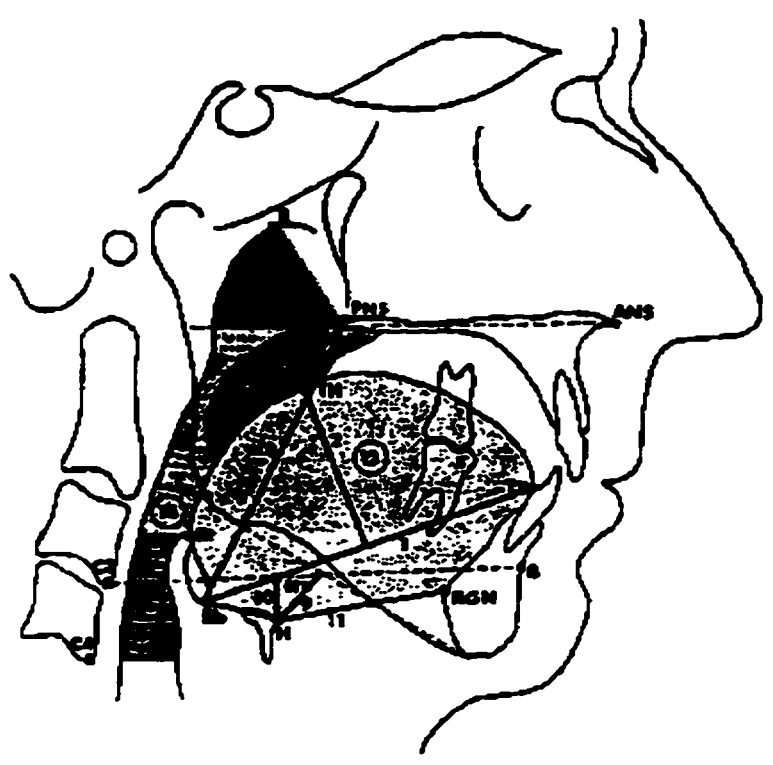


Figure 4.1. A schematic representation of the mouth and pharynx showing the cephalometric variables measured by Pae *et al.* (1994). Dimensions used in the creation of the model throat described here include: 1, tongue length; 2, tongue height; 4, maximum palate thickness; 7, inferior airway space; 8, vertical airway length.

Description of the model will proceed from the trachea to the mouth. A basic knowledge of the anatomy of the extrathoracic airways is assumed, and the reader is referred to an anatomy text for a description of the anatomical terms.

The trachea is a nearly cylindrical tube contained by a series of cartilaginous rings. It's length and diameter are well studied, and we adopt the values specified in the Weibel 'A' model scaled to 3 liters (see Table 2.1 for dimensions). For simplicity, we assume a smooth circular tube and neglect the cartilaginous rings. Martonen *et al.* (1993) study the effect of cartilaginous rings on the flow through tubes equivalent to generations 2-6 of a Weibel lung with a commercial CFD package and found that the presence of the rings had the effect of slightly narrowing the core flow of the tube. However, our interest here is in

deposition proximal to the trachea (i.e. extrathoracic deposition). The absence of cartilaginous rings in our model will not significantly affect our testing the usefulness of CFD for studying fluid flow and particle deposition in the extrathoracic airways.

The larynx has been studied more extensively to understand its role in the production of speech. Models which describe the vocal cords as a number of coupled masses (e.g. Titze, 1973, Titze, 1974) are of limited use for particle deposition as they focus on the high frequency vibrations of the vocal cords during speech production, and the propagation of that sound through the pharynx and oral cavities (also called the vocal tract). The vocal tract is often modeled as a series of cylindrical tubes (Titze uses 18) with a common axis of symmetry, which approximates the cross sectional area of the airways as measured by acoustic reflection.

More realistic models of the larynx have been developed for studying the fluid flow through, and the pressure drop across, the glottis. Scherer & Titze (1983) presented a detailed model of the larynx from which we adopted the length of the glottal opening (1.2 cm), the thickness of the glottal folds (0.29 cm), and the horizontal distance between the posterior side of the glottal opening and the posterior wall of the pharynx (1.12 cm). Brancatisano *et al.* (1983) studied the respiratory movements of the vocal cords and found that the width of the glottal opening varied during tidal breathing, with a maximum glottal width of 10.1 ± 5.6 mm (mean \pm standard error) and a maximum cross sectional area of 126 ± 8 mm². For our model, we assumed the glottis was an elliptical tube with a major axis of 1.2 cm, corresponding to the anterior-posterior measurement, and a minor axis of 1.0 cm, corresponding to the transverse measurement. The cross sectional area of the larynx presented here is 95 mm², about half way between the maximum opening seen during inhalation, and the maximum opening seen during exhalation (70 ± 7 mm²). The glottis is smoothly attached to the trachea.

Observations of CT scans ($n = 10$) indicated that the superior tip of the epiglottis was 20 mm above the floor of the pharynx, and angled at approximately 30° to the posterior wall of the pharynx. The epiglottal folds form a tube with a diameter of approximately 1.6 cm, which smoothly joins with the glottis.

The pharynx itself is often modeled as a cylindrical tube as the anterior and posterior walls are nearly parallel. Rodenstein *et al.* (1990) found that for healthy subjects, the pharynx had an anteroposterior/transverse ratio of 0.4. Thus, for our model, we assumed the pharynx was an elliptical cylinder with the major axis (in the transverse direction) 2.5 times as large as the minor axis (in the coronal plane). The anteroposterior dimension of the airway has been measured by Lowe & Fleetham (1991), Lowe (1994), and Pae *et al.* (1994) in a total of 44 normal subjects, and the average value of 13 mm is adopted for this model. A study involving the reconstruction of the pharynx from CT scans in 85 healthy volunteers showed that in most cases, the pharynx is slightly narrower in the transverse direction near the soft palate than near the epiglottis, while the anteroposterior dimension is constant (Lowe, 1996). To account for this, the anteroposterior/transverse ratio is increased to 0.5 at the top of the pharynx. The average cross sectional area of the model pharynx is 2.98 cm^2 , which compares favorably to the average value of $2.86 \pm .34$ (mean \pm standard error) measured by Haponik *et al.* (1983) from CT scans.

The teeth were modeled from bite impressions ($n = 5$) as a semi-circle with a diameter of 25 mm, with the teeth extending back 50 mm from the lips, to a width of 45 mm at the posterior end. The upper and lower teeth were assumed to be parallel, with a 1 cm opening between them. The studies of by Lowe & Fleetham (1991), Lowe (1994), and Pae *et al.* (1994) provided the measurements to locate the roof of the mouth (a vertical

distance of 72 mm from the base of the epiglottis) and the tip of the tongue (81 mm from the base of the epiglottis) which locate the mouth relative to the larynx and pharynx.

The vault of the mouth in a coronal section is often described as a segment of a circle whose radius decreases approaching the mouth (Sorokin, 1992). Here, we have assumed that the curvature in the hard palate is constant, with a radius equal to the curvature of the front of the teeth (i.e. $R=12.5$ mm). The walls of the mouth are joined smoothly with the walls of the pharynx, with the exception of a small step corresponding to the tip of the soft palate. The uvula is not represented in this model.

The tongue is a large mass of muscle, and as noted above, is known to vary dramatically during the production of speech. Very little is known about the position of the tongue during normal respiration. Subjects ($n = 5$) were asked to hold an MDI canister (1 cm opening) between their teeth, inhale, then remove the MDI without changing the position of their jaw or tongue. It was observed that the tip of the tongue was slightly below the bottom teeth, and the top of the tongue was flat, and crossed the upper teeth approximately 3/4 of the way back. The tongue is therefore assumed to be flat in the anterior part of the mouth, beginning 5 mm below the bottom teeth, and crossing the upper teeth 40 mm from the front of the mouth. It is then smoothly joined with the anterior wall of the pharynx.

A fiberglass cast of the model was made from a hand carved wood mold. The volume of the geometry to the top of the trachea is 52 cm^3 , which compares favorably with the 49 cm^3 given by the International Committee for Radiological Protection (ICRP, 1994) for the volume of the extrathoracic airways.

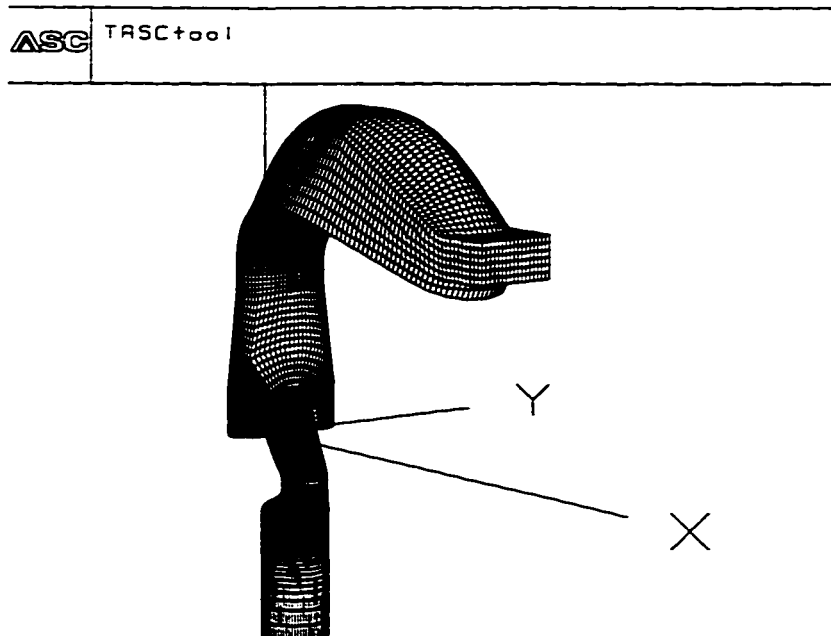


Figure 4.2. An isometric view of the physiologically realistic throat model showing the mouth, larynx, and pharynx. A square inlet is added to the front teeth. Note that the trachea has a total length of approximately 10 cm and extends out of the picture to allow for a more detailed view of the mouth and pharynx. The epiglottis is not shown in this view.

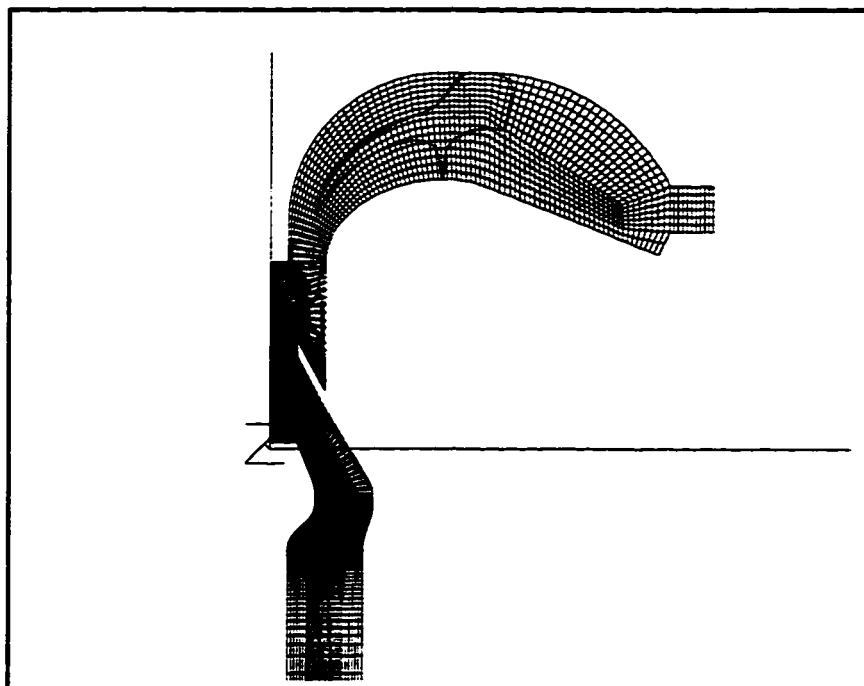


Figure 4.3: A view of the geometry through the symmetry plane showing the epiglottis and the internal structure of the model.

4.5 Particle Deposition in Bent Tubes

To validate our use of TASCflow3D, and its particle deposition predictions, it is useful to first consider a simple geometry where laminar flow is expected. The deposition of inert particles from laminar flow in bent tubes was studied experimentally by Landahl & Herman (1949), Johnston & Muir (1972) and Johnston *et al.* (1977) and computationally by Crane & Evans (1977). Additionally, theoretical equations for the deposition have been obtained (Yeh, 1974, Cheng & Wang, 1975, Dui & Yu, 1980, Balashazy *et al.* 1990). As the Reynolds numbers in these flows is on the order of a few hundred, TASCflow3D should have little difficulty *simulating the air flow*, providing a simple way of validating the use of Lagrangian particle tracking to investigate aerosol deposition

This section will first overview the geometry used in the experimental studies, and the geometry chosen for this study, along with the flow regimes and the methodology for calculating the deposition in the bend. Secondly, the grid will be described, and it will be demonstrated that the solutions obtained are independent of the grid spacing and numerical influence from the outlet boundary condition. Next, the convergence criterion will be discussed, followed by the results.

4.5.1 Geometry

Here, we have chosen a 1.5 mm diameter tube with a 19.0 mm bend radius and a 90° bend angle as studied by Johnston *et al.* (1977). Here, a 50.0 mm length of straight pipe is added to the upstream end of the bend, and a 100.0 mm length of straight pipe is added to the downstream end of the bend to ensure that numerical artifacts from the outlet boundary condition does not affect the flow in the bend.

Three regions of the tube are defined for analysis of the deposition. Region 'A' corresponds to the inlet pipe, region 'B' corresponds to the bend itself, region 'C'

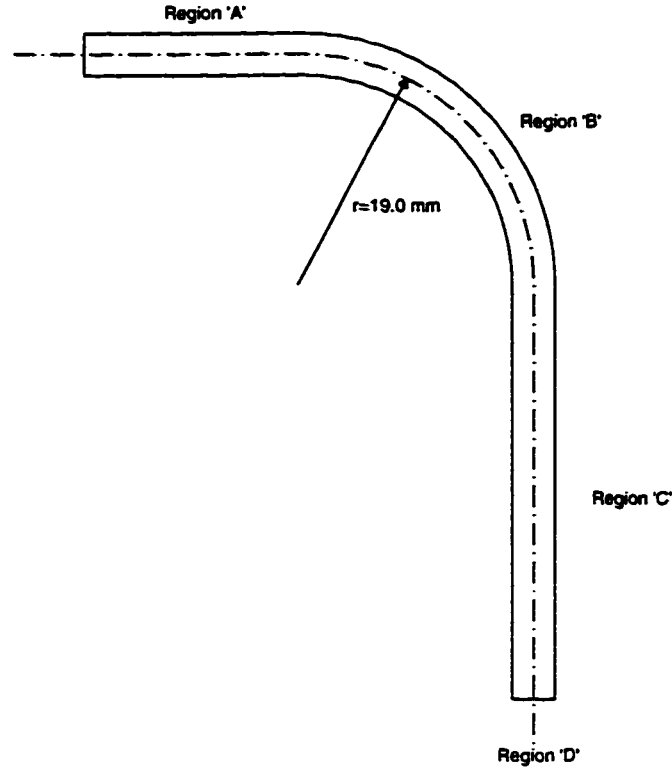


Figure 4.4. A schematic of the geometry of the bent tube. The diameter of the pipe is exaggerated for display purposes.

corresponds to the length of pipe after the bend. In addition, any particles that exit the geometry are collected on a filter, defined as region 'D'. The fractional deposition in the bend is then defined as:

$$DE = \frac{m_B}{m_A + m_B + m_C + m_D} \quad (4.10)$$

where m is the mass of particles collected in the region denoted by the subscript.

4.5.2 Grid

The base mesh used in the calculations is shown in Figure 4.5 and contains 58,695 nodes, or equivalently, 46,816 three-dimensional elements. First, it must be determined that the grid density is sufficient to resolve all the important flow features, and secondly, it must be determined that the exit boundary conditions are not influencing the results.

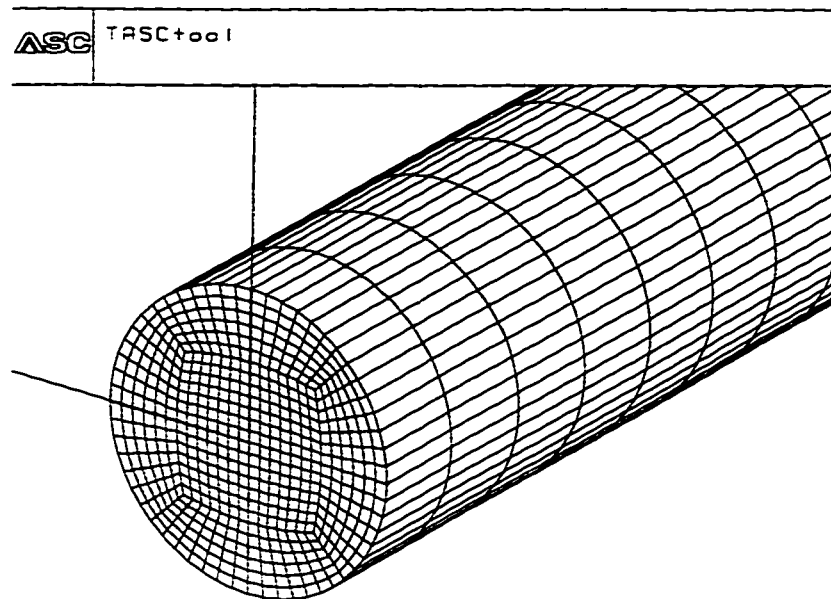


Figure 4.5. A partial view of the mesh used in the calculations showing the inlet and the mesh cross section. The large dot indicates the location of the end of the grid line used in the grid convergence studies.

The dependence of the solution on the grid density is checked for a flow rate of 0.3 liters/min. Three grid densities are used: the base grid described above, a low resolution grid with approximately twice the distance between nodes of the base grid (a total of 10,395 nodes), and a high resolution grid with approximately 1/2 the distance between the nodes of the base grid (a total of 352,175 nodes). Figure 4.6 shows the fluid speed along a gridline located approximately 1/2 of the distance between the center axis of the tube and the outside wall of the bend. The results predicted by the base grid and the high density grid are virtually identical. Figure 4.7 shows the pressure drop along the same line. Here, all three grids give similar results. It must also be determined that the exit boundary condition does not influence the solution in the region of interest. To do so, an extra 100.0 mm of tube is added to the exit pipe, and the speed and pressure drop along a grid line are

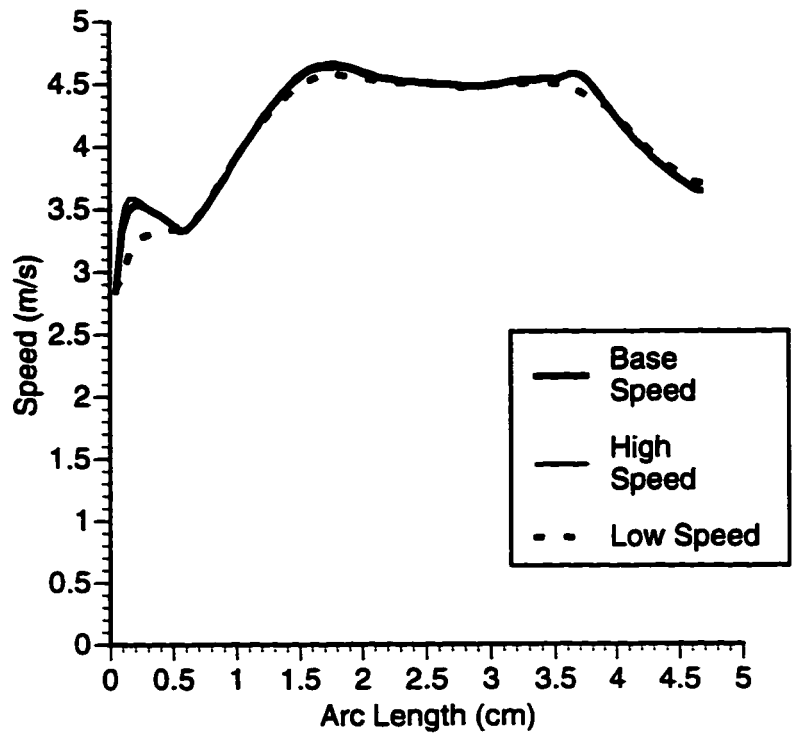


Figure 4.6. A plot of the speed of the fluid along a gridline for the three grid densities showing that the increasing the resolution of the grid beyond the base grid does not increase the accuracy of the results..

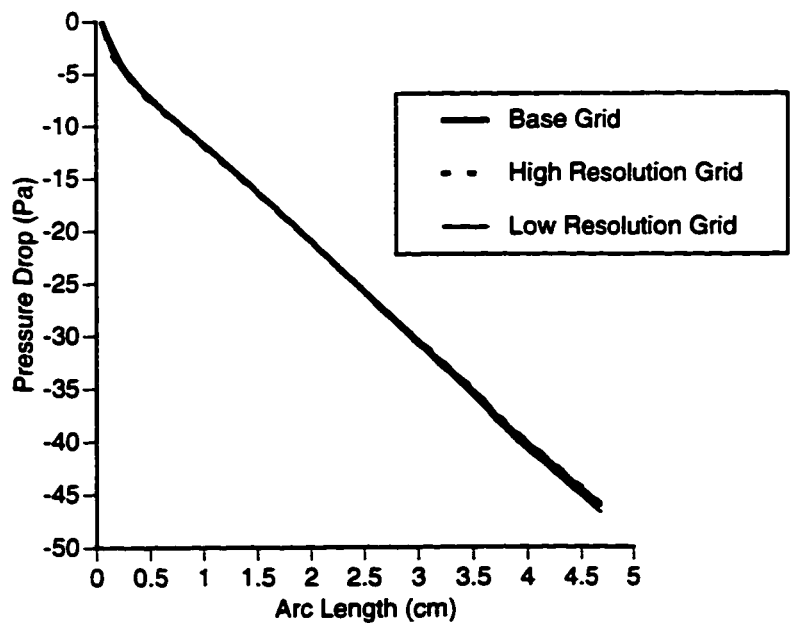


Figure 4.7. A plot of the pressure drop of the fluid along a gridline for the three grid densities showing that the increasing the resolution of the grid beyond the base grid does not increase the accuracy of the results..

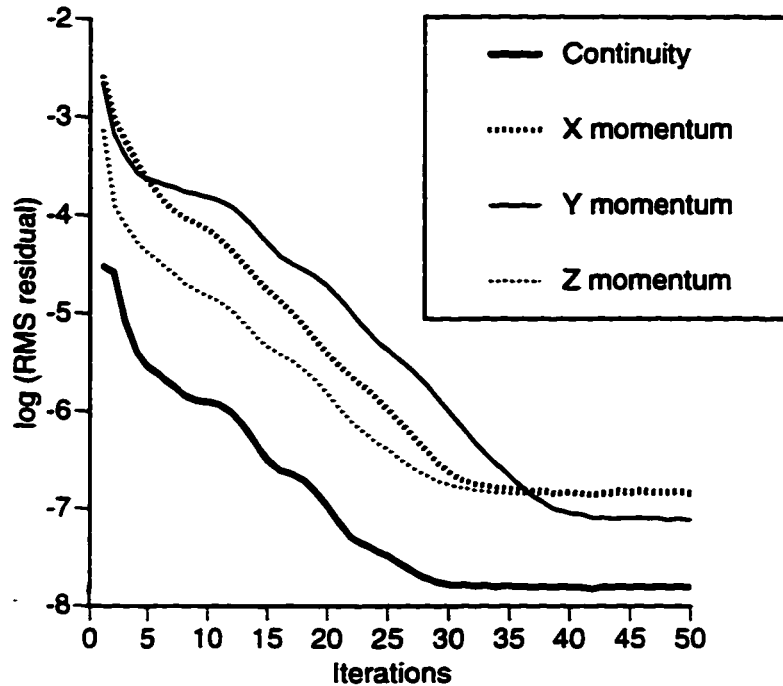


Figure 4.8. A typical plot of the dimensionless RMS residuals at each timestep for the calculations. In all cases, the maximum residuals at any grid point are less than one order of magnitude greater than the RMS value indicating that there are no local areas of high error.

compared. The difference between the two solutions is less than 0.001% at every grid point.

From the above tests, we can conclude that the solution calculated using the base grid is independent of the grid density and numerical influences from the outlet boundary conditions.

4.5.3 Convergence

Iterative convergence was achieved by allowing the code to run until there was no appreciable decrease in either the RMS value of the residual over the entire computational domain or in the maximum value of the residual at any grid point for a period of 10 iterations. Figure 4.8 shows a typical plot of the residual beginning from a uniform initial guess. Iterative convergence is achieved after approximately 40 iterations.

TASCflow3D also provides a report on the global conservation of the mass and momentum equations, an example of which is shown in Figure 4.8. The "Net Flow" gives an indication of the overall numerical accuracy of the solution. For example, the X-momentum at every grid point on the inlet boundary condition is summed (1.244×10^{-4} kg/m²s in Figure 4.9). This is repeated for the outlet boundary condition and the wall boundary condition. The "New Flow" is the sum of these values. Since TASCflow3D solves the Navier-Stokes equations in strong conservation form using a finite volume method, there will be no artificial sources or sinks from the numerical scheme, and non-zero values of the "Net Flow" will result from round-off errors and inaccuracies due to discretization and the finite differencing scheme. The "Net Flow", should be negligible with respect to the values at the boundary conditions to ensure an accurate solution. In this example, the "Net Flow" in the X and Y momentum is approximately 6 orders of magnitude lower than the boundary condition values, and the "Net Flow" for mass conservation are approximately 7 orders of magnitude less than the boundary conditions values. In the case of the Z momentum, the net flow is a much smaller fraction of the values at the boundaries, but in this case, the only source of Z momentum is the secondary

Momentum and Mass Flow Summary				
Boundary or source	X-momentum	Y-momentum	Z-momentum	Mass
B.C. # 1, WALL	-1.231E-04	-1.428E-04	4.061E-07	0.000E+00
B.C. # 2, OUTFLOW	-1.309E-06	1.428E-04	-4.046E-07	-1.548E-05
B.C. # 3, INFLOW	1.244E-04	2.963E-11	-7.071E-11	1.548E-05
Net Flow	-8.731E-11	4.953E-10	1.480E-09	-1.819E-12

Figure 4.9. A summary table of the mass flows from the same run shown in Figure 4.8. It can be seen that the net flow is approximately 5 orders of magnitude lower than the average values on the boundaries for X and Y momentum and conservation of mass.

flows generated as the air passes through the bends, which is small compared to the momentum in the X and Y directions. By considering both the iterative convergence and the mass flow summary, we can determine that the solutions are converged. For all the results presented in Section 4.5, the value in the RMS residuals over the entire flow field is always less than 2×10^{-7} . The “Net Flow” in the conservation of X and Y momentum are approximately 5 orders of magnitude less than the values at the boundaries.

4.5.4 Results

Once it was determined that a converged solution was obtained which was independent of the grid density, particles were injected in the flow, and their paths calculated. A total of 100,000 particles were injected at random locations across the inlet boundary of the tube. In the CFD calculations, a monodisperse aerosol of uranine particles having a diameter of $5.0 \mu\text{m}$ and density 1.3 g/cm^3 was assumed, similar to the particles used experimentally by Johnston *et al.* (1977). In Figure 4.10, our deposition probabilities calculated by CFD are compared with the experimental values of Johnston & Muir (1973) and Johnston *et al.* (1977), the computational results of Crane & Evans (1977), and the theoretical expression of Balàshàzy *et al.* (1990) for the inertial deposition in a bent tube. The CFD results presented here agree well with the available experimental data. Deposition patterns were not presented in the experimental studies, so comparisons of the deposition patterns are not possible.

In the above calculation, a uniform inlet velocity profile was used. When a parabolic inlet velocity profile was used, the differences in the deposition probabilities were less than 1% from those calculated with a uniform profile. Most theoretical investigations show a slight increase in the deposition efficiencies when a parabolic entrance profile is used. This departure from the theoretical predictions is the result of our long entrance tube

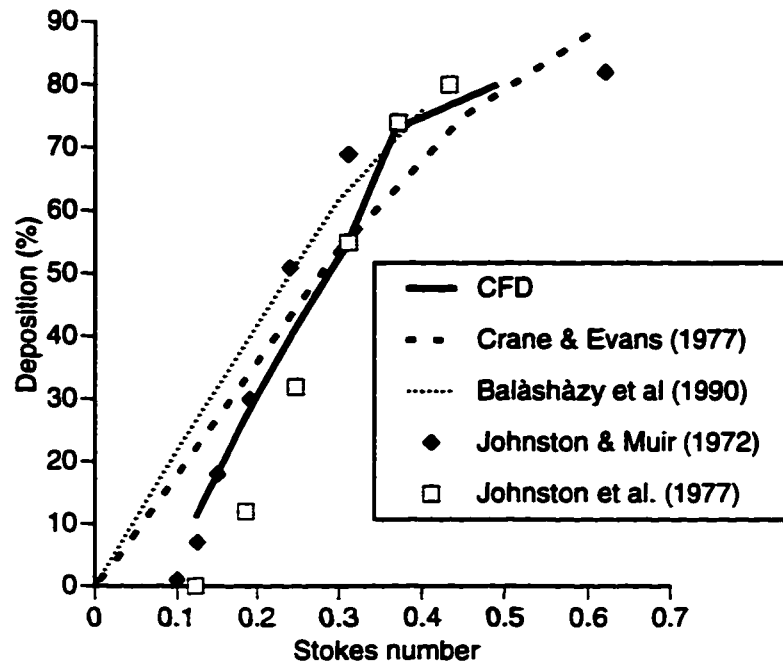


Figure 4.10. The calculated deposition in a tube with a 90° bend compared to experimental, theoretical, and other computational results. The results all show good agreement.

of approximately 30 tube diameters allowing the flow to develop before the bend is encountered.

From the results of this section, we can conclude that the Lagrangian particle tracking as implemented in TASCflow3D accurately reproduces the experimental deposition of aerosols in geometries where the flow is laminar and easily determined numerically.

4.6 Deposition in the USP model throat.

The second geometry studied is similar to the model throat described by the United States Pharmacopeia (1995) and will be referred to in this thesis as the USP model throat. The USP model throat is designed to be attached to the inlet of a cascade impactor, or a single stage impactor (described by USP 1995), to simulate the filtering capabilities of the

extrathoracic region of the respiratory tract. Here, we study this geometry because it provides an intermediate step between the simple geometry and flow of the bent tubes, and the complex geometry and flow of the physiologically realistic model throat.

4.6.1 Geometry and Grid

Fabrication instructions for this model are given in the USP (1995). In brief, the USP model throat consists of a 4.5 cm diameter sphere with a 2.9 cm diameter inlet tube with length 3.5 cm, and a 2.0 cm diameter outlet tube with length 2.0 cm oriented 90° from the inlet tube. On the inlet tube is a ground glass socket (female) to accept an adapter for the mouthpiece of the DPI or MDI being tested. The geometry studied here includes the inside surface of the ground glass socket. The outlet tube has a male ground glass socket to attach the impinger model throat to either a liquid impinger, or a cascade impactor. The geometry studied here includes the inside surface of the socket.

As was briefly mentioned in Section 4.3, generating a grid for the USP model throat requires consideration of both the flow and the turbulence model. Not only must the nodes be placed to resolve the flow features, but there must be enough nodes near the wall to resolve the damping functions used in the turbulence model. Figure 4.11 shows the base grid used in the calculations where it intersects the outside surface. Figure 4.12 shows the grid on the symmetry plane. It can be seen in both Figures 4.11 and 4.12 that the grid is much more dense near the walls, and near any sharp bends in the geometry.

This grid was created in an iterative manner. First, a solution was obtained on a uniform grid. The grid was refined wherever the maximum residual at a grid point was more than one order of magnitude greater than the RMS value of the residual, and the grid was resolved near the walls to obtain the necessary resolution for the damping functions. This process was repeated until an acceptable solution was obtained. The grid was then

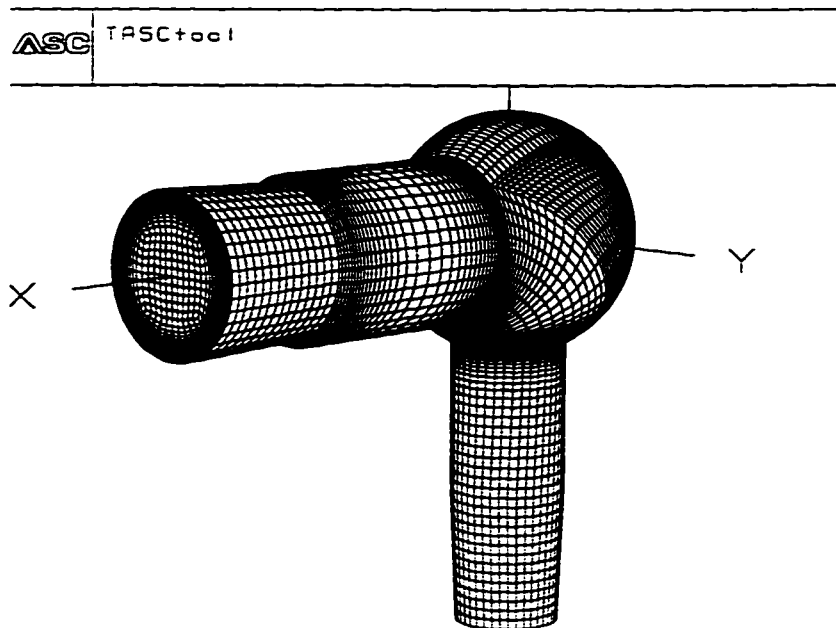


Figure 4.11. A view of the mesh for the USP model throat. The flow enters parallel to the X-axis, and exits at the bottom.

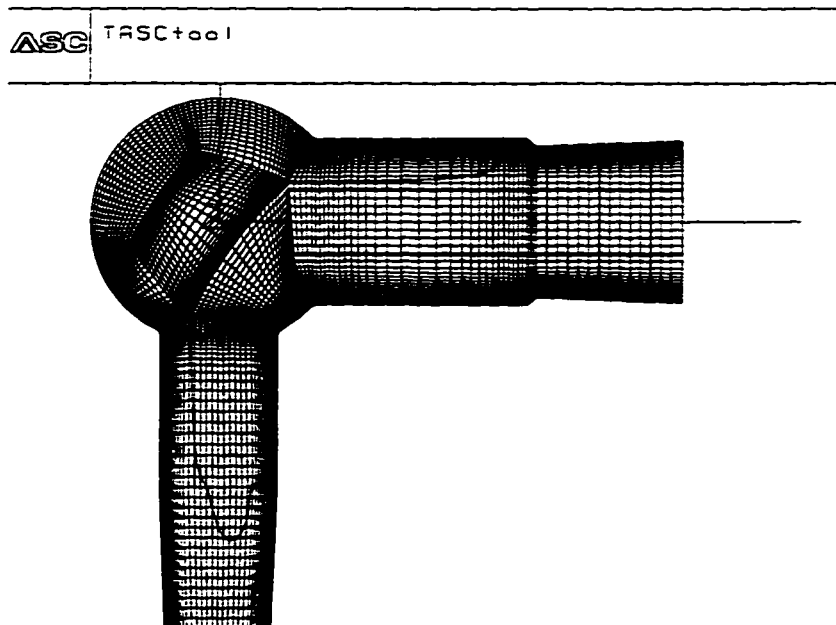


Figure 4.12. The grid for the USP model throat through the symmetry plane. The thick line gives the approximate location of the grid line used in the grid convergence studies.

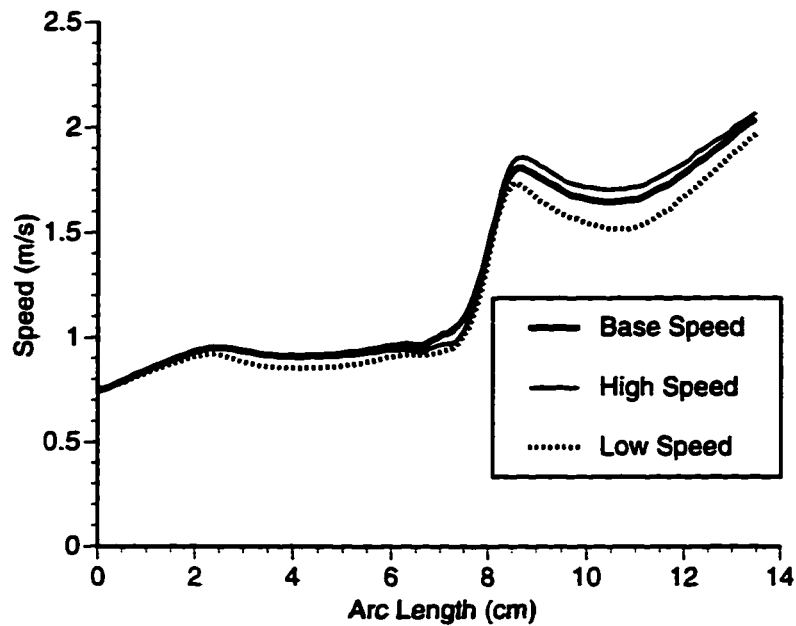


Figure 4.13. A plot of the speed of the fluid along a gridline for three grid resolutions of the USP model throat showing that increasing the resolution of the grid beyond the base grid results in only a slight increase in accuracy (<1% at all points).

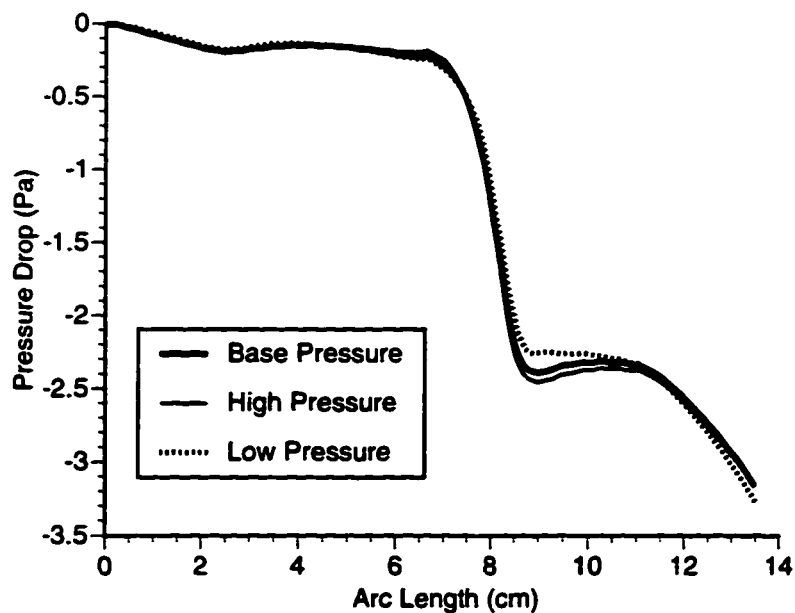


Figure 4.14. A plot of the pressure drop of the fluid along a gridline for three grid resolutions of the USP model throat showing that increasing the resolution of the grid beyond the base grid results in only a slight increase in accuracy (<1% at all points).

checked for grid convergence by increasing the spacing between the nodes by 50% in each direction to create a low resolution grid, and by decreasing the spacing between the nodes by 50% in each direction to obtain a high resolution grid. Figure 4.13 shows the fluid speed along a grid line, and the pressure drop is shown in Figure 4.14. From these results we can see that the base grid with 129,645 nodes is sufficiently resolved.

The final check on the grid is to ensure that the exit boundary condition does not influence the flow. An additional 10 cm of tube was added to the exit boundary condition, and it was found that both the velocity and pressure drop along a grid line differed by less than 0.05% at every grid point.

4.6.2 Boundary conditions

The airflow entering the model was assumed to be plug flow. To determine the value of the turbulence intensity at the inlet, the output of a Pari LC+ nebulizer was measured at a flow rate of 28.3 l/min (6.0 l/min from the compressor, and 22.3 l/min through the vent). The velocity distribution of aerosol droplets leaving the nebulizer was determined with a phase Doppler anemometer. Dividing the RMS value of the droplet velocity by the mean velocity exiting the nebulizer provided a turbulence intensity of 0.12 which is used as the inlet turbulence intensity for the calculations. The turbulence length scale is assumed to be 1/10 of the diameter of the inlet tube. The inlet turbulence length scale was varied 1/30 of the inlet tube diameter to 1/2 of the inlet tube diameter with no noticeable effect on the solution.

4.6.3 Convergence

Iterative convergence was achieved when the RMS residuals were all less than 4×10^{-6} . The maximum residual at any node was less than 3×10^{-5} showing that there are no local areas of high error on the grid. Additionally, Figure 4.15 shows that the “Net Flow”

Momentum and Mass Flow Summary				
Boundary or source	X-momentum	Y-momentum	Z-momentum	Mass
B.C. # 1, WALL	2.364E-03	-1.068E-03	1.113E-06	0.000E+00
B.C. # 2, INFLOW	-2.355E-03	8.563E-09	1.714E-09	5.478E-04
B.C. # 3, OUTFLOW	-9.536E-06	1.068E-03	-1.251E-06	-5.478E-04
Net Flow	-4.020E-07	1.377E-07	-1.357E-07	-2.212E-09

Figure 4.15. Mass flow summary for the flow solution on the base grid used in the particle tracking calculations. The “Net Flow” in the X-momentum and Y-momentum is approximately 4 orders of magnitude less than the boundary values, and the “Net Flow” in continuity approximately 5 orders of magnitude lower than the boundary values

in the conservation of X and Y momentum is approximately 4 orders of magnitude less than the values at the boundaries.

4.6.4 Experimental studies of aerosol deposition in the USP model throat

To validate the computational results, a wooden model of the USP throat geometry was built and used as a form for a fiberglass model. A Pari LC+ nebulizer was attached to the inlet of the USP model throat via heat-shrink tubing. The outlet was attached directly to a Marquest filter and a vacuum pump calibrated to draw 28.3 l/min of air through the apparatus. Figure 4.16 shows a schematic of the experimental setup. Normal saline solution (0.9% NaCl by weight) tagged with albutum colloid suspension is nebulized. The size of the aerosol produced by the specific nebulizer used in this study was measured to have an MMD of 4.8 μm and a GSD of 1.65 with a Dantek PDA system.

To ensure the validity of our assumption of inert particles in the CFD calculations, it is important to investigate the stability of the droplets exiting the nebulizer. The stability of the aerosol was determined by calculating the growth of the droplets through the nebulizer as described in Section 3.5, and it was found that more than 95% of the aerosol

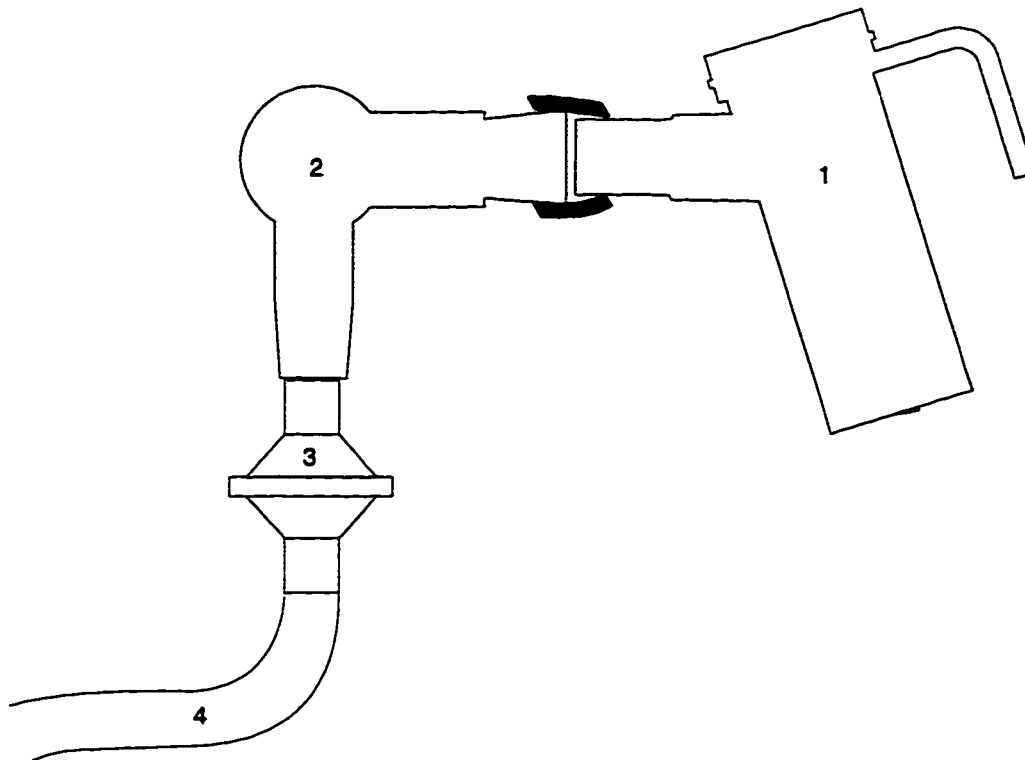


Figure 4.16. A schematic of the experimental setup used to determine the deposition of radiolabelled aerosols in the USP throat model. The nebulizer (1) is attached to the USP throat model (2) via heat-shrink tubing. Aerosol passing through the model is collected on a filter (3) attached to a vacuum pump via hosing (4).

was in equilibrium at the exit of the nebulizer. Additionally, Stapleton & Finlay (1997) showed that aqueous droplets produced by nebulizers can change size significantly when their size is measured by a cascade impactor due to heat transfer from the cascade impactor to the aerosol. It is useful to consider if this effect is important here.

To estimate an upper bound for the temperature drop of the fluid as it passes through the model, we will consider a straight tube with a diameter of 3.0 cm and a length of 10 cm, so that the diameter and volume of the test tube are close to the diameter of the inlet and exit tubes and the total volume of the USP model throat. (Note that this analysis is also applicable to the physiologically realistic throat model described in Section 4.7. because it has a similar volume and droplet residence time.) The equation for the increase in the bulk temperature of a fluid flowing through a tube is

$$\frac{T_{\infty} - T_{m,o}}{T_{\infty} - T_{m,i}} = \exp\left(\frac{-PL}{\dot{m}C_p} \bar{U}\right) \quad (4.11)$$

where T_{∞} = ambient temperature outside the pipe
 $T_{m,i}$ = mean temperature of the fluid in the pipe at the pipe inlet
 $T_{m,o}$ = mean temperature of the fluid in the pipe at the pipe outlet
 P = pipe circumference
 L = pipe length
 \dot{m} = mass flow rate through the pipe
 \bar{U} = average resistance to heat transfer

The only unknown on the right hand side of the equation is \bar{U} . To calculate a value for \bar{U} we first consider that the Nusselt number for steady laminar flow is 3.66. Using the heat conductance of water and the diameter of the pipe, a value for the convective heat transfer coefficient h can be calculated to be $h=5.0$. Then we can write (Incropera & DeWitt, 1990):

$$\bar{U} = \frac{1}{\frac{1}{h} + \frac{r_1}{\kappa} \ln\left(\frac{r_2}{r_1}\right)} \approx 5 \quad (4.12)$$

where r_1 and r_2 are the inner and outer radii of the tube, and κ is the heat transfer coefficient of the tube (fibreglass). Substituting into Equation (4.7), the maximum temperature drop is on the order of 0.4°C. Five micrometre droplets of isotonic saline exposed to this temperature difference would need to change their size by less than 1% to come into equilibrium with the new temperature. It can therefore be assumed that the droplets do not change size as they move through the model.

The aerosol was drawn through the model for 60 seconds, after which the model and filter were imaged by a Picker Prism 2000 gamma camera for 300 seconds. The fraction of aerosol depositing in the model was determined by counting the photons emitted by:

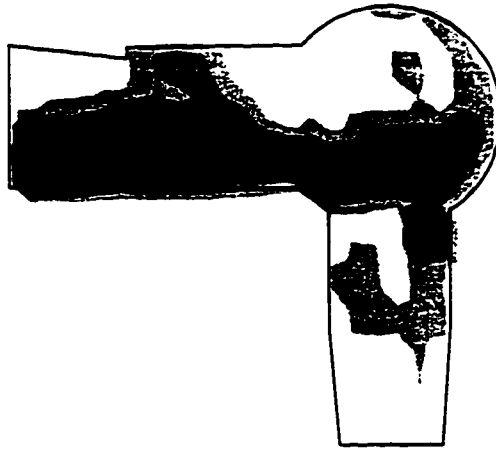


Figure 4.17. A greyscale image of the deposition of radiolabelled aerosol in the USP model throat. Air enters on the left, and exits on the bottom. The darker areas correspond to areas of higher deposition.

$$DE = \frac{C_m}{C_m + C_f} \quad (4.13)$$

where C_m is the number of counts from the model, and C_f is the number of counts on the filter. From Equation (4.10), 5.9% of the aerosol mass entering the USP model throat deposits on the walls.

The gamma camera image of the model shown in Figure 4.17 gives information on the deposition pattern in the model. It can be seen that there is significant deposition in the entrance tube, particularly in the region immediately downstream of the area corresponding to the ground glass inlet cone. In the spherical section of the USP throat model, most of the deposition occurs in a ring around the intersection with the exit tube. There is some deposition on the back of the sphere (i.e. on the side opposite to the inlet). There is minimal deposition in the exit tube, with most of it occurring on the back of the tube near the top.

4.6.5 Results

The flow in the USP model throat is complex, and highly three dimensional. The characteristics of the flow can be viewed by considering the tracks of massless particles injected in the flow. Figure 4.18 shows tracks from a side view, and shows the large recirculating regions in the spherical elbow. Aerosol enters from the right, and exits at the bottom. Figure 4.19 shows two vortical patterns that form in the sphere that are convected through the outlet tube.

Although the flow patterns in the USP model throat are interesting, here, we are primarily interested in the particle deposition. The particle deposition in this geometry was calculated using CFD for a monodisperse aerosol with a size equal to the measured MMD of the nebulizer. Additionally, the deposition for a polydisperse distribution with an MMD and GSD equal to that produced by the nebulizer was used.

Table 4.1 gives the quantitative results of the CFD particle calculations. The total deposition predicted by the CFD is approximately twice that seen in the experimental studies.

	Experimental Values	Monodisperse Aerosol	Aerosol Distribution
Inlet		0.3%	0.6%
Sphere		7.5%	8.0%
Outlet		3.6%	4.0%
Total	5.9%	11.4%	12.6%

Table 4.1. Calculated total deposition in the USP throat model showing the effect of using a monodisperse vs. a polydisperse aerosol. All values are a percentage of total mass of aerosol entering.

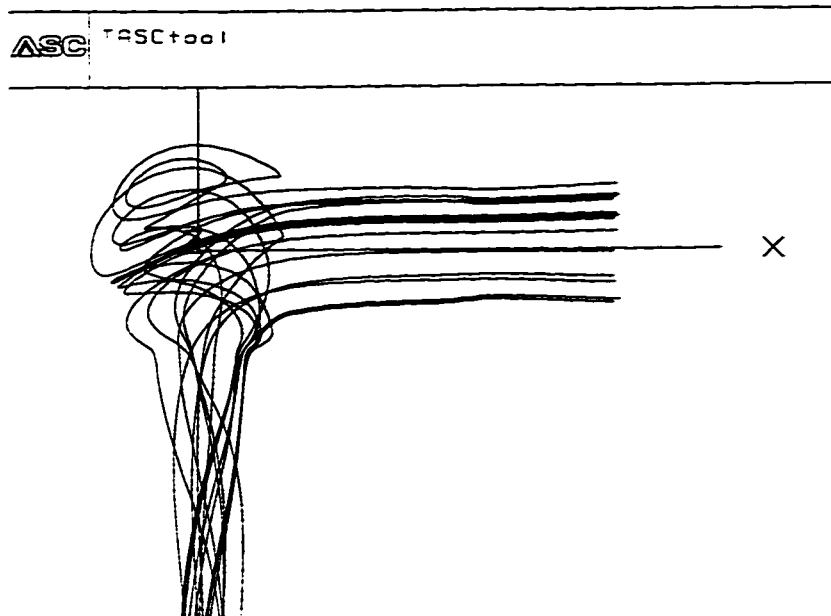


Figure 4.18. Tracks of massless particles in the USP model throat viewed from the side of the model. The flow enters from the right, and exits out the bottom.

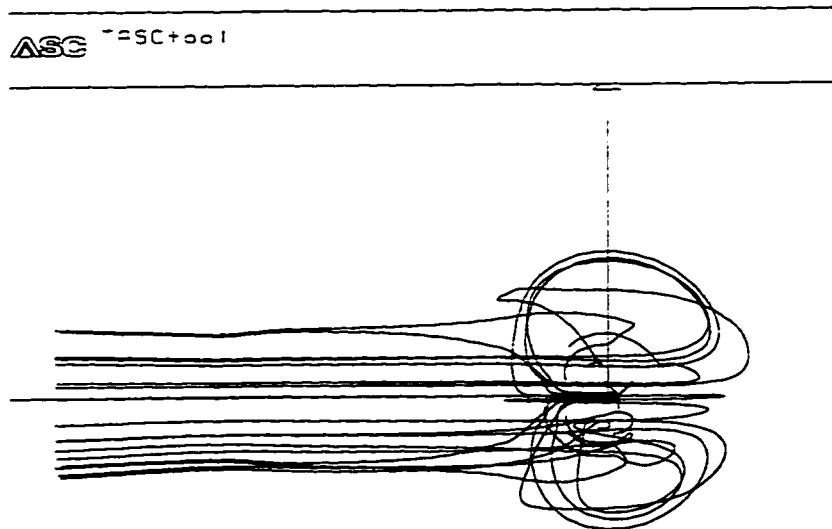


Figure 4.19. Tracks of massless particles in the USP model throat viewed from the top of the model. The flow enters from the left, and exits into the page.

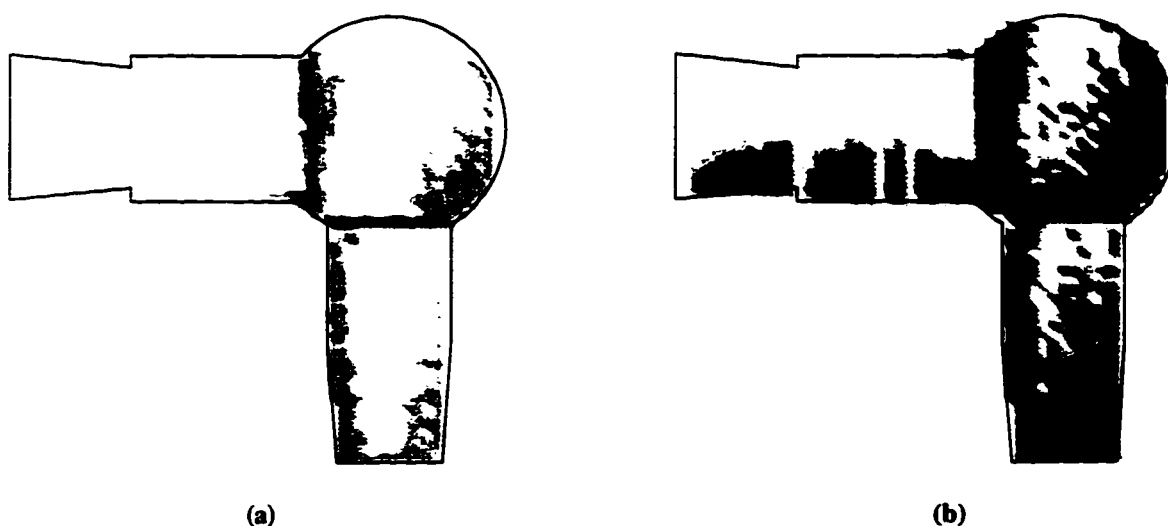


Figure 4.20. Calculated deposition patterns for the USP model throat. (a) shows the pattern for a monodisperse aerosol equal to the MMD of the aerosol produced by the nebulizer used in the experimental tests. (b) shows the calculated deposition pattern for a polydisperse aerosol with an MMD and GSD equivalent to the aerosol produced by the nebulizer.

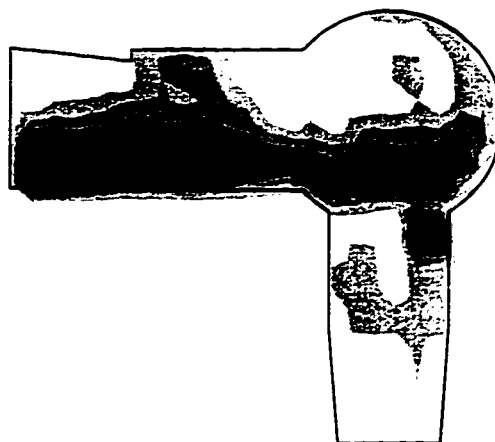


Figure 4.21. Experimental deposition in the USP model throat. This figure uses the same data as Figure 4.17 and is shown here for comparison purposes.

Figures 4.20 (a) and 4.20 (b) show the deposition pattern predicted by the CFD. Figure 4.17 is repeated here (as Figure 4.21) for comparison purposes. In the experimental results shown in Figure 4.22, most of the deposition occurs on the bottom of the inlet tube. In the computational results, most of the aerosol deposits in a narrow ring around where

the outlet tube intersects the sphere, with very little aerosol depositing in the inlet tube (this can also be seen in Table 4.1).

4.7 Aerosol deposition in the physiologically realistic throat model

4.7.1 Geometry and grid

The third geometry studied is the physiologically realistic throat model described in Section 4.4. The geometry contains many features that can be expected to complicate the flow calculations. For example, recirculation regions can be expected in the cavernous roof of the mouth, below the soft palate, and distal to the larynx.

The geometry was gridded with 63 blocks, and the base grid contains approximately 230,000 nodes. The surface grid is partially shown in Figure 4.2, and a cross section of the base grid through the symmetry plane is shown in Figure 4.22.

Two distinct areas of the grid can be identified. The first consists of regions where the flow impinges on a wall (e.g. on the posterior wall of the roof of the mouth, and on the inferior end of the pharynx) or where the flow recirculates (e.g. the roof of the mouth, posterior wall of the pharynx). In these areas, the law of the wall is not expected to be valid. The design of the base grid placed first grid point at $y^+ \leq 10$ in some of these regions, but because the law of the wall is not valid, this is acceptable. In regions where a reasonable approximation of boundary layer flow can be expected, for example on the tongue or in the trachea, the first grid point is at $y^+ \geq 25$. A standard $k - \epsilon$ turbulence model with wall functions was used.

Grid convergence was determined by comparing the base grid with a low resolution grid with approximately 60,000 nodes, and with a high resolution grid with

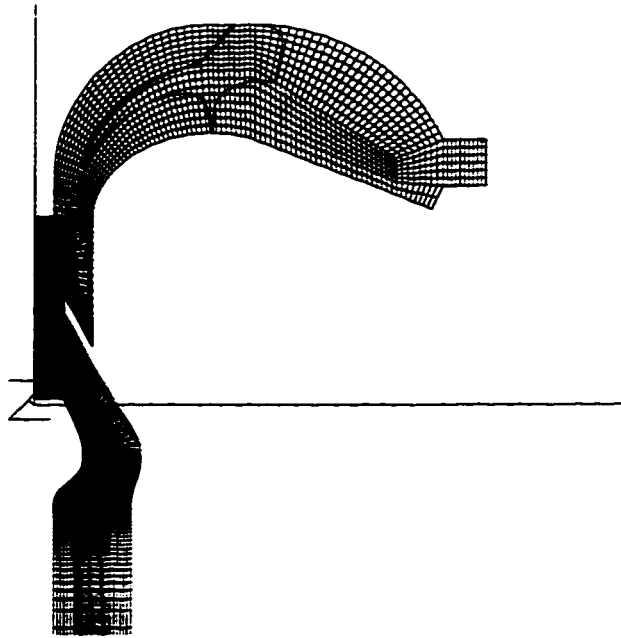


Figure 4.22. A cross sectional view of the base grid for the physiologically realistic throat model. The red lines indicate the approximate location of the grid lines used in the grid convergence studies.

approximately 600,000 nodes, representing a decrease and increase of approximately 50% in the nodal density respectively. Because of the complexity of the grid, it was difficult to find a continuous grid line through the entire flow field to use for the grid convergence studies. Instead, two separate lines are studied, the first begins in the mouthpiece, and passes through the mouth and pharynx and terminates on the superior surface of the epiglottis, and the second begins at the posterior wall of the pharynx and runs through the larynx and trachea. The approximate location of the lines are shown in Figure 4.22. Figures 4.23 and 4.24 compare the speed and pressure drop along the grid lines for the three grids, and it can be seen that the increase in accuracy of the high resolution grid is minimal.

4.7.2 Boundary conditions

The inlet boundary conditions used for this model are the same as for the USP model throat: plug velocity profile for 28.3 l/min, turbulence intensity of 0.12, and a turbulence length scale of 0.003 m. As with the USP model throat, the turbulence length scale was varied between 0.001 m and 0.01 m with no noticeable effect on the results. Decreasing the turbulence intensity also had little effect on the results, and all attempts to obtain converged solutions at higher turbulence intensities were unsuccessful.

4.7.3 Convergence

Iterative convergence was achieved when the RMS residuals over the entire flow field were all less than 7×10^{-8} . The maximum residual at any node was less than 2×10^{-6} indicating that there may be some areas of high error. Here, the maximum residuals are in a small recirculation region distal to the larynx on the posterior wall of the trachea. Most particles pass through this region close to the anterior wall of the trachea, so the impact of this error can be expected to be small.

The 'New Flow' summary is shown in Figure 4.25. Here it can be seen that in spite of the small RMS errors, the "Net Flow" is only 4 orders of magnitude less than the values at the boundaries.

Momentum and Mass Flow Summary				
Boundary or source	X-momentum	Y-momentum	Z-momentum	Mass
B.C. # 1, WALL	1.373E-03	3.229E-03	3.255E-07	0.000E+00
B.C. # 2, INFLOW	-1.378E-03	-1.352E-08	3.458E-10	5.480E-04
B.C. # 3, OUTFLOW	4.612E-06	-3.229E-03	-3.321E-07	-5.480E-04
Net Flow	-4.334E-07	-4.843E-08	-6.280E-09	1.572E-09

Figure 4.23. A summary table of the mass flows for the converged solution on the base grid used for the particle deposition calculations.

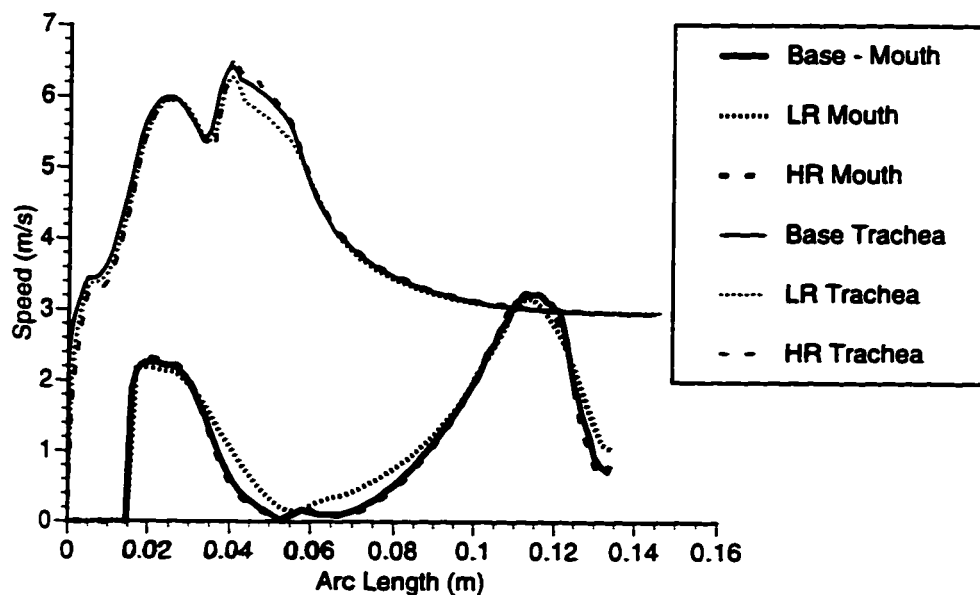


Figure 4.24. A plot of the speed of the fluid along the two grid lines for the three grid densities showing that increasing the grid resolution beyond the base grid does not increase the accuracy of the results. LR=low resolution. HR=high resolution.

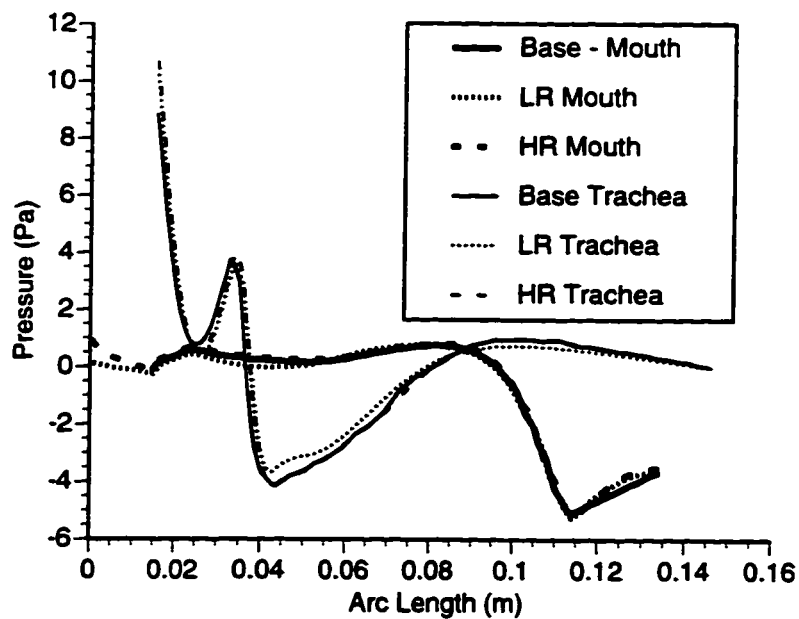


Figure 4.25. A plot of the pressure drop in the fluid along the two grid lines for the three grid densities showing that increasing the grid resolution beyond the base grid does not increase the accuracy of the results. LR=low resolution. HR=high resolution

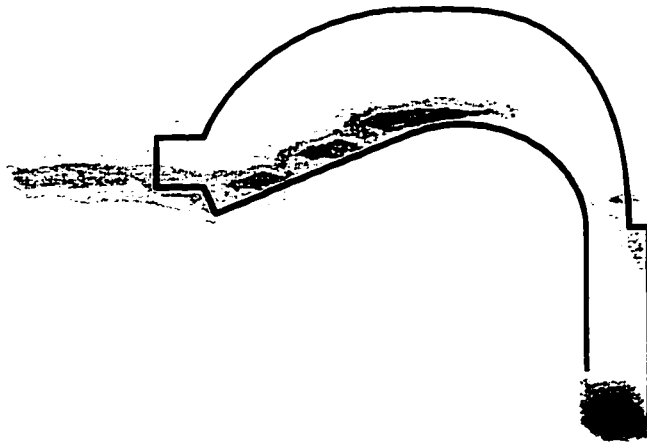


Figure 4.26. A greyscale image of the deposition of radiolabelled aerosol in the mouth and pharynx of the model throat. The deposition mainly occurs on the surface of the tongue and the bottom of the pharynx.

4.7.4 Experimental studies of aerosol deposition in the physiologically realistic throat model

A hand carved wooden model of the throat geometry was built and used as a form for a fiberglass model. The throat model was tested using the same technique as the USP model throat described in Section 4.6.4, and from Equation (4.10), it was determined that 21% of the mass entering the mouthpiece deposited on the walls of the model.

The pattern of deposition is shown in Figures 4.26 and 4.27. Approximately 30% of the aerosol which deposited in the model landed in the mouth, mainly on the tongue; 21% of the aerosol landed in the pharynx, with the most significant deposition on the inferior wall of the pharynx; and the remaining 49% deposited in the larynx (deposition on the superior surface of the epiglottis is considered part of the trachea).

The empirical equations given earlier in this thesis for deposition in the extrathoracic region of the respiratory tract provide a verification on both the experimental and computational results as they represent average values of extrathoracic deposition in actual subjects. Assuming a monodisperse aerosol with a particle diameter of $4.8\mu\text{m}$, a



Figure 4.27. A greyscale image of the deposition of radiolabelled aerosol in the larynx and trachea. The dark spot corresponds to the larynx. Significant deposition is also observed on the superior surface of the epiglottis.

flow rate of 28.3 l/min, and a tidal volume of 1 liter, a deposition fraction of 18.4% can be calculated with Equation (2.21). For a polydisperse aerosol with an MMD=4.8 and GSD=1.65, Equation (2.21) predicts that 25.6% of the aerosol should deposit.

4.7.5 Results

The deposition in the physiologically realistic throat was calculated using the same aerosols used with the USP model throat: a monodisperse aerosol with a diameter equal to the MMD of the aerosol produced by the nebulizer used in the experimental studies (4.8 μ m) and a polydisperse aerosol with an MMD and GSD equal to the values measured for the aerosol produced by the nebulizer used in the experimental studies (MMD of 4.8 μ m, and a GSD of 1.7).

The deposition as a percentage of the mass entering the mouthpiece is given in Table 4.2. In the previous section, it was noted that the average value of the extrathoracic deposition expected in actual subjects predicted by Equation (2.21) for a polydisperse

Region	Experimental Values	Monodisperse Aerosol	Polydisperse Aerosol
Mouth	6.4%	10.3%	20.0%
Pharynx	4.0%	8.9%	15.0%
Larynx/Trachea	7.6%	28.0%	29.8%
Total	21%	47.2%	64.8%

Table 4.2. Calculated total and regional deposition in the physiologically realistic throat model showing the effect of using a monodisperse vs. a polydisperse aerosol. All values are a percentage of total mass of aerosol entering.

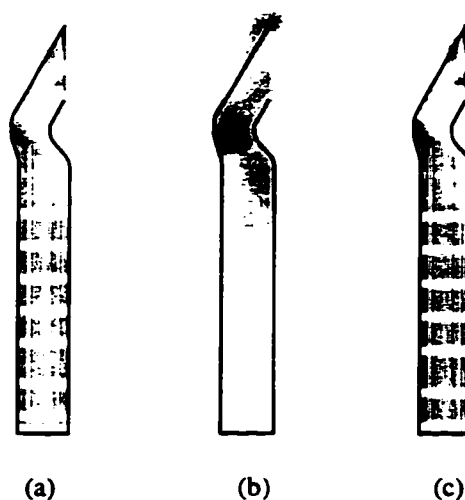


Figure 4.28. Calculated deposition pattern for the physiologically realistic throat model compared with the experimental results. (a) shows the deposition pattern in the trachea calculated using the monodisperse aerosol, (b) shows the experimental results (same data as Figure 4.27), and (c) shows the deposition pattern calculated using the polydisperse aerosol.

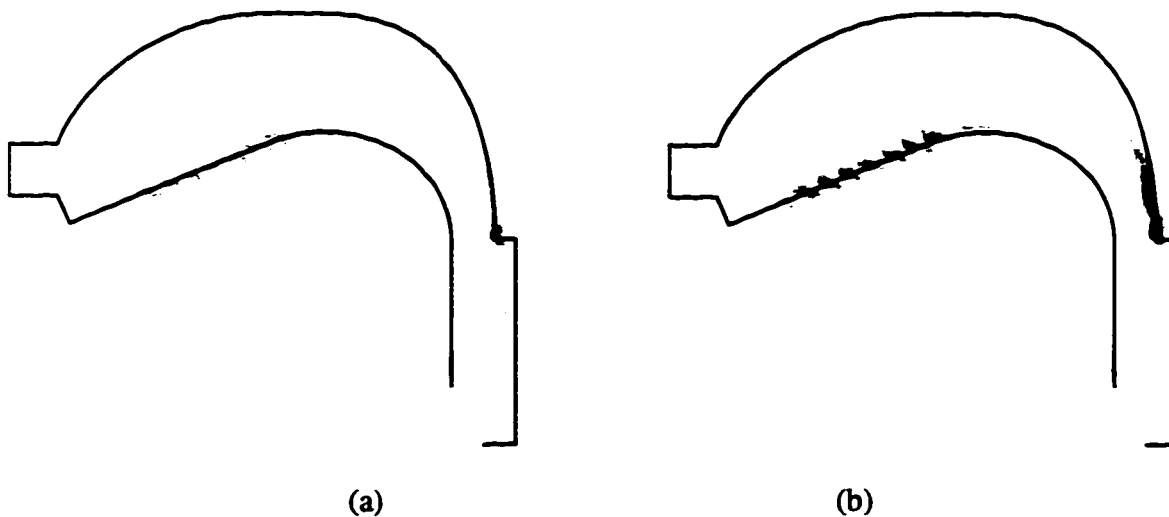


Figure 4.29. Calculated deposition pattern for the physiologically realistic throat model compared with the experimental results. (a) shows the deposition pattern calculated using the monodisperse aerosol, (b) shows the deposition pattern calculated using the polydisperse aerosol

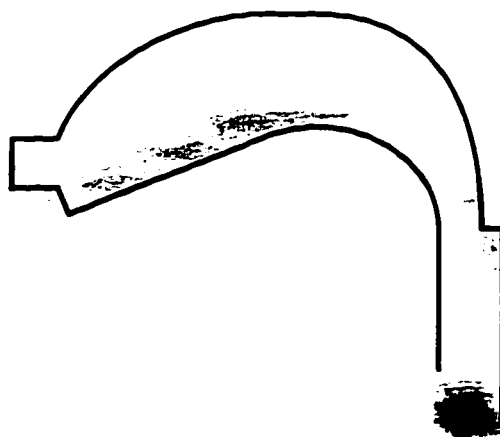


Figure 4.30. Experimental results of deposition in the mouth and pharynx. Same as Figure 4.26

aerosol (25%) is close to the experimentally determined deposition in the model (21%).

As was seen with the USP model throat, the calculated deposition is approximately twice the experimental value.

However, the deposition pattern predicted by the CFD is reasonably close to the experimentally observed pattern. Figures 4.29 4.30 compare the experimentally

determined deposition in the larynx/trachea with the computational results. It can be seen that the results for a polydisperse aerosol show reasonable agreement with the experimental patterns, with the most notable exception being that the CFD does not predict as much deposition on the bottom of the pharynx as was observed experimentally.

5. Conclusions

This manuscript has dealt with many of the issues involved in the study of drug delivery to the respiratory tract. Chapter 2 dealt with the development of a model that predicts the probability of a particle or droplet depositing in the different regions of the respiratory tract. Deposition due to sedimentation and diffusion are calculated from theoretical expressions for aerosol deposition in a system of randomly oriented tubes. Inertial impaction is calculated by an empirical expression matching the deposition in lung casts. Extrathoracic deposition is also calculated by an empirical expression.

The model also calculates the growth of droplets in response to their environment, and it was shown that one must consider not only the effect of their environment on the aerosol droplets, but also the effect of the aerosol droplets on their environment.

Here we have chosen to apply the deposition model to therapeutic aerosols generated by medical nebulizers, but in principle, it could be used for predicting the deposition of other devices, or in other applications. Indeed, a significant portion of the research in this area is supported by the occupational health and safety industry who are interested in the effects of human exposure to hazardous aerosol environments.

Chapter 3 characterized the output of medical nebulizers, and showed how this data can be used in conjunction with a deposition model to predict the actual dosage of medication delivered to the respiratory tract.

In developing a methodology for testing nebulizers so that a hygroscopic deposition model could be used to predict the pulmonary deposition, it was found that there are many factors that influence the drug delivered to the respiratory tract such as the droplet distribution, droplet number density, nebulizer mass output rate, ambient humidity and temperature, initial volume fill, initial solution concentration, and the design of the nebulizer itself (i.e. vented or unvented). To properly compare the output of nebulizers, all of these factors must be recorded or the value of the comparison is diminished. The method presented here accounts for all of these factors, and combines it with a sophisticated pulmonary deposition model to provide an estimate of the effectiveness of the nebulizer when used in a clinical setting.

The natural extension for this work is to develop a methodology for predicting the deposition of drugs formulated as suspensions, and drugs delivered by MDIs and DPIs. In both these cases, a major challenge will lie in measuring the output of the device correctly.

Overcoming the deficiencies in the deposition model presented here will most likely not be possible without a major shift in the current approach. One such approach is to use computational fluid dynamics (CFD). CFD has many attractive attributes, and is becoming increasingly accessible as a tool for researchers outside of traditional engineering areas.

Chapter 4 of this manuscript dealt with many of the issues involved in using CFD in the respiratory tract. A commercial code was tested on a variety of flows to investigate the usefulness of 'standard' CFD techniques for studying the flow and particle deposition in the respiratory tract. First, the particle deposition in tubes with simple 90° bends was studied, and it was found that the results duplicated both experimental the theoretical results available in the archival literature.

Next, a geometry similar to the USP model throat was investigated computationally and experimentally. Here, CFD did not perform well. The calculated filtering efficiencies were approximately twice the experimentally determined values. Further, the deposition pattern was not in close agreement. In the experimental results, the majority of the deposition occurred in the inlet tube, while the CFD predicted that most of the deposition would occur in a small ring where the exit tube joins the spherical elbow.

Finally, a novel throat model was described which closely approximated the shape of actual extrathoracic airways. The experimentally determined filtering efficiency of the model was similar to the deposition seen in actual throats. Again the filtering efficiencies calculated by the CFD were approximately twice the experimentally determined value. Here, the calculated deposition pattern more closely resembled the experimentally determined value with the exception that the CFD predicted less deposition on the bottom of the pharynx than was seen experimentally.

The reasons for the poor performance of the CFD are unclear. Since the predictions from the simple bent pipes with laminar flow show good agreement with experimental data, the turbulence model, and the implementation of turbulent dispersion are suspect.

Turbulence modeling is a complex subject, owing to its random nature, yet there is enough structure to turbulence that purely stochastic models do not perform well. Turbulence models perform adequately in flows for which they have been calibrated, mainly high Reynolds number and boundary layer flows. As was mentioned in Section 4.1, the flows seen in the USP model throat and the physiologically realistic throat have many characteristics (e.g. curved streamlines and recirculation regions) that are known to cause one and two-equation turbulence models to perform poorly. This may cause errors

in the mean streamlines. Additionally, it is unclear how particles themselves will affect the turbulence. Here, it is assumed that the particles do not affect the turbulence.

A Lagrangian trajectory model is used here to track particles through the turbulent field. The effect of turbulence on the particle tracks is modeled using an eddy lifetime model with the eddy characteristics calculated from the local turbulence quantities. This approach has a number of difficulties. First, the calculated turbulent field is approximate (and may be in error due to the turbulence model), and turbulent fluctuations chosen by Equation (4.3) will not satisfy the continuity equation for velocity fluctuations, hence, the flow field used in the particle trajectory calculations may be unphysical. Secondly, in the calculation of the particle trajectories, the turbulence is simulated using a single eddy size, when particles in these flows will actually be influenced by eddies with sizes differing by an order of magnitude. Again, as with turbulence models, these methods for calculating particle trajectories in turbulent flows work well for a narrow range of flows for which they are calibrated (e.g. single particles in homogeneous grid turbulence).

Overcoming these shortcomings may be possible by using more advanced turbulence models such as Large Eddy Simulation (LES) where some of the turbulence is simulated directly. It may then be possible to use some of this information in the particle trajectory calculations to improve their accuracy as well.

In summary, CFD shows promise for calculating the particle deposition in laminar flow, or those flows where turbulent dispersion is not important. However, using current CFD programs with turbulent dispersion can result in serious errors.

6. References

- Altshuler B. (1959). Calculation of regional deposition of aerosol in the respiratory tract. *Bulletin of Mathematical Biophysics*. **21**: 257-270.
- Alvine G.FI, Rodgers P., Fitzsimmons K.M., and Agrens R.C. (1992). Disposable nebulizers: How reliable are they? *Chest*. **101**(2): 316-319.
- Anderson J.D. (1995). *Computational Fluid Dynamics*. McGraw-Hill, New York.
- Baer T., Gore J.C., Gracco L.C., and Nye P.W. (1991). Analysis of vocal tract shape and dimensions using magnetic resonance imaging: Vowels. *Journal of the Acoustical Society of America*. **90**(2): 799-828.
- Balàshàzy I., Martonen T.B., and Hofmann W. (1990). Inertial impaction and gravitational deposition of aerosols in curved tubes and airway bifurcations. *Aerosol Science and Technology*. **13**: 308-321.
- Balàshàzy I., Hofmann W., and Martonen T.B. (1991). Inspiratory particle deposition in airway bifurcation models. *Journal of Aerosol Science*. **22**(1): 15-30.
- Balàshàzy I., and Hofmann W. (1993). Particle deposition in airway bifurcations - I. Inspiratory flow. *Journal of Aerosol Science*. **24**(6): 745-772.
- Bennett W.D. (1988). Human variation in spontaneous breathing deposition fraction: A review. *Journal of Aerosol Medicine*. **1**(2): 67-80.
- Berlemont A., Desjonqueres P., and Gouesbet G. (1990). Particle lagrangian simulation in turbulent flows. *International Journal of Multiphase Flow*. **16**(1): 19-34.
- Blake K.V., Hoppe M., Harman E., and Hendeles L. (1992). Relative amount of albuterol delivered to lung receptors from a metered-dose inhaler and nebulizer solution. *Chest*. **101**(2): 309-315.
- Brancatisano T., Collett P.W., and Engel L.A. (1983). Respiratory movements of the vocal cords. *Journal of Applied Physiology*. **54**(5): 1269-1276.

- Brockmann J.E. (1993). Sampling and transport of aerosols. In: *Aerosol Measurement: Principles, Techniques, and Applications*. (Eds. K. Willeke & P.A. Baron). Van Nostrand Reinhold, New York, NY, p77-111.
- Cai F.S., and Yu C.P. (1988). Inertial and interceptional deposition of spherical particles and fibres in a bifurcating airway. *Journal of Aerosol Science*. **19**(6): 679-688.
- Chan T.L., and Lippmann M. (1980). Experimental measurements and empirical modelling of the regional deposition of inhaled particles in humans. *American Industrial Hygiene Association Journal*. **41**: 399-409.
- Chan H.K., Phipps P.R., Gonda I., Cook P., Fulton R., Young I., and Bautovich G. (1994). Regional deposition of nebulized hypodense nonisotonic solutions in the human respiratory tract. *European Respiratory Journal*. **7**: 1483-1489.
- Chang H.K., and Masry O.A. (1982) A model study of flow dynamics in human central airways. Part I: Axial velocity profiles. *Respiration Physiology*. **49**: 75-95.
- Chang H.K., & Menon A.S. (1993). Airflow dynamics in the human airways. In: *Aerosols in Medicine: Principles, Diagnosis, and Therapy*. (Eds. F. MorEn, M.B. Dolovich, M.T. Newhouse, and S.P. Newman) Elsevier Science. London. p. 85-117.
- Cheng Y.S., & Wang C.S. (1975). Inertial deposition of particles in a bend. *Journal of Aerosol Science*. **6**: 139-145.
- Cinkotai F.F. (1971). The behavior of sodium chloride particles in moist air. *Journal of Aerosol Science*. **2**: 325-329.
- Cipolla D.C., Clark A.R., Chan H.K., Gonda I., and Shire S.J. (1994). Assessment of aerosol delivery systems for recombinant human deoxyribonuclease. *STP Pharma Sciences*. **4**(1): 50-62.
- Clark A.R. (1995). The use of laser diffraction for the evaluation of the aerosol clouds generated by medical nebulizers. *International Journal of Pharmaceuticals*. **115**: 69-78.
- Clay M.M., Pavia D., Newman S.P., Lennard-Jones T., and Clarke S.W. (1983). Factors influencing the size distribution of aerosols from jet nebulizers *Thorax*. **38**: 755-759.
- Cohen B.S., Sussman R.G., and Lippmann, M. (1990). Ultrafine particle deposition in a human tracheobronchial cast. *Aerosol Science and Technology*. **12**: 1082-1091.
- Cole P. (1953). Further observations on conditioning of respiratory air. *Journal of Laryngol. Otol.* **67**: 669-681.
- Consensus Conference on Aerosol Delivery. (1991). Aerosol Consensus Statement. *Chest* **100**: 1106-1109.
- Crane R.I., & Evans R.L. (1977). Inertial deposition of particles in a bent pipe. *Journal of Aerosol Science*. **8**: 161-170.

- Cranston W.I., Gerbrandy J., and Snell E.S. (1954). Oral, rectal and esophageal temperatures and some factors affecting them in man. *J Physiol London*. **126**: 347-358.
- Crowe C.T., Troutt, T.R., and Chung J.N. (1996). Numerical models for 2 phase turbulent flows. *Annual Review of Fluid Mechanics*. **28**: 11-43.
- Davies C.N. (1982). Deposition of particles in the Human Lungs as a function of particle size and breathing pattern: An empirical model. *Annals of Occupational Hygiene*. **26**(1-4): 119-135.
- Daviskas E., Gonda I., and Anderson S.D. (1990) Mathematical modeling of heat and water transport in human respiratory tract. *Journal of Applied Physiology*. **69**(1): 362-372.
- Dekker E. (1961). Transition between laminar and turbulent flow in human trachea. *Journal of Applied Physiology*. **16**(6): 1060-1064.
- Diu C.K., & Yu C.P. (1980). Deposition from charged aerosol flows through a pipe bend. *Journal of Aerosol Science*. **11**: 397-402.
- Egan M.J., and Nixon W. (1985). A model of aerosol deposition in the lung for use in inhalation dose assessments. *Radiation Protection Dosimetry*. **11**(1): 5-17.
- Eisner A.D., Graham R.C., and Martonen T.B. (1990). Coupled mass and energy transport phenomena in aerosol/vapour-laden gasses - I. Theory of the hygroscopic aerosol effects on temperature and relative humidity patterns of inspired air. *Journal of Aerosol Science*. **21**(7): 833-848.
- Emmett, P.C., Aitken, R.J., and Hannan, W.J. (1972). Measurements of the Total and Regional Deposition of Inhaled Particles in the Human Respiratory Tract, *Journal of Aerosol Science*. **13**(6): 549-560.
- Ferron G.A. (1977). The size of soluble aerosol particles as a function of the humidity of the air. Application to the human respiratory system. *Journal of Aerosol Science*. **8**: 251-267.
- Ferron G.A., Haider B., and Kreyling W.G. (1985a). A method for the approximation of the relative humidity in the upper human airways. *Bulletin of Mathematical Biology*. **47**(4): 565-589.
- Ferron G.A., Hornik S., Kreyling W.G., and Haider B. (1985b). Comparison of experimental and calculated data for the total and regional deposition in the human lung. *Journal of Aerosol Science*. **16**(2): 133-143.
- Ferron G.A., and Gebhart J. (1988). Estimation of the lung deposition of aerosol particles produced with medical nebulizers. *Journal of Aerosol Science*. **21**(3): 1083.
- Ferron G.A., Haider B., and Kreyling W.G. (1988a). Inhalation of salt aerosol particles - I. Estimation of the temperature and relative humidity of the air in the upper human airways. *Journal of Aerosol Science*. **19**(3): 343-363.

- Ferron G.A., Kreyling W.G., and Haider B. (1988b). Inhalation of salt aerosol particles - II. Growth and deposition in the human respiratory tract. *Journal of Aerosol Science*. **19(5)**: 611-631.
- Ferron G.A., and Soderholm S.C. (1990). Estimation of the times for evaporation of pure water droplets and for stabilization of salt solution particles. *Journal of Aerosol Science*. **21(3)**: 415-429.
- Ferron G.A., and Eisner D.A. (1996). Numerical simulation of air and particle transport in the conducting airways. *Journal of Aerosol Medicine*. **9(3)**: 303-316.
- Ferron G.A., Roth C., Busch B., and Karg E. (1997). Estimation of the size distribution of aerosols produced by jet nebulizers as a function of time. *Journal of Aerosol Science*. In Press.
- Findeisen W. (1935). über das Absetzen kleiner in der Luft Suspendierter Teilchen in der Menschlichen Lunge Bei der Atmung. *Pfluegers Arch*. **236**: 367-379.
- Finlay W.H., and Stapleton K.W. (1995). The effect on regional lung deposition of coupled heat and mass transfer between hygroscopic droplets and their surrounding phase. *Journal of Aerosol Science*. **26(4)**: 655-670.
- Finlay W.H., and Stapleton K.W. (1996). Are hygroscopic effects important in determining lung deposition of nebulized pharmaceutical aerosols? *Respiratory Drug Delivery V*. (Eds. R.N. Dalby, P.R. Byron, S.J. Farr) Interpharm Press, Buffalo Grove IL.
- Finlay W.H., Stapleton K.W., and Yokota J. (1996a). On the use of computational fluid dynamics for simulating flow and particle deposition in the human respiratory tract. *Journal of Aerosol Medicine*. **9(3)**: 329-341.
- Finlay W.H., Stapleton K.W., Chan H.K., Zuberbuhler and Gonda I. (1996b). Regional deposition of inhaled hygroscopic aerosols: in vivo SPECT compared with mathematical modelling. *Journal of Applied Physiology*. **81(1)**: 374-383.
- Finlay W.H., Stapleton K.W., and Zuberbuhler (1997a). Variations in regional lung deposition of salbutamol sulphate between 19 nebulizer models. Submitted to: *Pharmaceutical Science*.
- Finlay W.H., Stapleton K.W., and Zuberbuhler (1997b). Inhaled fine particle fraction as a measure of lung dosage for the inhalation of nearly isotonic nebulizer aerosols. Submitted to: *Journal of Aerosol Science*
- Finlay W.H., Stapleton K.W., and Zuberbuhler P. (1997b). Inhaled fine particle fraction as a measure of lung dosage for the inhalation of nearly isotonic nebulized aerosol. submitted to *Journal of Aerosol Science*.
- Finlay W.H. Stapleton K.W., and Zuberbuhler P. (1997c). Errors in regional lung deposition predictions of nebulized salbutamol sulphate due to neglect or partial inclusion of hygroscopic effects. *Journal of Aerosol Medicine*. In Press.

- Fletcher C.A.J. (1991). *Computational Techniques for Fluid Dynamics. Volume I and II.* Springer Verlag, Berlin.
- Foord, N., Black, A., and Walsh, M. (1978). Regional Deposition of 2.5-7.5 μm Diameter Inhaled Particles in Healthy Male Non-smokers, *Journal of Aerosol Science*. **9**: 343-357.
- Fuchs N.A. (1959). *Evaporation and Droplet Growth in Gaseous Media.* Pergamon Press, London.
- Fuchs N.A. (1964) *The Mechanics of Aerosols.* Dover Publications Inc. New York, NY.
- Gawronski R., and Szewczyk K.W. (1986). Inertial deposition of particles in the human branching airways. *Journal of Aerosol Science*. **17**(5): 795-801.
- Gebhart J., Heigwer G., Heyder J., Roth C., and Stahlhofen W. (1989). The use of light scattering photometry in aerosol medicine. *Journal of Aerosol Medicine*. **1**(2): 89-112.
- Gebhart J., Anselm A., Ferron G., Heyder J., and Stahlhofen W. (1990). Experimental data on total deposition of hygroscopic particles in the human respiratory tract. *Aerosols Science, Industry, Health, and Environment*. p. 1299-1302.
- Gehr P., Schürch S., Berthiaume Y., Im Hof V., and Geiser M. (1990). Particle retention in airways by surfactant. *Journal of Aerosol Medicine*. **3**(1): 27-43.
- Gehr P., Green F.H.Y., Geiser M., Im Hof V., Lee M.M., and Schürch S. (1996). Airway surfactant, a primary defense barrier: Mechanical and immunological aspects. *Journal of Aerosol Medicine*. **9**(2): 163-181.
- Giacomelli-Maltoni, G., Melandri, C., Prodi, V., and Tarroni, G. (1972). Deposition Efficiency of Monodisperse Particles in Human Respiratory Tract. *American Industrial Hygiene Association Journal* **33**: 603-610.
- Glansdorff P., & Prigogine I. (1971). *Thermodynamic Theory of Structure, Stability, and Fluctuations.* Wiley, New York, NY.
- Goldberg I.S., & Lourenço R.V. Deposition of Aerosols in Pulmonary Disease. *Archives of Internal Medicine*. **131**: 88-91 (1973).
- Gormley P.G., and Kennedy K. (1949). Diffusion from a stream flowing through a cylindrical tube. *Proceedings of the Royal Irish Society*. **52A**: 163.
- Graham R.C., & Eisner A.D. (1990). Coupled mass and energy transport phenomena in aerosol/vapour laden gasses II. Computer modelling of water vapour/droplet interaction and entrainment. *Journal of Aerosol Science*. **21**: 849.
- Gurman J.L., Lippmann M., and Schlesinger R.B. (1984). Particle deposition in replicate casts of the human upper tracheobronchial tree under constant and cyclic inspiratory flow. I. Experimental. *Aerosol Science and Technology*. **3**: 245-252.
- Haefeli-Bleuer B., & Weibel E.R. Morphometry of the Human Pulmonary Acinus. *Anatomical Record*. **220**: 401-414, 1988.

- Hanna M.L. & Scherer P.W. A theoretical model of localized heat and water vapour transport in the human respiratory tract. *Journal of Biomechanical Engineering*. **108**: 19-27, 1986.
- Hansen J.E. & Ampaya E.P. (1975). Human air space shapes, sizes, areas, and volumes. *Journal of Applied Physiology*. **38(6)**: 990-995.
- Heidenreich S. (1994). Condensational droplet growth in the continuum regime - A critical review for the system air-water. *Journal of Aerosol Science*. **25**: 49.
- Heidenreich S., and Büttner H. (1995). Investigations about the influence of the Kelvin effect on droplet growth rates. *Journal of Aerosol Science*. **26(2)**: 335-339.
- Heistracher T., & Hofmann W. (1995). Physiologically realistic models of bronchial airway bifurcations. *Journal of Aerosol Science*. **26(3)**: 497-509.
- Heyder J., Armbruster L., Gebhart J., Grein E., and Stahlhofen W. (1975). Total deposition of aerosol particles in the human respiratory tract for nose and mouth breathing. *Journal of Aerosol Science*. **6**: 311-328.
- Heyder J., Gebhart J. (1977). Gravitational deposition of particles from laminar aerosol flow through inclined circular tubes. *Journal of Aerosol Science*. **8**: 289-295.
- Heyder, J., Gebhart, J., Roth, C., Stahlhofen, W., Stuck, B., Tarroni, G., DeZaiacomo, T., Formignani, M., Melandri, C., and Prodi, V. (1978), Intercomparison of Lung Deposition Data for Aerosol Particles, *Journal of Aerosol Science*. **9**: 147-155.
- Heyder, J., Gebhart, J., Stahlhofen, W., and Stuck, B. (1982). Biological Variability of Particle Deposition in the Human Respiratory Tract During Controlled and Spontaneous Mouth-breathing, *Annals of Occupational Hygiene*. **26(1)**: 137-147.
- Heyder J., and Rudolf G. (1984). Mathematical models of particle deposition in the human respiratory tract. In: *Lung Modelling for Radioactive Materials*. (Eds. H. Smith & G. Gerber) EUR 9384 EN. Commission of the European Communities, Luxembourg. p. 17-38.
- Heyder J., Gebhart J., Rudolf G., Schiller C.F., and Stahlhofen W. (1986). Deposition of particles in the human respiratory tract in the size range 0.005-15 μm . *Journal of Aerosol Science*. **17(5)**: 811-825.
- Heyder J., Gebhart J., and Scheuch G. (1988a). Influence of human lung morphology on particle deposition. *Journal of Aerosol Medicine*. **1(2)**: 81-88.
- Heyder J., Blanchard J.D., Feldman H.A., and Brain J.D. (1988b). Convective mixing in human respiratory tract: Estimates with aerosol boli. *Journal of Applied Physiology*. **64**: 1273-1278.
- Hiller F.C. (1991). Health implications of hygroscopic particle growth in the human respiratory tract. *Journal of Aerosol Medicine*. **4**: 1.

- Hofmann W., & Balàshàzy I. (1991). Particle deposition patterns within airway bifurcations - solution of the 3D Navier-Stokes equations. *Respiration Protection Dosimetry*. **38(1/3)**: 57-63.
- Horsfield K., & Cumming G. (1969). Angles of Branching and Diameters of Branches in the Human Bronchial Tree. *Bulletin of Mathematical Biophysics*. **29**: 245-259.
- Hughes J.M.B., Hoppin Jr. F.G., and Mead J. (1972). Effect of lung inflation on bronchial length and diameter in excised lungs. *Journal of Applied Physiology*. **32(1)**: 25-35.
- ICRP (International Commission on Radiological Protection) (1994). Human Respiratory Tract Model for Radiological Protection. *Annals of the ICRP* **24(1-3)**. Elsevier Science Inc. Tarrytown, NY.
- Ilowite J.S., Baskin M.I., Sheetz M.S., and Abd A.G. (1989). Delivered dose and regional distribution of aerosolised Pentamidine using different delivery systems. *Chest*. **99(5)**: 1139-1144.
- Incropera F.P., and DeWitt D.P. (1990). *Introduction to Heat Transfer*. John Wiley & Sons, New York.
- Ingenito E.P., Solway J., McFadden E.R., Pichurko B.M., Cravalho E.G., and Drazen J.M. (1986). Finite difference analysis of respiratory heat transfer. *Journal of Applied Physiology*. **61(6)**: 2252-2259.
- Ingram D.B. (1975). Diffusion of aerosols from a stream flowing through a cylindrical tube. *Journal of Aerosol Science*. **6**: 125-132.
- Isabey D., & Chang H.K. (1982). A model study of flow dynamics in human central airways. Part II: Secondary flow velocities. *Respiration Physiology*. **49**: 97-113.
- Jaeger M.J., & Matthys H. (1969). The pattern of flow in the upper human airways. *Respiration Physiology*. **6**: 113-127.
- Johnston J.R., & Muir D.C.F. (1973). Inertial deposition of particles in the lung. *Journal of Aerosol Science*. **4**: 269-270.
- Johnston J.R., Isles K.D., and Muir D.C.F. (1977). Inertial deposition of particles in human branching airways. In: *Inhaled Particles IV*. (ed. Walton W.H.). Pergamon Press, Oxford, p. 61-73.
- Johnson M.A., Newman S.P., Bloom R., Talaei N., and Clarke S.W. (1989). Delivery of Albuterol and Ipratropium Pentamidine using different delivery systems. *Chest*. **96(1)**: 6-10.
- Katz I.M., & Martonen T.B. (1996a). Flow patterns in three-dimensional laryngeal models. *Journal of Aerosol Medicine*. **9(4)**: 501-512.

- Katz I.M., & Martonen T.B. (1996b). Three-dimensional fluid particle trajectories in the human larynx and trachea. *Journal of Aerosol Medicine*. 9(4): 531-520.
- Kays W.M., and Crawford M.E. (1980). *Convective Heat and Mass Transfer*. Wiley, New York.
- Kim C.S., and Iglesias A.J. (1989). Deposition of inhaled particles in bifurcating airway models: I. Inspiratory deposition. *Journal of Aerosol Medicine*. 2(1): 1-14.
- Kim C.S., Iglesias A.J., and Garcia L. (1989). Deposition of inhaled particles in bifurcating airway models: II. Expiratory deposition. *Journal of Aerosol Medicine*. 2(1): 15-27.
- Kim C.S., Fisher D.M., Lutz D.J., and Gerrity T.R. (1994). Particle deposition in bifurcating airway models with varying airway geometry. *Journal of Aerosol Science*. 25(3): 567-581.
- Knoch M. & Wunderlich E. (1994). In vitro assessment of a new efficient nebulizer system for continuous operation. In: *Respiratory Drug Deliver IV*. Interpharm Press Inc. Buffalo Grove IL. 60089.
- Landahl H.D., & Herman R.G. (1949). Sampling of liquid aerosols by wires, cylinders, and slides, and the efficiency fo impaction of the droplets. *Journal of Colloid Science*. 4: 103-136.
- Landahl H.D. (1950). On the removal of air-borne droplets by the human respiratory tract: I. The lung. *Bulletin of Mathematical Biophysics*. 12: 43-56.
- Langford S.A., and Allen M.B. (1993). Salbutamol output from two jet nebulizers. *Respiratory Medicine*. 87: 99-103.
- Lippman, M., and Albert, R.E. (1969). The Effect of Particle Size on the Regional Deposition of Inhaled Aerosols in the Human Respiratory Tract. *American Industrial Hygiene Association Journal*. 30: 357-375.
- Lippmann M. (1977). Regional deposition of particles in the human respiratory tract. *Handbook of Physics - Section 9: Reactions to Environmental Agents* (Lee D.H.K., Falk H.L., and Murry S.D. eds) American Physiological Society, Bethesda, MD, USA, pp212-232.
- Lippmann, M., Yeates, D.B., and Albert, R.E. (1980). Deposition, retention, and clearance of inhaled particles. *British Journal of Industrial Medicine*. 37: 337-362.
- Loffert D.T., Ikle D., and Nelson H.S. (1994). Comparison of commercial nebulizers. *Chest*. 106: 1788-1793.
- Logus J.W., Trajan M., Hooper H.R., Lentle B.C., and Man S.F.P. (1984). Single photon emission tomography of lungs imaged with 99mTc-labeled aerosol. *Journal of the Canadian Association of Radiologists*. 35: 99-103.

Lourenço, R.V., Klimek, M.F., Borowski, C.J. (1971). Deposition and Clearance of 2 μ m Particles in the Tracheobronchial Tree of Normal Subjects - Smokers and Nonsmokers, *Journal of Clinical Investigation*. **50**: 1411-1420.

Lowe A.A. (1990). The Tongue and Airway. *Otolaryngologic Clinics of North America*. **23**(4): 677-698.

Lowe A.A., & Fleetham J.A. (1991). Two- and Three-dimensional Analyses of Tongue, Airway, and Soft Palate Size. In: *Atlas of the Difficult Airway*. (Norton M.L., & Brown A.C.D. eds) Mosby Year Book, pp 74-82.

Lowe A.A. (1994). Personal communication.

Martonen, T.B., Bell, K.A., Phalen, R.F., Wilson, A.F., and Ho, A. (1982). Growth Measurements and Deposition Modeling of Hygroscopic Aerosols in Human Tracheobronchial Models. *Annals of Occupational Hygiene*. **26**(1): 93-108.

Martonen T.B. (1983). On the fate of inhaled particles in the human: a comparison of experimental data with theoretical computations based on a symmetric and asymmetric lung. *Bull Math Biol*. **45**(3): 409-424.

Martonen T.B. & Lowe J. (1983). Assessment of aerosol deposition patterns in human respiratory tract casts. In: *Aerosols in the Mining and Industrial Work Environments, Vol 1: Fundamentals and Status*. (Eds. V.A. Marple and B.Y.G. Liu). Ann Arbor Science Publishers, Ann Arbor MI. p. 151-164.

Martonen T.B., Yang Y. and Xue Z.Q. (1993). Influences of cartilaginous rings on tracheobronchial fluid dynamics. *Inhalation Toxicology*. **6**: 185-203.

Mason B.J. (1971). *The Physics of Clouds*. 2nd Edition, Clarendon Press, Oxford.

Matthys H. and Köhler D. (1985). Pulmonary deposition of aerosols by different mechanical devices. *Respiration*. **48**: 269-276.

Maxey M.R., and Riley J.J. (1983). Equation of motion for a small rigid sphere in a nonuniform flow. *Physics of Fluids*. **26**(4): 883-889.

McFadden E.R., Pichurko B.M., Bowman H.F., Ingenito E., Burns S., Dowling N., and Solway J. (1985). Thermal mapping of the airways in humans. *Journal of Applied Physiology*. **58**(2): 564-570.

Mercer T.T., Tillery M.I., and Chow H.Y. (1968). Operating characteristics of some compressed-air nebulizers. *American Industrial Hygiene Journal*. **29**: 66-78.

Mercer T.T. (1981). Production of therapeutic aerosols. *Chest*. **80**(6): 813-817.

Miller J.A., Pereira J.C., and Thomas D.W. (1989). Fluid flow through the larynx channel. *Journal of Sound and Vibration*. **121**(2): 277-290.

Morris A.H. (1993). *NSWC library of mathematics software*. Naval Surface Warfare Center (Dahlgren Division, Dahlgren, Virginia) Technical Report 92 (NSWCDD/TR-92/425).

Morrow P.E. (1974). Aerosol Characterization and Deposition. *American Review of Respiratory Diseases*. **110**: 88-.

Morrow P.E. (1986). Factors determining hygroscopic aerosol deposition in airways. *Physiological Reviews*. **66**(2): 330-376.

Morrow, P.E., and Yu, C.P. (1993). Models of aerosol behavior in airways and alveoli. *Aerosols in Medicine, Principles, Diagnosis and Therapy* (MorÈn F., Dolovich M.B., Newhouse M.T., and Newman S.P eds) Elsevier Science Publishers B.V. pp. 157-193.

Newman S.P., Pellow P.G.D., and Clarke S.W. (1986). Choice of Nebulizers and compressors for delivery of carbenicillin aerosol. *European Journal of Respiratory Disease*. **69**: 160-168.

O'Callaghan C., Clarke A.R., and Milner A.D. (1989). Inaccurate calculation of drug output from nebulizers. *European Journal of Pediatrics*. **148**: 473-474.

Olson D.E., Dart G.A., and Filley G.F. (1970). Pressure drop and fluid flow regime of air inspired into the human lung. *Journal of Applied Physiology*. **28**(4): 482-494.

Olson D.E. (1972). *Fluid Mechanics relevant to respiration - Flow within Curved Channels and Elliptical Tubes and Bifurcating Systems*. (PhD thesis) University of London.

Olson D.E., Sudlow M.F., Horsfield K., and Filley G.F. (1973). Convective patterns of flow during inspiration. *Archives of Internal Medicine*. **131**: 51-57.

Pack A., Hooper M.B., Nixon W., and Taylor J.C. (1972). A computational model of pulmonary gas transport incorporating effective diffusion. *Respiration Physiology*. **29**: 101-124.

Pae E.-K., Lowe A.A., Sasaki K, Price C., Tsuchiya M., and Fleetham J.A. (1994). A cephalometric and electromyographic study of upper airway structures in the upright and supine positions. *American Journal of Orthodontics and Dentofacial Orthopedics*. **106**(1): 52-59.

Panton R.L. (1984). *Incompressible Flow*. John Wiley & Sons, New York.

Patel V.C., Rodi W., and Scheuerer G. (1985). Turbulence models for near-wall and low Reynolds number flows: A review. *AIAA Journal*. **23**(9): 1308-1319.

Pedley T.J. (1977). Pulmonary Fluid Dynamics. *Annual Reviews of Fluid Mechanics*. **9**: 229-274.

Persons D.D., Hess G.D., Muller W.J., Scherer P.W. (1987). Airway deposition of hygroscopic heterodispersed aerosols: results of a computer calculation. *Journal of Applied Physiology*. **63**(3): 1195-1204.

Phipps P.R., Gonda I., Bailey D.L., Borham P., Bautovich G., and Anderson S.D. (1989) Comparisons of planar and tomographic gamma scintigraphy to measure the penetration index of inhaled aerosols. *American Review of Respiratory Disease*. **139**: 1516-1523.

Phipps P.R. and Gonda I. (1990). Droplets produced by medical nebulizers. *Chest*. **97**: 1327.

Phipps P.R., Gonda I., Anderson S.D., Bailey D., and Bautovich G. (1994). Regional deposition of saline aerosols of different tonicities in normal and asthmatic subjects. *European Respiratory Journal*. **7**: 1474-1482.

Pich J. (1972). Theory of gravitational deposition of particles from laminar flows in channels. *Aerosol Science*. **3**: 351-361.

Prakash C., and Patankar S.V. (1985). A control volume-based finite-element method for solving the Navier-Stokes equations using equal-order velocity-pressure interpolation. *Numerical Heat Transfer*. **8**: 259-280.

Prokop R.M., Finlay W.H., and Stapleton K.W. (1995). An in vitro technique for calculating the regional dosages of drugs delivered by an ultrasonic nebulizer. *Journal of Aerosol Medicine*. **26**(5): 847-860.

Prokop R.M., Finlay W.H., Stapleton K.W., and Zuberbuhler P. (1995). The effect of ambient relative humidity on regional dosages delivered by a jet nebulizer. *Journal of Aerosol Medicine*. **8**(4): 363-374.

Reid R.C., Prausnitz J.M., and Sherwood T.K. (1977). *Properties of Gases and Liquids*. McGraw-Hill, New York.

Rodenstein D.O., Doms G., Thomas Y., Listro G., Stanescu D.C., Culée C., and Aubert-Tulkens G. (1990). Pharyngeal shape and dimensions in healthy subjects, snorers, and patients with obstructive sleep apnoea. *Thorax*. **45**: 722-727.

Rudolf G., Köbrich R., and Stahlhofen W. (1990). Modelling and algebraic formulation of regional aerosol deposition in man. *Journal of Aerosol Science*. **21**(S1): S403-S406.

Saidel G.M., Kruse K.L., and Primiano, Jr. F.P. (1983). Model simulation of heat and water transport dynamics in an airway. *Journal of Biomechanical Engineering*. **105**: 188-193.

Scherer R.C., and Titze I.R. (1983). Pressure-flow relationships in a model of the laryngeal airway with a diverging glottis. In: *Vocal Fold Physiology: Contemporary Research and Clinical Issues*. (Eds. D.M. Bless and J.H. Abbs). College Hill Press. San Diego, p. 179-193.

- Schlesinger R.B. and Lippmann M. (1972). Particle deposition in casts of the human upper tracheobronchial tree *American Industrial Hygiene Association Journal*. **33**: 237-251.
- Schlesinger R.B., Bohning D.E., Chan T.L., and Lippmann M. (1977). Particle deposition in a hollow cast of the human tracheobronchial tree. *Journal of Aerosol Science*. **8**: 429-445.
- Schroter R.C., & Sudlow M.F. (1969). Flow patterns in models of the human bronchial airways. *Respiration Physiology*. **7**: 341-355.
- Shadle C.H. (1996). The aerodynamics of speech. In: *Handbook of Phonetics*. (Eds. W.J. Hardcastle & J. Laver) Blackwells.
- Smaldone, G.C., Perry, R.J., Bennett, W.D., Messina, M.S., Zwang, J., and Ilowite J. (1988). Interpretation of '24 hour lung retention' in studies of mucociliary clearance. *Journal of Aerosol Medicine*. **1**: 11-16.
- Smye S.W., Jollie M.I., and Littlewood J.M. (1991). A mathematical model of some aspects of jet nebulizer performance. *Clin. Phys. Physiol. Meas.* **12**(3): 289-300.
- Smye S.W., Jollie M.I., Cunliffe H., and Littlewood J.M. (1992). Measurement and prediction of drug solvent losses by evaporation from a jet nebulizer. *Clin. Phys. Physiol. Meas.* **13**(2): 129-134.
- Sorokin V.N. (1992). Determination of vocal tract shape for vowels. *Speech Communication*. **11**: 71-85.
- Stahlhofen, W., Gebhart, J., and Heyder, J. (1981). Biological variability of regional deposition of aerosol particles in the human respiratory tract. *American Industrial Hygiene Association Journal*. **42**: 348-352.
- Stahlhofen W., Gebhart J., Rudolf G., and Scheuch G. (1987). Retention of radioactively labelled Fe₂O₃ particles in the human lungs. *Deposition and Clearance of Aerosols in the Human Respiratory Tract*. (Ed. W. Hoffmann). Facultas Universitätsverlag, Vienna, Austria.
- Stahlhofen, W., Rudolf, G., and James, A.C. (1989). Intercomparison of Experimental Regional Aerosol Deposition Data. *Journal of Aerosol Medicine*. **2**(3): 285-308.
- Stanescu D.C., Pattijn J., Clément J., and van de Woestijne K.P. (1972). Glottis opening and airway resistance. *Journal of Applied Physiology*. **32**(4): 460-466.
- Stapleton K.W. & Finlay W.H. (1997). Errors in measuring nebulized particle size distributions with cascade impactors. *ISAM Focus Symposium*. January 25, Puerto Rico.
- Stapleton K.W., Finlay W.H., and Zuberbuhler P. (1994). An in vitro method for determining regional dosages delivered by jet nebulizers. *Journal of Aerosol Medicine*. **7**(4): 325-344.

- Sterk P.J., Plomp A., van de Vate J.F., and Quanjer P.H. (1984). Physical properties of aerosols produced by several jet and ultrasonic nebulizers. *Bulletin of European Physiopathological Respiration*. **20**: 65.
- Stuart B.O. (1973). Deposition of Inhaled Aerosols. *Archives of Internal Medicine*. **131**:60-73.
- Swift D.L., & Proctor D.F. (1977). Access of air to the respiratory tract. In: *Respiratory Defince Mechanisms*. (Eds. J.D. Brain, D.F. Proctor, & L.M. Reid) Dekker, NY. **3**: 63-94.
- Taulbee D.B. and Yu C.P. (1975). A theory of aerosol deposition in the human respiratory tract. *Journal of Applied Physiology*. **38**(1): 77-85.
- Taulbee D.B., Yu C.P., and Heyder J. (1978). Aerosol transport in the human lung from analysis of single breaths. *Journal of Applied Physiology*. **44**(5): 803-812.
- Tennekes H., and Lumley J.L. (1992). *A First Course in Turbulence*. The MIT Press, Cambridge, MA.
- Thompson D.A. (1942). *Growth and Form*. Cambridge Univ. Press, New York, NY.
- Titze I.R. (1973). The Human Vocal Cords: A Mathamatical Model. *Phonetica* **28**: 129-170.
- Titze I.R. (1974). The human vocal cords: A mathematical model. Part II. *Phonetica*. **29**: 1-21.
- Titze I.R. (1989). A four-parameter model of the glottis and vocal fold contact area. *Speech Communication*. **8**: 191-201.
- Trajan M., Logus J.W., Enns E.G., Man S.F.P. (1984) Relationship between regional ventilation and aerosol deposition in tidal breathing. *American Review of Respiratory Disease*. **130**: 64-70.
- Tsu M.E., Babb A.L., Ralph D.D., and Hlastala M.P. (1988). Dynamics of heat, water, and soluble gas exchange in the human airways: a model study. *Annals of Biomediacal Engineering*. **16**: 547-571.
- Tsuda A., Henry F.S., Otani Y., Haber S., and Butler J.P. (1996). Aerosol transport and deposition in the rhythmically expanding pulmonary acinus. *Journal of Aerosol Medicine*. **9**(3): 389-408.
- USP (United States Pharmacopeia) (1995). **23**: 1765-1766.
- Wang C.Y. (1991). Exact solutions of the steady-state Navier-Stokes equations. *Annual Reviews of Fluid Mechanics*. **23**: 159-177.
- Weibel E.R. (1963). *Morphometry of the human lung*. Academic Publishers Inc., New York.

- Wilcox D.C. (1993). *Turbulence Modeling for CFD*. DCW Industries Inc. La Cañada, CA.
- Williams M.H. (1974). Steroid and Antibiotic Aerosols. . *American Review of Respiratory Diseases*. **110**: 122-.
- Wilson D.J. (1997) Personal communication.
- Xu, G.B., and Yu, C.P. (1985). Theoretical Lung Deposition of Hygroscopic NaCl Aerosols. *Aerosol Science and Technology*. **4**:455-461.
- Yeh H-C., & Schum G.M. (1980). Models of Human Lung Airways and their Application to Inhaled Particle Deposition. *Bulletin of Mathematical Biology*. **42**:461-480.
- Yu C.P., & Diu C.K. (1982a) A comparative study of aerosol deposition in different lung models. *American Industrial Hygiene Association Journal*. **43**(1):54-65.
- Yu, C.P., and Diu, C.K. (1982b). A Probabilistic Model for Intersubject Deposition Variability of Inhaled Particles, *Aerosol Science and Technology*. **1**: 355-362.
- Yu C.P., & Cohen B.S. (1994). Tracheobronchial airway deposition of ultrafine particles. In: Inhaled Particles VII. Proceedings of an International Symposium on Inhaled Particles Organized by the British Occupational Hygiene Society. 16-22 September, 1991 (Eds. Dodgson J., & McCallum R.L.) *Annals of Occupational Hygiene*.
- Yu G., Zhand Z., and Lessmann R. (1996). Computer simulation of the flow field and particle deposition by diffusion in a 3-D human airway bifurcation. *Aerosol Science and Technology*. **25**: 338-352.
- Zainudin M.B.Z., Biddiscombe M., Tolfree S.E.J., Short M., and Spiro S.G. (1990). Comparison of bronchodilator responses and deposition patterns of salbutamol inhaled from a pressurized metered dose inhaler, as a dry powder, and as a nebulizer solution. *Thorax*. **45**: 469-473.

7. Appendix A

This appendix contains the input files for the deposition model. The contents of the main input file `data.dat` are:

```
'      Data file for RegDep program.
=====
```

This file contains the configuration information for the regdep program for Versions 4.8 and greater. Deleting any lines, or moving decimal places may cause the program to crash.

Input type

2

Nebulizer type

2

Aerosol Type

1

Aerosol Characteristics (if Input = 2 only)

4.0
1.6
0900000.0
1.0

Calculation type

1
0.005

Room information:

22.5
50.0

Solution information:

4.0
72.0
* Drugs
1
'Ventolin'

001.00
 00576.70
 1.5
 2.5
 NoDrug
 000.00
 00000.00
 0.0
 0.0
 * Suspension info
 2
 'Budesonide'
 000.50
 01.6
 1.26
 * Salts
 0
 000.00
 0
 000.00
 58.43
 2.145
 1.85

Breathing information:

0.75
 500.0
 1.0
 50.00
 00.00

Nebulizer Flow rate: (if Input = 1 only)

6.4
 4.5

Mouthpiece dimensions

4.0
 1.40
 1.0 Flag, 0=mouthpiece only, 1= lung

COPD Lung !Modification by LKY 20.6.95

0.0
 3.50

Pediatric Lung !Modification by LKY 11.08.95

0

Calculate effective diameters for alveolar?

0 !flag, 0=no, 1=yes

Lung Geometry

0.0
2.0
30.0
183.5

Key to data:

Input source

flag 1= nebulizer
2=specified aerosol

Nebulizer type

flag 1=continuous running jet nebulizer
2=vented jet nebulizer
3=ultrasonic nebulizer

Aerosol Type

flag (1 = non-hygroscopic aerosol
2 = initially solid, hygroscopic aerosol
3 = liquid hygroscopic aerosol)

Aerosol Characteristics (if Input = 2 only)

mass median diameter of aerosol
geometric standard deviation of aerosol
approximate number of particles per cc in the aerosol
bin width (min=0.1 max=9.9)

Calculation type

flag (1 = tracks single particle of each size through respiratory tract
2 = uses Lagrangian multiphase approach to solve heat and vapour

transport equations through respiratory tract)
RERR relative error in the implicit solver. For Lagrangian multiphase only

Room information:

temperature (degrees celcius)
relative humidity (%)

Solution information:

initial volume of solution in the nebulizer (ml) (if Input=1 only)
surface tension of liquid (mJ/sq. m)

* Drugs

Flag, (1=solution, 2=suspension)
Name of drug 1 (in ' ')
initial concentration of drug 1 in the solution (mg/ml)
molecular weight of drug 1
density of drug 1

```

van't hoff factor of drug 1
Name of drug 2 (in ' ')
initail concentration of drug 2 in the solution (mg/ml)
density of drug 2
van't Hoff factor of drug 2
* Suspension info
  flag, 1=suspension,2=solution
  Name of drug (in ' ')
  initial concentration of drug
  CMD of drug particles
  density of drug particles
* Salts
  flag for salt 1 (1=saline, 0=none)
  initial concentration of salt 1 (mg/ml)
  flag for salt 2 (1=saline, 11=other)
  initail concentration of salt 2 (mg/ml)
  molecular weight of salt 2
  density of salt 2
  van't Hoff factor of salt 2

Breathing information:

  tidal volume (litres)
  Inhalation flow rate (cc/s)
  Type of breathing (0=nose breathing, 1=mouth breathing)
  % of breathing cycle where patient inhales
  % of breathing cycle which is the pause between inhalation and
  exhalation

Nebulizer Flow Rate: (if Input=1 only)

  neb flow rate (l/min)
  solution temperature drop

Mouthpiece dimensions:

  length
  diameter

COPD Lung Model

  flag (0.0=use healthy lung, 1.0=COPD lung model)
  Total resistance

Pediatric Lung Model

  0=pediatric lung model not used, any other number=age (months)

Lung Geometry

  flag (0 = no scale use population averages, 1 = scale for an
  individual)
  sex (1=female, 2=male)
  age (years)
  height (cm)

```

The information on the mass lost from the nebulizers is contained in the file

NebInfo.dat:

Time Av Neb Mass Error
1st min 1.1233

Concentration at end of Nebulization period
1.33356

Mass of solids collected on filter (vented jet neb only)
0.3000

Notes:

For a continuous running jet nebulizer, the "Av Neb Mass" is the change in the nebulizer mass each minute. Measuring this each minute will result in the most accurate results from the model. In the "Concentration...." field, the concentration of the solution in the nebulizer bowl should be entered. This value should be the increase in concentration relative to the initial concentration

For a vented jet nebulizer, the mass of water collected on the filter for the entire run should be entered in the "Av Neb Mass" spot, with the number of minutes set to 1. No errors are needed. The "Mass of solids collected on filter" is the number of milligrams of salt and drug collected on the filter over the entire run. The concentration field is not used for vented jet nebulizers.

The names of the PDA files for the size measurement are contained in the file

FileNames.txt:

This file contains the names of the data files from the Dantek system. This file is for versions 4.2 and later of the code. See note at end for info on vented jet nebs

Number of Data Files

1
9

Number of classes in the data files

185

Data file for 1st minute

'neb1.ct0'
'neb1.ct1'
'neb1.ct2'
'neb1.ct3'
'neb1.ct4'
'neb1.ct5'
'neb1.ct6'
'neb1.ct7'
'neb1.ct8'
'neb1.ct9'

Data files for 2nd minute

'12.prn'
'22.prn'
'32.prn'
'42.prn'
'52.prn'
'62.prn'
'72.prn'
'82.prn'
'92.prn'

Data files for 3rd minute

'13.prn'
'23.prn'
'33.prn'
'43.prn'
'53.prn'
'63.prn'
'73.prn'
'83.prn'
'93.prn'
'103.prn'

Data files for 4th minute

'14.prn'
'24.prn'
'34.prn'
'44.prn'
'54.prn'
'64.prn'
'74.prn'
'84.prn'
'94.prn'
'104.prn'

Data files for 5th minute

'15.prn'
'25.prn'

'35.prn'
'45.prn'
'55.prn'
'65.prn'
'75.prn'
'85.prn'
'105.prn'

Data files for 6th minute

'16.prn'
'26.prn'
'36.prn'
'46.prn'
'56.prn'
'66.prn'
'76.prn'
'86.prn'
'96.prn'
'106.prn'

NOTE:

For vented jet nebulizers, the number of minutes should be set to 1. This is because the solution concentration in the particles is average over the entire run time. Multiple PDA measurements should be taken, and can be averaged here.

For suspension drugs, the number of minutes is automatically set to 1.

1. Appendix B

The main output from the deposition model is contained in the file `results.out`:

Program Output
=====

Test type: Vented jet nebulizer

Test Conditions:

Ambient Temperature: 296.1
Ambient RH: 55.0

Uncoupled particle and ambient phases

The lung is for an average person (6000cc)
at 51% TLC (3050cc)

Breathing Conditions:

Tidal Volume (cc): 750.0
Inspiration Flow Rate (cc/s): 300.0
Breathing cycle inhalation percent: 50.00
Breathing cycle holding percent: .00

Initial Solution data:

Drug type: Solution
Volume of liquid in nebulizer (ml): 2.50
Drug 1: 'Ventolin'
Initial concentration of drug 1 (mg/ml): 1.00

Salt 1: Saline
Initial Concentration of salt 1 (mg/ml): 9.00

Aerosol MMD (micrometres): 6.02
Aerosol GSD: 1.74

Regional Dosage (mg, (std dev))

'Ventolin'

ExtraTh:	.16736	(.07068)
Bronchial:	.22416	(.08851)
Alveolar:	.08467	(.02943)

Total Delivered Dose (mg): .476192

Inhaled Mass (mg): .553110

Percent drug delivered to each compartment

ExtraTh:	6.694256
Bronchial:	8.966582
Alveolar:	3.386846
Total:	19.047683

If you have drug in your solution, the dosage
delivered is DRUG only, if you do not have
drug, then the dosage is salt
Deposition probs are available in "out.out"
Particle sizes and temperature and RH in each
generation are available in "size.out"
Dosage delivered to each generation is
available in "gendose.out"
Dosage delivered to each compartment per minute
is available in "dosage.out"

Tue Dec 3 06:39:30 1996

/v/kevin/regdep/pari/2/neb1/
Code Version 5.3

The distribution of the aerosol output by the nebulizer after correction for the optical depth of the cloud is output in distribution.out

Number density of inhaled particles

NOTE: for nebulizers delivering a suspended drug, these numbers should be divided by the nebulizer run time (min).

Total Number density 852202.1

Class Breakdown

Minute number 1

Class	Number of particles (per cc)
1	138.4
2	645.7
3	1614.3
4	3090.2
5	6826.1
6	14482.4
7	26197.5
8	43262.7
9	66739.0
10	88185.9
11	91230.0
12	93351.6
13	77531.6
14	60973.7
15	47321.5
16	36805.6
17	29610.5
18	24168.1
19	21124.0
20	16327.3
21	15497.1
22	12406.9
23	11715.1
24	9501.2
25	7794.7
26	6780.0
27	5488.6
28	4796.7
29	3828.2
30	3643.7
31	2767.3
32	2490.6
33	2260.0

34	1937.1
35	1568.2
36	1568.2
37	1291.4
38	1199.2
39	1106.9
40	876.3
41	691.8
42	553.5
43	507.3
44	461.2
45	276.7
46	322.9
47	276.7
48	230.6
49	138.4
50	92.2
51	138.4
52	138.4
53	46.1
54	46.1
55	.0
56	46.1
57	46.1
58	46.1

Tue Dec 3 06:39:30 1996

/v/kevin/regdep/pari/2/neb1/
Code Version 5.3

The deposition model also outputs the size of each droplet class at the end of each generation of the Weibel lung along with the temperature and relative humidity of the air. Additionally, the dosage delivered by each particle size class to each individual generation is available. These files are not included here for space considerations